

HUMBOLDT-UNIVERSITÄT ZU BERLIN
MATHEMATISCH-NATURWISSENSCHAFTLICHE FAKULTÄT I
INSTITUT FÜR PHYSIK

On the semiclassical structure of QCD
— A lattice study at finite temperature —

DIPLOMARBEIT

eingereicht von

DIRK PESCHKA

geboren am 21. November 1977 in Zossen

Aufgabensteller: Prof. Dr. M. Müller-Preußker
Zweitgutachter: Prof. Dr. U. Wolff
Abgabedatum: 30. August 2004

Contents

1	Introduction	2
2	Quantum mechanics and the semiclassical approximation	5
2.1	The path-integral in quantum mechanics	5
2.2	Semiclassical approach to quantum mechanics	8
2.3	Kink solutions and fluctuations	10
2.4	Kink-gas approximation	13
2.5	Numerical results for the double-well	14
2.6	Lessons for QCD	20
3	Classical $SU(3)$ gauge fields	21
3.1	Classical $SU(3)$ gauge theory	21
3.2	Calorons in $SU(2)$	24
3.3	Calorons in $SU(3)$	27
3.4	Instanton model	29
4	QCD on the lattice	33
4.1	Functional integral for lattice QCD	33
4.2	QCD at finite temperature	34
4.3	Improved actions	37
4.4	Cooling methods	38
4.5	Detecting classical fields on the lattice	39
5	Classical solutions on the lattice - examples	42
5.1	Systematics of the investigation	42
5.2	Constructed calorons with $ Q = 1$	45
5.3	Cooled calorons with $ Q = 1$	53
5.4	Cooled calorons with $ Q = 2$	61
5.5	Caloron-anticaloron superposition with $Q = 0$	67
5.6	Fitting an analytical expression	70
5.7	Summary	73
6	Classical solutions on the lattice - statistical properties	74
6.1	Problems finding calorons in $SU(3)$	74
6.2	Moduli space of lattice calorons	77
6.3	Dependence on the aspect ratio N_t/N_s	82
6.4	Dependence on the volume N_s^3	84

6.5	Non-caloron configurations from cooling	85
6.6	Summary	86
7	Summary and Outlook	87
7.1	Summary	87
7.2	Conclusions	88
7.3	Outlook	88
A	Projection to $SU(N)$	89
A.1	General remarks	89
A.2	Projection to $SU(2)$	91
A.3	Iterative projection to $SU(N)$	91
B	Testing the Dirac operator	92
	Acknowledgements	93

Abstract

In this numerical study the semiclassical structure of finite temperature $SU(3)$ Yang-Mills theory is examined. The classical solutions with non-trivial holonomy, found in the year 1998 by Kraan-van Baal and Lee-Lu, are of particular interest. The classical gauge fields to be analysed are obtained from a Monte-Carlo ensemble by the 'cooling' method. The actual appearance of these solutions is determined by the holonomy and the aspect ratio of the lattice. Despite the finiteness of the lattice, the analytical behaviour for these solutions is confirmed, for single configurations and for whole ensembles.

From these findings we conclude that the instanton model at finite temperature, where Harrington-Shepard calorons are the building blocks of the semiclassical approximation, has to be reconsidered. Within our approach we find signals to identify background fields of KvBLL caloron type in the quantised lattice Yang-Mills theory near the deconfined phase transition. A new self-consistent semiclassical model would have to take into account the fact that these new caloron fields couple to the Polyakov loop, being the order parameter of the phase transition.

Zusammenfassung

Diese Arbeit beschäftigt sich mit der semiklassischen Struktur der $SU(3)$ Gittereichtheorie bei endlicher Temperatur. Von besonderem Interesse sind die klassischen Lösungen der Feldgleichungen mit nichttrivialer asymptotischer Holonomie. Instantonmodelle bei endlicher Temperatur gingen bisher von Lösungen mit trivialem Polyakov-Loop in der räumlichen Asymptotik aus. Die hier untersuchten Lösungen werden auf dem Gitter aus einem Monte-Carlo Ensemble in der Confinement-Phase durch die "cooling" Methode gewonnen. Wir finden bei diesen Feldern im allgemeinen eine nichttriviale Holonomie und die Signaturen, welche die von Kraan-van Baal und Lee-Lu im Jahr 1998 beschriebenen Lösungen im $S^1 \times \mathbb{R}^3$ besitzen.

In diesem Licht ist die bisherige Auswahl von klassischen Lösungen, wie sie in ein Instantonmodell bei endlicher Temperatur einfließen, zu überdenken. Bei endlicher Temperatur sollte eine semiklassische Approximation nahe dem Phasenübergang auf allgemeineren KvBLL Caloronen beruhen, um die Kopplung an den Polyakov-Loop konsistent zu beschreiben.

Chapter 1

Introduction

Today quantum field theory is the appropriate formalism to explain features of elementary particles and their interactions. It is known to produce excellent results in the case of perturbative quantum electrodynamics. It is widely believed that the so-called quantum chromodynamics (QCD) is the theory that describes strong nuclear forces. QCD is obtained from a local gauge principle based on the gauge group $SU(3)_{\text{color}}$. The strong interaction between fundamental quark flavours is mediated by the exchange of coloured gluons, the vector bosons of the corresponding Yang-Mills theory. The Lagrangian density of QCD in Euclidean space is [1–3]

$$\mathcal{L}(A_\mu, \psi, \bar{\psi}) = -\frac{1}{4} \sum F_{\mu\nu}^a F_{\mu\nu}^a + \sum \bar{\psi}_f (\not{D} + m_f) \psi_f,$$

where the sums run over colour, spinor and flavour indices. Due to the non-commutativity of the gauge group the gluons can self-interact.

Baryons and mesons, which are found in experiments, are described as bound states of three quarks or a quark and an anti-quark. Within the so-called quark model these bound states are qualitatively classified as multiplets of the flavour group [4] (Nobel price 1969). The quark model has been kinematically very successful in the description of the observed meson and baryon states and their quantum numbers. On the other hand, no free quarks have ever been observed.

QCD can be studied perturbatively in deep inelastic electron-proton scattering experiments [5]. However, the explanation of bound states of quarks lies within the non-perturbative regime of QCD, where no reasonable results can be obtained from perturbative expansions in the strong coupling constant α_s . The lattice formulation provides a convenient framework to study the non-perturbative regime of QCD. Fundamental properties like confinement, which explains why quarks are only found as colour-singlet bound states, are reproduced within the lattice approach. Nevertheless, quantitative lattice calculations should be accompanied by a qualitative understanding of the phenomenology of QCD and its vacuum structure.

One can imagine that the QCD vacuum consists of non-perturbative fluctuations of the gluon fields. The model where these background fields are characterised by superpositions of instanton and anti-instanton fields is the so-called instanton liquid model [6–10].

An instanton is a topologically non-trivial solution of the $SU(3)$ Yang-Mills equation of motion [11]. A prominent feature of the QCD vacuum is the axial $U(1)$

anomaly. The conservation of the axial quark current, which holds for the classical theory, is not found in the quantum theory. In fact, the divergence of the expectation value of the axial current does not vanish in the quantum theory, but is proportional to the topological charge density. The topological charge density related to the instanton field can give a qualitative explanation for the relatively large mass of the η' [12]. Another effect explained with the help of instantons is the spontaneous breaking of chiral symmetry. The chiral condensate $\langle \bar{\psi}\psi \rangle$, which is the order parameter of this symmetry, is connected with the spectral density $\rho(\lambda)$ of the Dirac operator by the Banks-Casher relation [13]

$$\langle \bar{\psi}\psi \rangle = - \lim_{m \rightarrow 0} \lim_{V \rightarrow \infty} V^{-1} \frac{\partial}{\partial m} \ln \mathcal{Z} = - \lim_{\lambda \rightarrow 0} \lim_{m \rightarrow 0} \lim_{V \rightarrow \infty} \frac{\pi}{V} \langle \rho(\lambda) \rangle.$$

For a vacuum filled with instantons and anti-instantons a finite density of eigenvalues near zero is generated by overlapping instantons. The eigenvalue $\lambda = 0$ of the Dirac operator for a single (anti) instanton is lifted to $\lambda = \pm |\psi_I \not{D} \psi_A|$ if a superposition of an instanton zero-mode ψ_I and an anti-instanton zero-mode ψ_A is considered as the proper vacuum background.

What is still missing from the point of view of the instanton liquid model is a working mechanism of confinement. Today's most accepted scenario for confinement is based on the dual super-conductor picture [14]. Attempts to describe confinement within the random instanton approach were not able to get a confining string tension of the right magnitude or to get confinement at all [15]. It seems that additional degrees of freedom are needed [16] in order to describe this key property. Only very recently Negele [17] proposed a confinement mechanism based on a strongly correlated instanton or meron ensemble in the regular gauge.

At finite temperature the Yang-Mills theory has a similar vacuum structure, built from periodic instantons or so-called calorons [18]. These fields are characterised by their Polyakov loop at spatial infinity, which is called the asymptotic holonomy. It was pointed out that a non-trivial asymptotic holonomy (not in the centre of the gauge group) is suppressed [19]. Hence, classical fields with a non-trivial asymptotic Polyakov loop were neglected in the vacuum and a corresponding caloron solution with non-trivial holonomy remained unknown. In the last years new caloron solutions with non-trivial holonomy were found and studied by Kraan-van Baal [20] and Lee-Lu [21], hence we call this solution KvBLL caloron. The mechanism of coupling these fields to the Polyakov loop, the order parameter of the deconfinement phase transition, is of particular interest. In certain limits the KvBLL caloron reproduces the BPST instanton solution [11] or the caloron with trivial asymptotic Polyakov loop [18] but it has some additional interesting features. Recent work [22, 23] also deals with the semiclassical quantisation of calorons with non-trivial holonomy and with the extension of the parameter space to other topological sectors [24]. All these works point out that a non-trivial asymptotic Polyakov loop cannot be neglected. Such analytical progress of semiclassical methods is supplemented by investigations of lattice fields [25, 26], where the topological content of Monte-Carlo ensembles is examined.

The subject of this work is to systematically study whether classical solutions, which are numerically obtained on a finite and asymmetric lattice, can be described within the parameter space, the so-called moduli space, of KvBLL calorons. These fields serve as a starting point for the semiclassical approximation. In order to obtain classical solutions of the $SU(3)$ lattice gauge theory, Monte-Carlo fields are 'cooled' [27, 28] until the equations of motion are sufficiently fulfilled. To extend the previous work from $SU(2)$ [29, 30] to the more challenging case of $SU(3)$ many tools for the investigation have been improved. The main problem, which was formulated for this work, is the following.

Can we find evidence that classical $SU(3)$ gauge fields on asymmetric lattices are described in terms of KvBLL calorons?

This study tries to answer the question and to motivate the semiclassical calculations. It is organised as follows. In Chapter 2 the semiclassical approach is briefly explained using a quantum mechanical toy model. Some numerical methods which are important for QCD will be introduced and motivated. In particular, the numerical approach in terms of the Feynman path-integral and the operator formalism are compared for this toy model and the role of the vacuum is addressed. The cooling technique is proposed to obtain classical solutions and to test the viability of the semiclassical approach. In Chapter 3 the $SU(3)$ Yang-Mills theory is introduced on a classical level and the classical solutions of the equation of motion will be specified and described. The chapter is closed by a brief review of the current status of the semiclassical quantisation for finite temperature field theory. In Chapter 4 the lattice formulation of the theory and the definitions of observables, which are essential to identify KvBLL calorons and investigate their properties, are introduced. The results of the numerical work are split up to show and discuss examples of calorons within Chapter 5 and to show and discuss the statistical analysis for an ensemble of calorons from different topological sectors in Chapter 6. The conclusions from the numerical work and the summary are made in Chapter 7. Finally an outlook for future work is given.

Chapter 2

Quantum mechanics and the semiclassical approximation

In this chapter the path integral approach to quantum mechanics will be briefly introduced. Within this formalism the semiclassical approach, also known as saddle point method, is formulated. Analytical calculations and numerical results are presented for a the double-well oscillator to illustrate the language and techniques, that are also used in case of the semiclassical approach to QCD. The quantum mechanical vacuum will be described as a gas of non-interacting pseudo-particles (kink gas). The own numerical work was guided by the publications of Creutz, Freedman [31] and Huang [32].

2.1 The path-integral in quantum mechanics

In quantum mechanics physical quantities like momentum p and location x are usually replaced by Hermitian operators \hat{p} and \hat{x} , which fulfil the commutator relations $[\hat{q}, \hat{p}] = i\hbar$, $[\hat{q}, \hat{q}] = [\hat{p}, \hat{p}] = 0$. This is the canonical approach. These operators act on a Hilbert space of physical states $|\psi\rangle$. Within some arbitrary representation, e.g. position space, such states are complex functions with the scalar product $\langle\psi|\phi\rangle = \int dx \bar{\psi}(x)\phi(x)$. A measurement of a quantity \hat{O} in a state $|\psi\rangle$ is defined

$$\langle\psi|\hat{O}|\psi\rangle := \int dx \bar{\psi}(x)\hat{O}\psi(x).$$

In the Schrödinger picture the time dependence of states in a system with a Hamilton operator $\mathcal{H}(\hat{p}, \hat{q})$ is governed by the time dependent Schrödinger equation

$$i\hbar\frac{\partial}{\partial t}|\psi(t)\rangle = \mathcal{H}(\hat{p}, \hat{q})|\psi(t)\rangle$$

The time evolution of a state in Eq. 2.1 can formally be written using the time evolution operator $U(t) := \exp[-i\mathcal{H}t/\hbar]$

$$|\psi(t)\rangle = U(t)|\psi(t=0)\rangle$$

The path integral approach to quantum mechanics is an alternative method to formulate quantum mechanics and to circumvent the non-commuting operators. For

this purpose one calculates the matrix element W of $U(t)$ between location eigenstates. One will see that this approach provides a different starting point for doing the same quantum mechanical calculations. The matrix element in question is

$$W(x, t; y, 0) := \langle x | U(t) | y \rangle. \quad (2.1)$$

The matrix element W , also known as Feynman kernel, solves the time dependent Schrödinger equation with an initial condition

$$\psi(x, t) = \int dy W(x, t; y, 0) \psi(y, t = 0).$$

Since the time evolution operator has the property $U(t)U(t') = U(t + t')$ an expression for W can be obtained iteratively in the limit of an infinite number $N \rightarrow \infty$ of infinitesimal small time translations $\epsilon = t/N \rightarrow 0$. The so-called transfer matrix $\langle x | T(\epsilon) | y \rangle = W(x, \epsilon, y, 0)$, which enters the construction through the limit $U(t) = \lim_{N \rightarrow \infty} T(t/N)^N$, is explicitly known up to corrections of order $\mathcal{O}(\epsilon^3)$.

$$\langle x | T(\epsilon) | y \rangle = \left(\frac{m}{2\pi\hbar i\epsilon} \right)^{1/2} \exp \left[\frac{im}{2\hbar\epsilon} (x - y)^2 - \frac{i\epsilon}{2\hbar} (V(x) + V(y)) \right] + \mathcal{O}(\epsilon^3).$$

To take this limit the time axis $[0, t]$ is cut in N equal subintervals of length $\epsilon = t/N$ and a unity operator $\int dx | x \rangle \langle x | = \mathbb{1}$ is inserted to obtain W .

$$W(x, t; y, 0) = \lim_{N \rightarrow \infty} \int dx_1 \dots dx_{N-1} \langle x | T | x_1 \rangle \langle x_1 | \dots \langle x_{N-1} | T | y \rangle$$

With the abbreviations

$$\mathcal{D}x := \left(\frac{m}{2\pi\hbar i\epsilon} \right)^{N/2} dx_1 \dots dx_{N-1} \quad (2.2)$$

$$S[x] := \sum_{n=0}^{N-1} \epsilon \left[\frac{m}{2} \left(\frac{x_{n+1} - x_n}{\epsilon} \right)^2 - \frac{V(x_{n+1}) + V(x_n)}{2} \right] \quad (2.3)$$

where the first is the measure and the latter is an approximation of the continuum action for not necessarily classical paths, one arrives at the well known Feynman form of path integral for a non-relativistic quantum-mechanical system

$$W(x, t; y, 0) = \lim_{N \rightarrow \infty} \int \mathcal{D}x \exp \left[\frac{i}{\hbar} S[x] \right]. \quad (2.4)$$

The states x (final) and y (initial) enter the expression by $x_0 := y$ and $x_N := x$. Besides the Schrödinger equation and the matrix approach the path-integral is another fundamental approach to quantum mechanics. The idea for this new formulation came from Dirac but it was Feynman [33] who further established it. One can imagine the path integral being a sum of paths with an oscillating, complex-valued weight.

A heuristic argument for convergence is that the strongly oscillating contributions cancel out and one is left with small fluctuations around a stationary path. The transition to Euclidean time $-it/\hbar \rightarrow \beta$ and $\Delta\tau = \beta/N$, also known as Wick rotation, makes the numerical computation by importance sampling possible and yields an analogy to statistical mechanics. In the limit $\beta \rightarrow \infty$ the Feynman kernel is dominated by the vacuum state because $\exp[-\beta\mathcal{H}]$ is dominated by its smallest eigenvalue. In the Euclidean language the Feynman kernel reads

$$W_E(x, \beta; y, 0) = \langle x | \exp[-\beta\mathcal{H}] | y \rangle = \int \mathcal{D}_E x \exp[-S_E[x]].$$

The action S_E differs from S by the positive sign of the potential $V(x)$ in the Lagrangian function. The weight factor e^{-S_E} is now positive and real. If the potential is bounded from below there exists a path with maximal weight. Where the main contribution to the sum of path comes from is determined by the competition of action versus the measure of paths¹. In fact, the measure $\mathcal{D}x$ is flat in case of quantum mechanics and this competition looks trivial. Having performed the Wick rotation, the Feynman kernel in Euclidean space is given by (from here \hbar is set to unity)

$$\begin{aligned} W_E(x, \beta; y, 0) &= \lim_{N \rightarrow \infty} \int \mathcal{D}_E x \exp[-S_E] & (2.5) \\ \mathcal{D}_E x &:= \left(\frac{m}{2\pi \Delta\tau}\right)^{N/2} dx_1 \dots dx_{N-1} \\ S_E[x_n] &:= \sum_{n=0}^{N-1} \Delta\tau \left[\frac{m}{2} \left(\frac{x_{n+1} - x_n}{\Delta\tau}\right)^2 + \frac{V(x_{n+1}) + V(x_n)}{2} \right]. \end{aligned}$$

However, one is interested in properties of the original system. With the exception of the real-time evolution, almost all those properties can be conveniently studied in the path integral language. To extrapolate back to the original problem it is best to study the behaviour of the partition sum $\mathcal{Z}_{qm} = \text{tr}(\exp[-\beta\mathcal{H}])$ of the quantum mechanical model². By just looking at the propagator W_E one might lose some information, e.g. energy levels of some parity.

Being aware of that danger one also studies the lowest energy levels by investigating the asymptotic behaviour of W_E for large Euclidean times $\beta \rightarrow \infty$. One could also study the two-point correlator $\langle x(\tau)x(\tau') \rangle$ to obtain the energy gap from its exponential suppression for large Euclidean times $|\tau - \tau'|$ and $\beta \rightarrow \infty$. From now on everything will be calculated in Euclidean space and the index ' E ' is suppressed.

¹**Note:** "finite action is of zero measure" [34]

²**Note:** The Feynman kernel has the representation $W_E(x, \beta; x, 0) = \sum_{\text{spec}(\mathcal{H})} e^{-\beta E_n} |\psi_n(x)|^2$.

2.2 Semiclassical approach to quantum mechanics

The method and concept of the semiclassical approximation is explained for an example from quantum mechanics. The standard calculation is expanded by non-standard numerical investigations. There is some set of quantum mechanical models one could favour here [31, 35]. However, the double-well potential, in Euclidean space one should better call it the 'double-hill' potential, is chosen

$$V(x) = \frac{m\omega^2}{8\eta^2} (x^2 - \eta^2)^2.$$

In this case a perturbation expansion around a minimum of $V(x)$ would not give right results for small couplings $g^2 \propto \eta^{-2}$ because [36]

1. the perturbation series can be shown to be Borel non-summable in g ,
2. the parity transformation leaves the potential invariant, such that the eigenfunctions are classified according to a principal quantum number and the parity eigenvalues,
3. the energy splitting between states of opposite parity is described by non-analytic factors of the form $\exp[-1/6g]$.

In the limit $\eta \rightarrow \infty$ the problem decouples to a system of two harmonic oscillators with $E = \hbar\omega/2$. One can qualitatively understand this feature with the LCAO-ansatz, where one makes the assumption that the wave function is just a symmetric/antisymmetric linear combination of oscillator wave functions ψ_0 centred at $\pm\eta$

$$\psi_{s/a}(x) = \frac{1}{N_{s/a}} (\psi_0(x + \eta) \pm \psi_0(x - \eta)) \quad \psi_0(x) = \frac{2\pi}{\lambda} \exp[-\lambda/2x^2]$$

with $\lambda = m\omega/\hbar$ and the normalisation factor $N_{s/a}$ for the symmetric and antisymmetric wave function respectively. The corresponding energies³ of the Hamiltonian $\mathcal{H} = \hat{p}^2/2m + V(x)$ are

$$E_{\pm}^{\text{LCAO}} := \langle \psi_{s/a} | \mathcal{H} | \psi_{s/a} \rangle = \frac{\hbar\omega}{2} + \frac{3}{32} \frac{\hbar^2}{m\eta^2} \pm \frac{3}{8} \frac{(\hbar\omega + m\omega^2\eta^2)}{\exp\left[\frac{m\omega}{\hbar}\eta^2\right] \mp 1}$$

This solution respects parity but has the wrong asymptotical behaviour. At least it already has an exponential behaviour for small couplings. The comparison with the exact solution in Fig. 2.3 shows that the exponential small gap has the wrong slope. In Fig. 2.1 one can see the energy levels $E_n(\eta)$ for the exact solution together with this ansatz for a fixed ω .

³This can be compared with the perturbative expansion in [37].

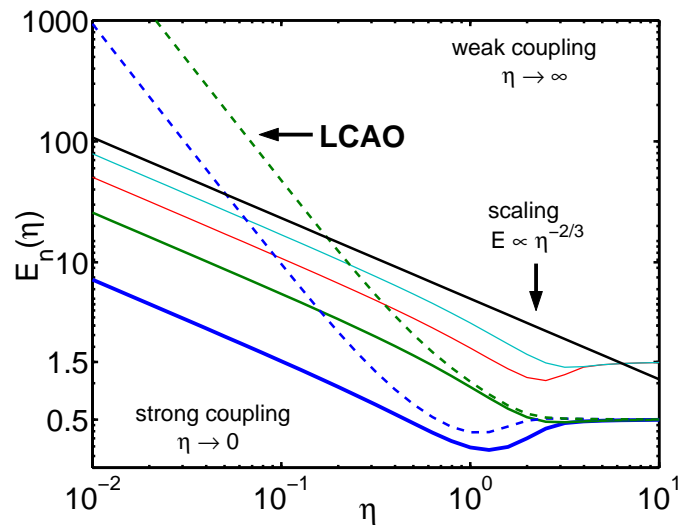


Figure 2.1: comparison of LCAO with exact result

In particular one is interested in a weak coupling approximation, that correctly describes the exponential behaviour of the mass gap. This is provided by the semiclassical approach and the kink-gas approximation.

The idea of a semiclassical approximation is to substitute the action $S[x]$ by a series of fluctuations δx around a path $x_{cl}(\tau)$, being a solution of the classical equation of motion. Compared to any path $x(t) = x_{cl}(\tau) + \delta x(\tau)$ its contribution to the Euclidean path integral should be the biggest. However, a single path is of zero measure in the sum of path. The hope is that by further integrating over quadratic fluctuations around this path one will have isolated the relevant degrees and freedom and one gets meaningful results for the calculation. Whether this hope is satisfied will become clear later. From $x(\tau) = x_{cl}(\tau) + \delta x(\tau)$ ($\delta x(0) = \delta x(\beta) = 0$) one gets a functional expansion in $S[x_{cl} + \delta x]$.

$$\begin{aligned}
 S[x_{cl} + \delta x] &= S[x_{cl}] + \int_0^\beta d\tau \left(-\frac{d^2 x_{cl}}{d\tau^2} + V'(x_{cl}) \right) \delta x(\tau) \\
 &+ \frac{1}{2} \int_0^\beta \int_0^\beta d\tau d\tau' \frac{\delta^2 S}{\delta x(\tau) \delta x(\tau')} \Big|_{x_{cl}} \delta x(\tau) \delta x(\tau') + \mathcal{O}(\delta x^3) \quad (2.6)
 \end{aligned}$$

The first integral will vanish, because x_{cl} solves the classical equation of motion. Note the sign of the potential in the equation of motions. The second part, which will be denoted by S_{fl} , describes the action of quadratic fluctuations around this classical path. The series, taken up to the 2nd order (1-loop), replaces the expression for the action S in the path integral and one ends up with a series in δx which is called the saddle-point approximation. The shift of x in the path integral is exact and the approximation enters by cutting off higher orders of δx^n . Inserting this into Eq. 2.5 gives the Euclidean Feynman kernel in the 1-loop (semiclassical) approximation

$$W(x, \beta; y, 0) = \exp[-S_{cl}] \int \mathcal{D}\delta x(\tau) \exp[-S_{fl}[\delta x]] =: e^{-S_{cl}} \mathcal{F}(\beta). \quad (2.7)$$

The integral over the quadratic fluctuations $\mathcal{F}(\beta)$ in Eq. 2.7 can be written in terms a Gaussian integral of a local operator⁴ $\delta^2 S/\delta x \delta y = \mathcal{M}(x, y)$, which is called the *Hessian of S_E* . In the case of Euclidean quantum mechanics one has

$$\mathcal{F}(\beta) = \int \mathcal{D}\delta x \exp \left[\int d\tau \frac{1}{2} \delta x \mathcal{M} \delta x \right] \quad \text{with} \quad \mathcal{M} = -\frac{d^2}{d\tau^2} + m^{-1} V''(x_{cl}). \quad (2.8)$$

Gaussian integrals in N dimensions are explicitly solvable and lead to a determinant of a $N \times N$ matrix. It is interesting to study the Feynman kernel $W_E(x, \beta, y, 0)$ with x and y located at the minima of the potential $x = \pm\eta$ and $y = \eta$. Therefore the analytic solutions of Euclidean equations of motion connecting these points are of particular interest.

2.3 Kink solutions and fluctuations

The solutions of the Euclidean equation of motion $m \ddot{x}_{cl}(\tau) = V'(x_{cl})$ are the building blocks of the semiclassical approximation. By Euclidean energy conservation one easily obtains the classical solution for the double-well potential. Using the fixed location parameter $x_{cl}(\tau_0) = 0$ the classical solution is

$$x_{cl}(\tau) = \pm\eta \tanh \left[(\tau - \tau_0) \frac{\omega}{2} \right]. \quad (2.9)$$

The two functions, one with $x_{cl}(-\infty) = -\eta$ and the other with η , are called *kink* and *anti-kink solution*. There are also classical solutions “falling from the tip of the mountain”, but they have no finite action and thus they do not contribute. There is no correspondence to a kink solution with $E = 0$ in the original theory because there simply does not exist a classical path connecting both minima. But there is the correspondence between a tunneling process in the Minkowskian quantum mechanics and the kink pseudo-particle solution in the Euclidean formulation of the path-integral. The classical action of the kink solution is calculated

$$S_{cl} = \int_{-\infty}^{+\infty} d\tau \left(\frac{m}{2} \dot{x}_{cl}^2 + V(x_{cl}) \right) = m \int_{-\eta}^{+\eta} dy \frac{\omega}{2\eta} (\eta^2 - y^2) = \frac{2}{3} \eta^2 \omega m.$$

The kink is a localised pseudo-particle since the action density $s(\tau) = \frac{m}{2} \dot{x}^2 + V(x)$ is localised at the kink position τ_0 (see Fig. 2.2 rhs).

⁴**Note:** Since this operator is symmetric the eigenvalues are real and eigenfunctions are orthogonal. The form of an operator \mathcal{M} acting on δx is obtained after a partial integration.

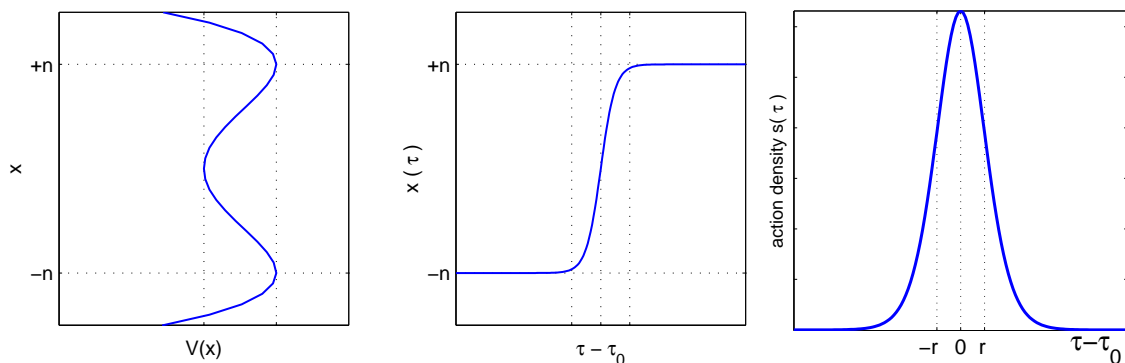


Figure 2.2: (left) double-well potential (middle) kink solution and (right) localised action density of a kink solution

In Fig. 2.2 the double-well potential and the kink-solution are illustrated. The duration time (radius) of the kink is $r = 2\omega^{-1}$ (dashed lines). It is visible, that $x(\tau)$ is located at $\pm\eta$ for $|\tau - \tau_0| \gg r$ up to (exponential) small corrections. For completeness and later use one should note that there also exist so called *multi-kink solutions*, which are superpositions of kinks and anti-kinks. They can be considered approximate solutions to the Euclidean equation of motions as long as their centres τ_i are well separated $|\tau_i - \tau_j| > r$. Such solutions can be created by a product ansatz,

$$x_{cl}^n(\tau) = \eta \prod_{i=1}^n \tanh \left[(\tau - \tau_i) \frac{\omega}{2} \right] \quad \text{where} \quad \tau_1 < \tau_2 \dots < \tau_n.$$

The action of such a solution is $S_{cl}^n \approx n S_{cl}$. The numerical investigation will also make use of paths, which are 'almost' solution of the equation of motion. These solutions $x(\tau)$ are called *streamlines*.

On the classical level (0-loop) the solutions of the equation of motion themselves are the basic ingredients of a semiclassical approximation. The quantum effects are then introduced by calculating the path integral over quadratic fluctuations (1-loop). Using the Hessian \mathcal{M} corresponding to the quantum mechanical action one can rewrite Eq. 2.8 for a finite N using the definitions of Eq. 2.5

$$\mathcal{F}_N(\beta) = \left(\frac{m}{2\pi \Delta\tau} \right)^{1/2} \left[\det (\Delta\tau^2 \mathcal{M}_\Delta)_{N-1} \right]^{-1/2} \quad (2.10)$$

where, at least for well behaved cases, the single divergent contribution from the determinant and the prefactor ($\propto 1/\sqrt{\Delta\tau}$) should give a finite result for $\lim_{N \rightarrow \infty} \mathcal{F}_N$. Of course that happens at least in the cases where the semiclassical approach is known to be exact (free particle and harmonic oscillator). The Hessian \mathcal{M}_Δ is the discretised version of \mathcal{M} Eq. 2.8

$$\mathcal{M}_\Delta = \frac{1}{\Delta\tau^2} \begin{pmatrix} -2 + W_1 & 1 & \dots & 0 & 0 \\ 1 & -2 + W_2 & \dots & 0 & 0 \\ \vdots & & \ddots & & \vdots \\ 0 & 0 & \dots & -2 + W_{N-2} & 1 \\ 0 & 0 & \dots & 1 & -2 + W_{N-1} \end{pmatrix}$$

with $W_n = \Delta\tau^2 m^{-1} V''(n\Delta\tau)$. In case of an (anti)kink the Hessian operator \mathcal{M} has the explicit form

$$\mathcal{M}(\tau, \tau') = \left[-\frac{d^2}{d\tau^2} + \omega^2 \left(1 - \frac{3}{2} \frac{1}{\cosh^2(\omega(\tau - \tau_0)/2)} \right) \right] \delta(\tau - \tau'). \quad (2.11)$$

One should observe that \mathcal{M} explicitly acts on fields and not on the $\delta(\tau - \tau')$ distribution after partial integration of the operator kernel Eq. 2.8. The spectrum corresponds to the eigenvalue problem of the one-dimensional Schrödinger equation in a Pöschl-Teller potential $V(x) = \cosh^{-2}(x)$. A detailed discussion of this potential can be found in the book of 'Landau and Lifshitz III, Introduction to quantum mechanics'. This system has two bound states (discrete spectrum) $\lambda_0 = 0$ and $\lambda_1 = 3/4\omega^2$ and a continuous spectrum for $\lambda \geq \omega^2$. The eigenfunction corresponding to λ_0 , usually referred as *zero-mode*, is

$$x_0(\tau) = \sqrt{\frac{3\omega}{8}} \cosh^{-2}(\omega(\tau - \tau_0)/2).$$

Note that the zero-mode is proportional to the derivative of $x_{cl}(\tau)$ with respect to τ_0 . If one is interested in studying streamlines, one needs to know the Hessian matrix for arbitrary paths $x(\tau)$ in the double-well potential which are not necessary solutions of the classical equation of motion. This operator is

$$\mathcal{M}(\tau, \tau') = \left[-\frac{d^2}{d\tau^2} - \frac{\omega^2}{2} \left(1 - 3 \frac{x_{E,cl}(\tau)^2}{\eta^2} \right) \right] \delta(\tau - \tau'). \quad (2.12)$$

For the further analysis the eigenvalues of \mathcal{M} and some of the eigenvectors corresponding to the lowest eigenvalues will be used for the purpose of interpretation. For the numerical analysis to be given later the general expression for the Hessian Eq. 2.12 is of importance.

The overall result for the calculation of the 1-loop Feynman kernel, after having introduced a finite Hessian matrix, is

$$W(x, \beta; y, 0) = \lim_{N \rightarrow \infty} \exp[-S_{cl}] \mathcal{F}_N(\beta).$$

Usually the Feynman kernel is then calculated by normalising the determinant relative to the harmonic oscillator W_ω with the Hessian $\mathcal{M}_\omega = -d^2/d\tau^2 + \omega^2$

$$W(x, \beta; y, 0) = W_\omega(x, \beta, y, 0) \left[\frac{\det \mathcal{M}}{\det \mathcal{M}_\omega} \right]_{x_{cl}}^{-1/2} \exp[-S_{cl}]. \quad (2.13)$$

The analytical calculation of the ratio of determinants for the double-well potential can be found in [37] or in a modern fashion in [38]. The main difficulty in the computation of the ratio of determinants is that the spectrum of \mathcal{M} contains an zero mode $x_0(\tau)$ while \mathcal{M}_ω has none. This is due to the τ_0 -translational invariance of the kink solution. In QCD one will also encounter zero-modes, which come from symmetries of the classical solution. Due to this invariance, the associated fluctuations are not

Gaussian but can be calculated exactly by using the method of collective coordinates [39, 40], where one replaces the integral over fluctuations associated with the exact value of the integral and leaves the zero-eigenvalue out. The determinant without the lowest eigenvalue is denoted by $\det' [\mathcal{M}]$.

$$\left[\frac{\det \mathcal{M}}{\det \mathcal{M}_\omega} \right]_{x_{cl}}^{-1/2} \xrightarrow{\text{collective coordinates}} \sqrt{\frac{S_{cl}}{2\pi}} \omega \int d\tau_0 \underbrace{\left[\frac{\det' [\mathcal{M}]}{\det' [\mathcal{M}_\omega]} \right]^{-1/2}}_{\sqrt{12}}$$

Putting all steps together one arrives at an expression for the Feynman kernel of the double-well potential in the 1-loop approximation with a single kink

$$W_E(\eta, \beta, -\eta, 0) = \sqrt{\frac{m\omega}{\pi}} \exp \left[-\frac{\omega\beta}{2} \right] \exp [-S_{cl}] \sqrt{\frac{6S_{cl}}{\pi}} \omega \beta \quad (2.14)$$

In the end one question arises. Is the result based on the relevant degrees of freedom? To extend this model usually a superposition of I kinks and A anti-kinks, where the number $I - A$ is fixed due to the boundary condition by $\int_0^\beta d\tau \dot{x}_{cl}(\tau) = x(\beta) - x(0)$, is considered. For $\beta \rightarrow \infty$ this is no serious restriction, although a superposition of kinks and anti-kinks is no strict solution of the equation of motion.

2.4 Kink-gas approximation

The kink gas can be understood as a superposition of single kink-amplitudes. The different centre positions $\{\tau_i\}$ are the position of pseudo-particles in the kink-gas. Formally one writes

$$W_E(\pm\eta, \beta; \eta, 0) = \sum_{\substack{\text{only even} \\ \text{or odd } n}} \int \left[\prod_{i=1}^n d\tau_i \right] W_E(\eta_{i+1}, \tau_{i+1}; \eta_i, \tau_i) \quad \eta_i = (-\eta)^i. \quad (2.15)$$

This expression describes the more realistic situation of *kink-gas*. The gas describes the situation of non-interacting localised pseudo-particles in a volume β with $\kappa = \omega\sqrt{6S_{cl}/\pi}$.

$$\begin{aligned} \langle \pm\eta | \exp [-\beta\mathcal{H}] | \eta \rangle &= \sqrt{\frac{m\omega}{\pi}} e^{-\frac{\omega\beta}{2}} \sum_{\text{even or odd}} \frac{1}{n!} (\kappa \exp [-S_{cl}])^n \\ &= \sqrt{\frac{m\omega}{4\pi}} e^{-\frac{\omega\beta}{2}} \left[\exp [\kappa e^{-S_{cl}}] \pm \exp [-\kappa e^{-S_{cl}}] \right] \end{aligned}$$

This expression seems to be complete in a sense, that the relevant degrees of freedom were considered. From the transition amplitude one can read off the energy splitting due to tunnelling⁵

$$E_{\pm} = \hbar\omega \left(\frac{1}{2} \pm 2\eta \sqrt{\frac{\omega m}{\pi \hbar}} \exp \left[-\frac{2\eta^2 \omega m}{3\hbar} \right] \right) \quad (2.16)$$

⁵here we will insert the \hbar factors

It becomes clear that the expression for the energy gap $\Delta = E_+ - E_-$, whose calculation was the purpose of this chapter, in the kink gas approximation fits very well to the exact results. The exponential small energy gap is shown in Fig. 2.3 as a function of η . The kink-gas approximation works only for a dilute gas of pseudo-particles, hence the kink distance has to be larger than its size and one is bound to the $\eta \gg 2$ in this numeric example.

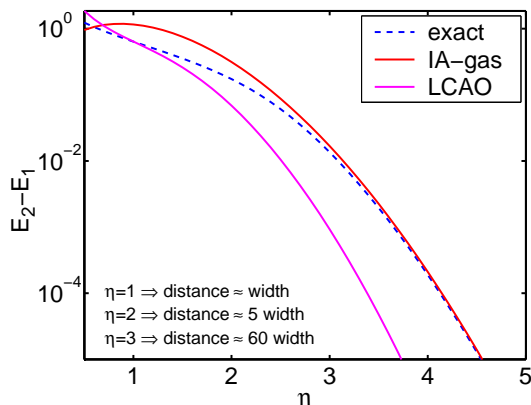


Figure 2.3: The mass gap in the kink-gas approximation. The approximation becomes asymptotically exact for small couplings, has parity and the exponential tail of the gap, which is a feature of the exact solution.

One can see that this approximation becomes good for small couplings and describes the exponential tail of the gap as it is predicted by the (numerical) exact solution. Of course there is still much space for improvement of this method e.g. kink interaction or higher loop calculations. For example the lowest energy E_1 is not exponentially close to $\hbar\omega/2$ at all!

2.5 Numerical results for the double-well

The general theoretical explanations are supplemented by numerical calculations which show further aspects of the semiclassical approximation of the double-well potential. First the exact results are presented. They are meant to support the analytical results from the previous sections. The second part consists of results of a Monte-Carlo study of 2-point correlation functions. In the last part of this section streamline configuration will be inspected and it will be argued, how one could numerically determine, whether a semiclassical approach is feasible or not.

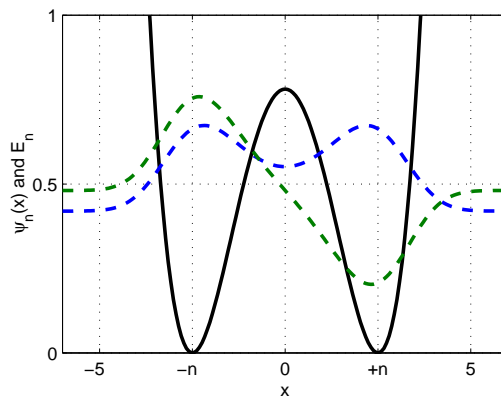


Figure 2.4: eigenfunctions of double-well Hamiltonian with $m = \omega = 1$ and $\eta = 2.5$

In Fig. 2.4 the two lowest eigenfunctions are shown. The corresponding energy levels are shown as the global offset of the wave function. The results (Tab. 2.1 and Fig. 2.4) were calculated by computing the spectrum of a discretised Hamiltonian operator with MATLAB. The kinetic term $\hat{p}^2/2$ was implemented using the Fourier transform of an exact lattice Laplacian Eq. 2.17. Whether the result is numerical exact was checked by varying the lattice extent L (the lower bound for L depends on η) and the number of lattice points ranging from $N = 200$ to $N = 300$. Due to the limited numerical (double) precision no calculations are possible for $\eta < 7$.

$$\begin{aligned}
 (\mathcal{H})_{kl} &= \left(\frac{\hat{p}^2}{2} \right)_{kl} + \frac{\delta_{kl}}{8\eta^2} (\hat{x}_l^2 - \eta^2)^2 \quad \text{with} \quad (\hat{p}^2)_{kl} = \frac{1}{N} \sum_p p^2 \exp[i p (\hat{x}_k - \hat{x}_l)] \\
 p &\in \frac{\pi}{2L} [-N, -N+2, \dots, N-2] \quad \text{and} \quad \hat{x}_k = -L + \frac{2kL}{N}
 \end{aligned} \tag{2.17}$$

Since the matrix $(\mathcal{H})_{kl}$, where the indices k and l run from 1 to N , assumes periodic boundary conditions for the kinetic part, its spectrum for the non-periodic case can only be correct if the wave function drops fast enough at the boundary. In Tab. 2.1 the results for various values of η are shown.

η	1.0	2.5	5.0
E_1	0.293298	0.419809	0.489498
$E_2 - E_1$	0.641225	0.060942	$6.1175 \cdot 10^{-7}$

Table 2.1: Numerical (exact) results for double-well potential with $\hbar = m = \omega = 1$

This should be compared with the results from numerical simulation. Since the ultimate technique to obtain results in quantum field theory is the path-integral approach using Monte-Carlo techniques it is worth to consider this approach in quantum mechanics. Assume one creates a set of N uniformly and independently path $x(\tau)_n$ which are distributed randomly. An expectation value of an observable \hat{O} is then calculated by

$$\langle \hat{O} \rangle = \frac{1}{N} \sum_n O[x_n] \exp[-S[x_n]]$$

where $O[x]_n$ is the classical quantity measured on a path of the Monte-Carlo ensemble. This method is called straight sampling. This method is very inefficient, since the weight $e^{-S[x_n]}$ is strongly peaked in the configuration space, and most paths do not contribute to the expectation value. In the forthcoming analysis the set of paths (Monte-Carlo ensemble) is already distributed according to the Boltzmann-law $P(x_n) \propto \exp[-S[x_n]]$ (importance sampling). Hence the probability to have a path with the action $S[x]$ is $P(x)$. For comparison with the exact results the cases $\eta = 1.0$ and $\eta = 2.5$ are chosen. To calculate the energy gap one usually measures the exponential tail of the connected 2-point correlation function, in this case

$$\langle \hat{x}(\tau)\hat{x}(\tau + T) \rangle - \langle \hat{x}(\tau) \rangle \langle \hat{x}(\tau + T) \rangle \stackrel{T, L \rightarrow \infty}{\propto} \exp[-(E_2 - E_1)T].$$

On a periodic lattice this has to be changed to a $\cosh((E_2 - E_1)(T - L/2))$ function, since the 2-point function is symmetric for $T \rightarrow L - T$. Using this fit function the following results emerge from the Monte-Carlo simulation⁶.

η	$E_2 - E_1$ (fit)	χ^2/DOF
1.0	(0.640 ± 0.007)	0.7
2.5	(0.063 ± 0.005)	1.1

Table 2.2: Results from Monte-Carlo simulation

The two 2-point function, measured on the periodic lattice is shown in Fig. 2.5.

The next step is to show some properties of the classical solution numerically and to discuss, whether respectively when the semiclassical approach is reliable. For this purpose the Monte-Carlo configurations for the double-well potential are used as the starting point. To obtain the streamlines from those configurations one applies some smoothing, which means that the local action is iteratively minimised (or lowered) by substitutions with a small 'time' step ϵ

$$x_{t+\epsilon}(n) = x_t(n) - \epsilon \left[\frac{2x_t(n) - x_t(n+1) - x_t(n-1)}{a} + aV'(x_t(n)) \right].$$

The dynamics introduced for the quantity t has no physical meaning and the streamlines should be thought as a point in function space, where the semiclassical approximation can be performed. This process of removing short range fluctuations is also known as *cooling*, *smoothing* or *smearing* in the literature [41–43]. In [32] the author argues, that for consistency of a semiclassical approach one needs a scale separation into 'slow' (small) and 'fast' (large) modes of the Hessian.

In particular the author concludes that self-consistency can be established through the spectrum of the Hessian if

1. there is a gap that divides eigenvalues into small and large ones;
2. the spreading among the small eigenvalues is small relative to the gap.

⁶**Note:** For $\eta = 1.0$ we have chosen $\Delta\tau = 0.04$, $\beta = 20$ and for $\eta = 2.5$ the lattice spacing $\Delta\tau = 0.4$ and $\beta = 200$. $\hbar = \omega = m = 1$

It is clear that 'excessive' smoothing ($t \rightarrow \infty$) will lead to a classical path with such properties. That's why a physical quantity, like a 2-point correlation function, has to be monitored while cooling to ensure, that it is not biased by too excessive smoothing. The observable can be insensitive to a certain amount of cooling and the smoothed trajectory obtained then is the streamline, which lies halfway between classical and Monte-Carlo trajectories.

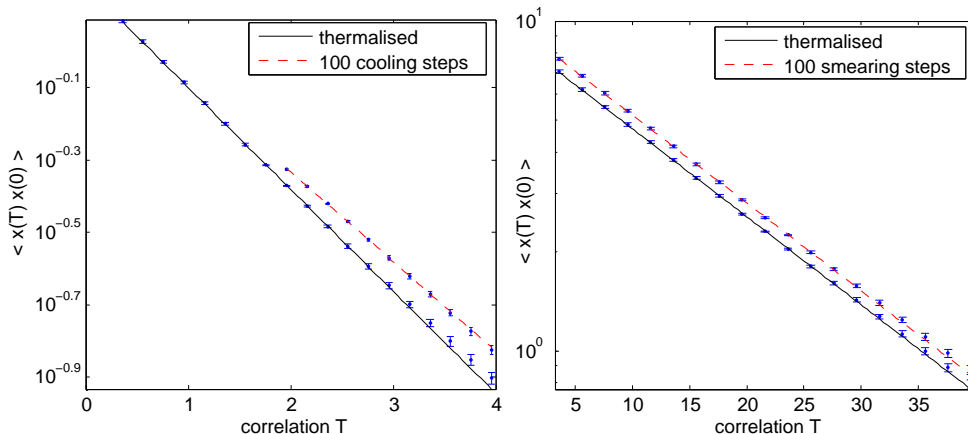


Figure 2.5: two-point function for $\eta = 1.0$ (left) and $\eta = 2.5$ (right)

From the fit to the Monte-Carlo data, shown in Tab. 2.3, it becomes clear that the result for the two-point function, which is in agreement with the exact value, is not affected by cooling in the weak coupling regime. Both correlations functions are perfectly parallel. This is in correspondence to the statement of self-consistency for the semiclassical approach in the weak coupling regime, if the Hessian shows the scale separation. The result for strong couplings is heavily effected by the 100 smoothing steps. The would-be energy gap, measured after 100 smoothing steps in the strong coupling regime, deviates by 26σ from the exact value.

η	exact	$(E_2 - E_1)_{MC}$	$(E_2 - E_1)_{100}$
1.0	0.641225	(0.646 ± 0.005)	(0.538 ± 0.004)
2.5	0.060942	(0.061 ± 0.003)	(0.061 ± 0.005)

Table 2.3: comparison of energy gap

In order to elucidate the reasons for success in the weak coupling case, we extend the investigation of the semiclassical properties somewhat further. Especially the spectrum of the Hessian is of interest now. If it shows a separation of scales, following the arguments of Huang [32], the semiclassical approach is consistent for weak couplings (because the gap resisted to the smoothing).

In Fig. 2.6 typical trajectories after a number of cooling steps are shown. For weak couplings (left panel) the dilute kink(s), modulated by oscillations, are already visible in the thermalised path. The trajectories are also smooth in the strong coupling regime, but there are no typical kink solutions visible (right panel).

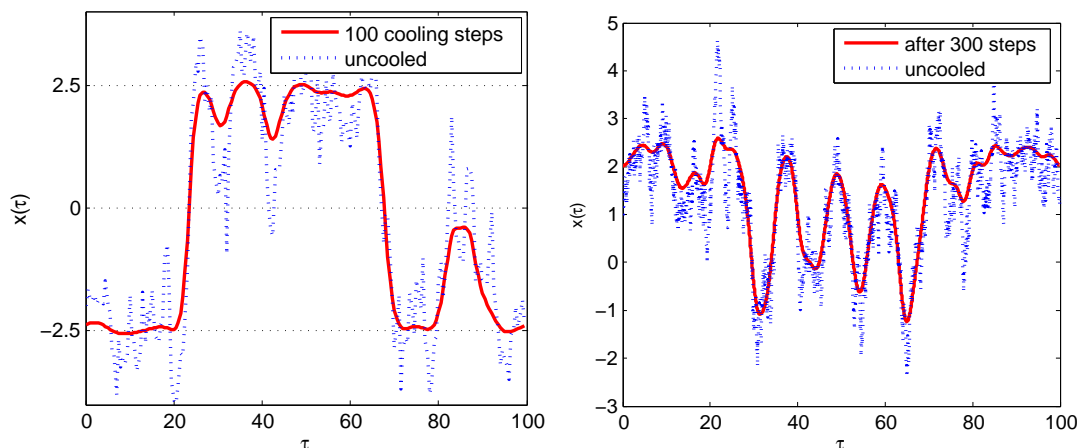


Figure 2.6: typical trajectories from MC ensemble and after cooling for weak coupling $\eta = 2.5$ (left) and for strong coupling $\eta = 1.0$ (right)

It is impossible to find a gap in the spectral density, which is averaged over 1000 configurations, in Fig. 2.7 without cooling. Nevertheless, after some cooling steps the spectrum of the Hessian shows a scale separation. The narrow peak of almost-eigenvalues is separated from the higher eigenvalues. This shows the self-consistency of the semiclassical approach for the energy gap in the weak coupling regime. Similar observations have been made by Huang [32].

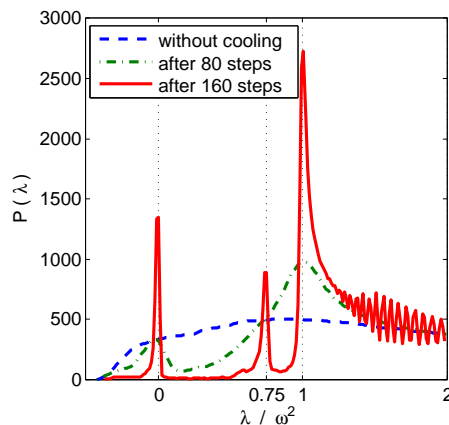


Figure 2.7: spectral density of the Hessian $\delta^2 S$ for various stages of cooling (averaged over 1000 trajectories with $\Delta\tau = 0.4$, $\beta = 200$, $\hbar = \omega = m = 1$ and $\eta = 2.5$ (weak coupling))

The numerical investigation is completed by showing some properties of the classical kink solution. Especially the spectrum of the Hessian operator in the background of a kink is interesting. The operator Eq. 2.11, with the Laplacian taken from Eq. 2.17, is diagonalised and the lowest eigenmodes are illustrated in in Fig. 2.8.

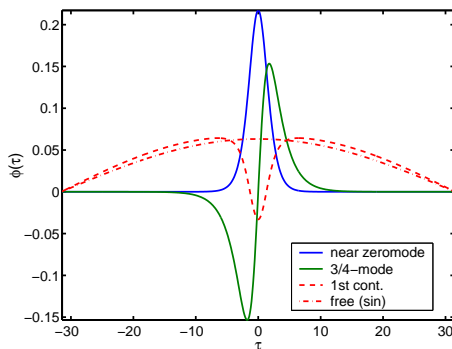


Figure 2.8: 3 eigenmodes of \mathcal{M} and one of \mathcal{M}_ω

The spectrum contains two isolated eigenmodes $\lambda_0 = 0$ and $\lambda_1 = 3/4\omega^2$, and a continuous spectrum for $\lambda \geq \omega^2$. The zero-mode is localised on the kink position $\tau_0 = 0$. Higher modes look like their free counterparts but are influenced by the zero-mode. Continuum modes can be identified by a inverse participation ratio $IPR = V \sum_x (\bar{\psi}(x)\psi(x))^2$ close to one. Due to the finite time interval β the zero mode of one kink will be lifted to a near zero mode (exponential small). The interaction of a kink and an anti-kink will drag the zero-mode to negative values. This effect can actually be seen in Fig. 2.7 which is an average over Monte-Carlo trajectories with different amount of smoothing. The λ_0 and λ_1 modes are enhanced after 160 cooling steps. After 80 steps the gap is also already visible. In Fig. 2.9 one can compare the spectrum of the Hessian of the harmonic oscillator, which is continuous in the continuum and independent from a trajectory, with the Hessian of the double-well oscillator in the background of a single kink, where two bound states are also visible. The similarity between of the lower right figure in Fig. 2.9 and the spectral density in Fig. 2.7 is remarkably clear.

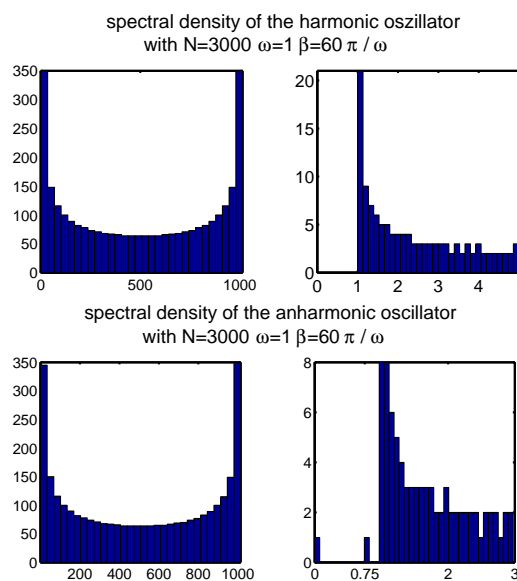


Figure 2.9: Hessian of harmonic and anharmonic oscillator, left figures show full spectrum, right figures only the low lying end

The semiclassical approach to QCD has very similar features. Having understood this toy model helps to formulate what one can expect from a semiclassical approach to Yang-Mills theory.

2.6 Lessons for QCD

This extended analysis of the quantum mechanical path integral shows that there exist some non-perturbative effects, which can be described by a semiclassical approximation. One alternative approach to Schrödinger's quantum mechanics is given by the path integral approach, which can be studied using Monte-Carlo techniques. The discretisation of time (and space in QFT) is natural for the path integral. It is unavoidable for the lattice formulation. In this approach the semiclassical approach (saddle point method) can be examined. The straight forward calculation is accompanied by zero-modes associated with symmetries of the classical solution. Whether this approach is applicable depends on whether there exists some scale separation that allows one to divide the problem into a classical and a 'fluctuating' part. Numerically this can be decided by evaluating the spectrum of the corresponding Hessian $\delta^2 S / \delta\phi(\tau)\delta\phi(\tau')$. This separation is enhanced by cooling out UV fluctuations around the more or less fuzzy path and simultaneously observing the physical quantity, e.g. a correlator, of interest as a function of smearing steps. If the observable of interest is not affected by this smoothing the semiclassical approach is likely to work for this quantity, if one considers the corresponding streamline paths as a starting point for the saddle-point method. One must be especially cautious since this method might fail in some regime like it does for the strongly coupled double-well oscillator!

Since solving the equation of motions for the $SU(3)$ gauge theory is difficult on itself it is convenient to use the smoothing technique to obtain solutions of the equation of motion which are the 'kinks' of QCD. This method, the so-called cooling method, is used throughout the whole work to study classical solutions of $SU(3)$ lattice gauge theory.

With the help of the semiclassical method some effects like chiral symmetry breaking were already successfully described in QCD but there is the open question whether one can describe the property of confinement within this framework. Some hopes are laid on a new type of solution. But first the basic notions of non-Abelian gauge theory and the little 'zoo' of its classical solutions need to be introduced.

Chapter 3

Classical $SU(3)$ gauge fields

In this chapter the classical $SU(3)$ Yang-Mills theory at finite temperature is introduced for continuum gauge fields. The classical solutions for the Euclidean space \mathbb{R}^4 and for finite temperature $S^1 \times \mathbb{R}^3$ are introduced in a concise way and their properties described. Finally the status of the semiclassical quantisation, especially for finite temperature and non-trivial holonomy, is reviewed.

3.1 Classical $SU(3)$ gauge theory

The semiclassical approach to a gauge theory starts with the same ingredients like in quantum mechanics. First solutions of the classical equations of motion need to be found. In non-Abelian field theory, however, topological properties enter the construction of *classical fields* and the equations of motion are difficult to solve. The dynamical variables of the $SU(3)$ gauge theory are eight real-valued vector potentials A_μ^a which form an anti-hermitian gauge field

$$A_\mu(x) = igA_\mu^a(x) T^a \quad a \in \{1, \dots, 8\}.$$

In case of finite temperature x is defined on $[0, \beta] \times \mathbb{R}^3$ and the gauge fields are in the periodic gauge such that $A_\mu(x + \hat{t}\beta) \equiv A_\mu(x)$. For zero temperature x is defined on \mathbb{R}^4 . The hermitian generators T^a (Gell-Mann matrices) of the $SU(3)$ algebra obey $\text{tr}(T^a T^b) = \frac{1}{2} \delta_{ab}$. With the induced covariant derivative $D_\mu = \partial_\mu + A_\mu(x)$ the field strength is

$$F_{\mu\nu}(x) := [D_\mu, D_\nu] = \partial_\mu A_\nu(x) - \partial_\nu A_\mu(x) + [A_\mu(x), A_\nu(x)]. \quad (3.1)$$

Under a gauge transformation $\Omega(x) \in SU(3)$ these quantities transform as

$$A_\mu(x) \xrightarrow{\Omega} \Omega^\dagger(x) (A_\mu(x) + \partial_\mu) \Omega(x) \quad \text{and} \quad F_{\mu\nu}(x) \xrightarrow{\Omega} \Omega^\dagger(x) F_{\mu\nu}(x) \Omega(x).$$

With these definitions the Euclidean action of the $SU(3)$ Yang-Mills theory is defined

$$S_{YM}[A] := -\frac{1}{2g^2} \int d^4x \text{tr}(F_{\mu\nu}(x) F_{\mu\nu}(x)). \quad (3.2)$$

and the equations of motion, which follow from a variational principle, are

$$\frac{\delta S}{\delta A_\mu} = 0 \quad \Rightarrow \quad [D_\mu, F_{\mu\nu}] = 0. \quad (3.3)$$

To have a solution of the equations of motion it is sufficient but not necessary that the field is self-dual or anti-selfdual. This means that the dual field strength $\tilde{F}_{\mu\nu} = \frac{1}{2}\epsilon_{\mu\nu\rho\sigma} F_{\rho\sigma}$ is up to a sign equal to the field strength itself.

In the spirit of mathematical literature mainly (anti) self-dual gauge fields are considered in this work. Of main interest are the classical solutions of $SU(3)$ Yang-Mills theory at finite temperature. This corresponds to $S^1 \times \mathbb{R}^3$ as the base space of the gauge fields. Self-dual or anti self-dual gauge connections for finite temperature are called *calorons*. The analytical knowledge of the caloron *moduli space* or parameter space regarding classical solutions with non-trivial holonomy was extended short time ago by Kraan-van Baal and Lee-Lu [20, 21]. The description is a subject of current investigations, both from a numerical [25, 29] and an analytical [24, 44] point of view. The ansatz of this work is to obtain classical gauge fields on the lattice by relaxing the fields using the cooling method. This makes it possible to obtain all classical solutions which are compatible with the boundary conditions, are numerically stable on the discretised space time and which are tolerated by the cooling method.

Within this framework it is not possible to obtain analytic expressions but this is also not the purpose of this study. Rather the moduli space of classical solutions can be explored and checked whether the analytical description of classical solutions is complete and understood. It is argued that the description in terms of calorons with trivial holonomy is incomplete and should be extended for a semiclassical description just below the deconfinement transition.

To accomplish this task gauge invariant quantities, which show a characteristic behaviour for the different classes of classical solutions, are studied and compared to the known analytical formulae. The quantities which are used here are the topological charge Q , the action S , the Polyakov loop \mathcal{P} and the spectrum of the massless Dirac operator with the background field A_μ . These quantities also need to be introduced on the lattice, but their significance and definition is underlined here. The Yang-Mills action was already introduced. Like in quantum mechanics the pseudo-particle solutions are localised and will show up as a peak in the action density. For (anti) self-dual gauge fields the action is proportional to the topological charge

$$Q[A_\mu] := -\frac{1}{32\pi^2} \int d^4x \operatorname{tr} \left(\tilde{F}_{\mu\nu}(x) F_{\mu\nu}(x) \right) \in \mathbb{Z}. \quad (3.4)$$

The topological charge is an integer for every smooth, but not necessarily classical, gauge field if only some weak conditions hold¹. In this case Q just represents the mapping degree from the base space to the group space and gives, properly normalised, an integer.

¹For example finite action is sufficient for \mathbb{R}^4 .

For finite temperature the Polyakov loop operator

$$\mathcal{P}(\vec{x}) := \text{P.O.} \exp \left[\int_0^\beta A_0(\tau, \vec{x}) d\tau \right] \quad (3.5)$$

characterises classical gauge fields. Since the Polyakov loop transforms under a gauge transformation as $\Omega^\dagger(x) \mathcal{P}(\vec{x}) \Omega(x + \beta\hat{t})$ the trace

$$P(\vec{x}) := \frac{1}{3} \text{tr}(\mathcal{P}(\vec{x})) \quad (3.6)$$

is invariant under gauge transformations. The holonomy in the periodic gauge is defined as

$$\mathcal{P}_\infty := \lim_{|\vec{x}| \rightarrow \infty} \mathcal{P}(\vec{x}) = \Omega^\dagger(\vec{x}, 0) \exp [2\pi i \text{diag}(\mu_1, \mu_2, \mu_3)] \Omega(\vec{x}, \beta). \quad (3.7)$$

The eigenvalues $\{\mu_m\}$ and the trace $P_\infty := \text{tr}(\mathcal{P}_\infty)/3$ of \mathcal{P}_∞ are gauge invariant. Topological properties of a gauge field are also encoded in the spectrum of the massless Dirac operator. The massless Dirac operator in the background of a gauge field A_μ is defined

$$\mathcal{D} := \gamma^\mu (\partial_\mu + A_\mu(x)). \quad (3.8)$$

The operator \mathcal{D} acts on spinor fields $\psi(x)$ which carry a further spinor and a colour index. For finite temperature QCD the spinor fields have to obey anti-periodic boundary conditions. However, as a diagnostic tool for gluodynamics the influence of temporal fermionic boundary conditions

$$\psi(x + \beta\hat{t}) = \exp [2\pi i\xi] \psi(x) \quad (3.9)$$

on the spectrum can be studied. Like in the quantum mechanical example especially the zero-modes $\psi^{(0)}(x)$ of the Dirac operator are interesting to study. Since γ_5 anti-commutes with the Dirac operator, the zero-modes can be chosen to be eigenfunctions of γ_5 with eigenvalue $\gamma_5 \psi^{(0)} = \pm \psi^{(0)}$. The number of eigenvalues with positive (negative) γ_5 eigenvalue are denoted by n_+ (n_-). The difference $n_- - n_+$, formally known as the index of \mathcal{D} , can be written as $-\text{tr}(\gamma_5[U]) = n_- - n_+$ and is connected to the topological charge Q by the famous Atiyah-Singer index theorem [45]

$$n_- - n_+ = Q. \quad (3.10)$$

The trace is to be taken over spinor, colour and spacetime indices of the zero-modes of the Dirac operator \mathcal{D} . In order to study localisation properties of classical solutions it is interesting to study the zero-mode density $\rho = \psi^\dagger \psi$ and the chiral density $\chi = \psi^\dagger \gamma_5 \psi$ of the zero-mode. With the normalised action density $s(x)$ and topological density $q(x)$

$$\frac{s(x)}{S_0} := -\frac{1}{32\pi^2} \text{tr}(F_{\mu\nu} F_{\mu\nu}) \quad q(x) := -\frac{1}{32\pi^2} \text{tr}(F_{\mu\nu} \tilde{F}_{\mu\nu}) \quad (3.11)$$

and the three-dimensional Polyakov loop these densities can be used to pinpoint a localised pseudo-particle solution of classical equation of motions and to classify classical gauge fields.

The next sections give an overview about the analytical knowledge of classical solutions with trivial and non-trivial holonomy. The expressions for the gauge fields are restricted to $SU(2)$, where a uniform presentation is sought.

3.2 Calorons in $SU(2)$

The instanton solution was found in 1975 by Belavin, Polyakov, Schwartz and Tyupkin as a regular, non-trivial solution of Euclidean Yang-Mills theory with finite action and topological charge $Q = 1$ [11]. The instanton is a localised pseudo-particle in \mathbb{R}^4 and its existence results from the inequality between the action and topological charge

$$S[A_\mu] \geq \frac{8\pi^2}{g^2} |Q| \quad Q[A_\mu] \in \mathbb{Z}.$$

The inequality settles for an (anti) self-dual gauge field with topological charge Q with $S = |Q|S_0$. The action is quantised in units of $S_0 := 8\pi^2/g^2$. An expression for the gauge field in the singular gauge is given by

$$A_\mu(x) = \frac{\tau_a}{2} \bar{\eta}_{\mu\nu}^a \partial_\nu \ln \left(1 + \frac{\rho^2}{(x-y)^2} \right) \quad (3.12)$$

where the 't Hooft symbols $\bar{\eta}_{\mu\nu}^a$ [46] and the generators $\tau_a/2$ of the $SU(2)$ algebra are used. The 4 dimensional position is given by $y = (t_0, \vec{y})$ and the size of the instanton is ρ . To have a uniform presentation of the gauge fields the following notation is used

$$A_\mu(x) = \frac{\tau_3}{2} \bar{\eta}_{\mu\nu}^3 \partial_\nu \ln \phi + \frac{1}{2} \phi \operatorname{Re} \left((\bar{\eta}_{\mu\nu}^1 - i\bar{\eta}_{\mu\nu}^2)(\tau_1 + i\tau_2) \partial_\nu \chi \right). \quad (3.13)$$

With these definition the instanton gauge field is expressed through

$$\begin{aligned} \phi(x) &= \frac{\psi(x)}{\hat{\psi}(x)} = 1 + \frac{\rho^2}{(x-x_0)^2} \\ \psi(x) &= 2\pi^2 \left((x-y)^2 + \rho^2 \right), \quad \hat{\psi}(x) = 2\pi^2 (x-y)^2 \\ \chi(x) &= 1 - \frac{1}{\phi} = \frac{2\pi^2 \rho^2}{\psi} \end{aligned} \quad (3.14)$$

The caloron with trivial holonomy was found by Harrington and Shepard by putting a chain of instantons with same colour orientation onto \mathbb{R}^4 with same spatial positions but separated by β in time [18]. The periodic solution can be written as a generalisation of Fig. 3.14.

$$\begin{aligned} \phi &= 1 + \sum_{k=-\infty}^{\infty} \frac{\rho^2}{(\vec{x} - \vec{y})^2 - (x_4 - (t_0 + k\beta))^2} \\ &= 1 + \frac{\pi\rho^2}{\beta r} \frac{\sinh(2\pi r/\beta)}{\cosh(2\pi r/\beta) - \cos(2\pi t/\beta)} \end{aligned} \quad (3.15)$$

with the abbreviation $r = |\vec{x} - \vec{y}|$ and $t = x_0 - t_0$. The periodicity of this solution is $\beta = T^{-1}$. For simplicity $\beta = 1$ is set throughout the following formulas. The potentials for the caloron with trivial holonomy are then given by

$$\begin{aligned}
\phi(x) &= \frac{\psi(x)}{\hat{\psi}(x)} = 1 + \frac{\pi\rho^2}{r} \frac{\sinh(2\pi r)}{\cosh(2\pi r) - \cos(2\pi t)}, \\
\psi(x) &= \cosh(2\pi r) - \cos(2\pi t) - \frac{\pi\rho^2}{r} \sinh(2\pi r), \quad \hat{\psi}(x) = \cosh(2\pi r) - \cos(2\pi t), \\
\chi(x) &= 1 - \frac{1}{\phi} = \frac{\pi\rho^2 \sinh(2\pi r)}{r\psi}.
\end{aligned} \tag{3.16}$$

The asymptotic Polyakov loop reaches $\mathcal{P}_\infty = 1$ and the Polyakov loop at the position of the caloron takes the value $\mathcal{P}(\vec{y}) = -1$. Classical solutions given until here are described in terms of 5 parameters. An additional rotation in colour space can be interpreted as a global gauge transformation. As soon as one deals with multi-instanton solutions these degrees of freedom become important.

Atiyah et. al. [47] created a framework for the construction of generic (anti) self-dual fields with arbitrary topological charge, known as ADHM construction. Due to the ADHM formalism the complete construction of instantons is in principle reduced to some linear algebra but the moduli space of instantons is only known for a limited number of spaces. Hence it is particularly interesting to explore the parameter space of classical solution also from the numerical point of view. In the case of $SU(2)$ they predict (anti) self-dual gauge fields with topological charge Q which depend on $8|Q|$ parameters from parameter counting arguments. These parameters might be interpreted as position, size and colour orientation. But the instantons, lined up to build the Harrington-Shepard caloron, have the same colour orientation. The generalisation for $|Q| = 1$ is to introduce a relative colour rotation $4\pi\omega$. This parameter ω is actually given by the holonomy $\mathcal{P}_\infty = \exp[2\pi i\omega\tau_3]$ of the $SU(2)$ gauge field. In contrast to the calorons with trivial holonomy, classical solutions with non-trivial holonomy were constructed only relatively recently [20, 21]. This solution is parametrised by the potentials

$$\begin{aligned}
\phi(x) &= \frac{\psi}{\hat{\psi}}, \quad \chi = e^{4\pi i t \omega} \frac{\pi\rho^2}{\psi} \left\{ e^{-2\pi i t} s^{-1} \sinh(4\pi s \omega) + r^{-1} \sinh(4\pi r \bar{\omega}) \right\}, \\
\psi(x) &= \cosh(4\pi r \bar{\omega}) \cosh(4\pi s \omega) + \frac{(r^2 + s^2 + \pi^2 \rho^4)}{2rs} \sinh(4\pi r \bar{\omega}) \sinh(4\pi s \omega) - \cos(2\pi t) \\
&\quad + \pi\rho^2 \left\{ s^{-1} \sinh(4\pi s \omega) \cosh(4\pi r \bar{\omega}) + r^{-1} \sinh(4\pi r \bar{\omega}) \cosh(4\pi s \omega) \right\}, \\
\hat{\psi}(x) &= \cosh(4\pi r \bar{\omega}) \cosh(4\pi s \omega) + \frac{(r^2 + s^2 - \pi^2 \rho^4)}{2rs} \sinh(4\pi r \bar{\omega}) \sinh(4\pi s \omega) - \cos(2\pi t).
\end{aligned} \tag{3.17}$$

This expression is in the so-called algebraic gauge $A_\mu(\vec{x}, t + \beta) = \mathcal{P}_\infty A_\mu(\vec{x}, t) \mathcal{P}_\infty^\dagger$. Using a non-periodic gauge transformation one can express the gauge field in the periodic gauge using $\tilde{\chi} = e^{-4\pi i t \omega} \chi$

$$A_\mu = \frac{\tau_3}{2} \bar{\eta}_{\mu\nu}^3 \partial_\nu \ln \phi + \frac{\phi}{2} \operatorname{Re} \left((\bar{\eta}_{\mu\nu}^1 - i\bar{\eta}_{\mu\nu}^2) (\tau_1 + i\tau_2) (\partial_\nu + 4\pi i \omega \delta_{\nu 0}) \tilde{\chi} \right) + \delta_{\mu 0} 2\pi i \omega \tau_3. \tag{3.18}$$

The holonomy parameters ω and $\bar{\omega}$ in this formula are related by $\bar{\omega} = 1/2 - \omega$ and $0 \leq \omega \leq 1/2$. The distances to the constituent cores are $r = |\vec{x} - \vec{y}_1|$ and

$s = |\vec{x} - \vec{y}_2|$ and the distance between the constituents is $\pi\rho^2/\beta = d = |\vec{y}_1 - \vec{y}_2|$. In the limit $\omega \rightarrow 0$ or $\bar{\omega} \rightarrow 0$ the Harrington-Shepard caloron of Eq. 3.16 is obtained. If the centres are well separated $d \gg 1$ one will obtain two static constituents, where $\omega/8\pi^2$ and $\bar{\omega}/8\pi^2$ are the masses of the constituents. The action density for all previous solutions is given by the formula

$$s(x) = -\frac{1}{2} \partial^2 \partial^2 \ln \psi(x). \quad (3.19)$$

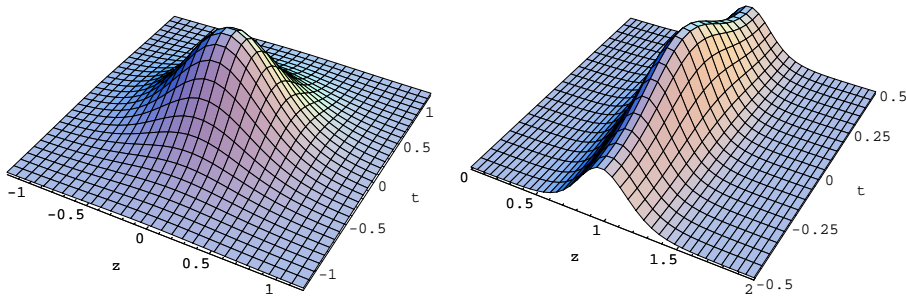


Figure 3.1: action densities of an BPST instanton (left) and for an Harrington-Shepard caloron (right) in the $z - t$ plane with $x = y = 0$; ($\rho = 0.8\beta$ for caloron). (figure taken from [23])

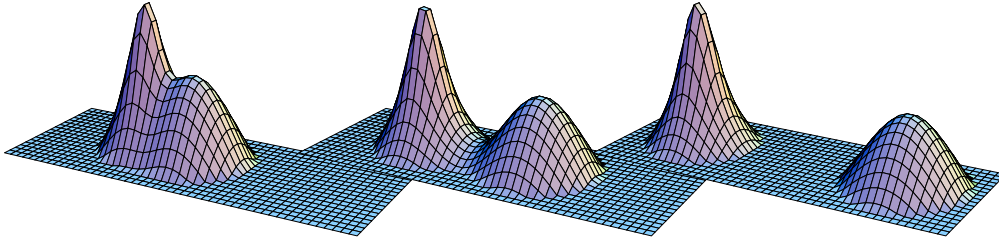


Figure 3.2: action density (logarithmic scale) of a $SU(2)$ caloron with non-trivial holonomy $\mu_2 = \mu_1 = 0.125$ $\rho = 0.8, 1.2, 1.6\beta$ (left, right, middle) (figure taken from [48])

The action density of the instanton solution is $O(4)$ symmetric solution while the Harrington-Shepard caloron only has $O(3)$ symmetry (see Fig. 3.1). The KvBLL calorons with non-trivial holonomy, are even less symmetric in the generic case. The action-density of the caloron with non-trivial holonomy in Fig. 3.2 shows a dissociation into constituents.

This short overview for $SU(2)$ might have given the impression, that the moduli space for the investigation of $SU(3)$ gauge fields with $|Q| = 1$ is known now. But this is not the case since the general solution for $SU(3)$ cannot be described in terms of the $SU(2)$ caloron, but it is contained in a suitable limit. The $SU(3)$ caloron is not just an embedding but an extension of the $SU(2)$ caloron solution.

That is the reason why it is also necessary to analyse the $SU(3)$ KvBLL caloron on its own.

3.3 Calorons in $SU(3)$

The $SU(3)$ $|Q| = 1$ caloron depends on 12 parameters [49, 50]. These are three positions \vec{y}_n (9 parameter) of the so-called constituent monopoles and the three eigenvalues of the asymptotic holonomy $\mu_{1,2,3}$ (2 independent parameter). The missing parameter is a shift is the S^1 coordinate of the caloron (1 parameter). Coming from the abstract ADHM construction these parameter do not need to have an obvious interpretation in terms of shape parameters of the caloron, like it is the case for the BPST instanton. However, if the constituent monopoles are well separated, the constituent positions \vec{y}_n can be identified by one of the following criteria [51]:

1. Spatial points \vec{x} where the eigenvalues of the Polyakov loop $\mathcal{P}(\vec{x})$ coincide.
2. The centres of mass of (spherical) lumps of action.
3. As Abelian monopoles, e.g. as a defect of the maximal Abelian gauge.

In this study extensive use of the first criterion is made since it allows to detect several monopoles inside one (anti)self-dual lump of action. For definiteness the eigenvalues of the asymptotic holonomy $\mathcal{P}_\infty \simeq \text{diag}(e^{2\pi i\mu_1}, e^{2\pi i\mu_2}, e^{2\pi i\mu_3})$ are ordered $\mu_1 \leq \mu_2 \leq \mu_3 \leq \mu_4$ with $\mu_4 := 1 + \mu_1$ and are normalised $\sum_{n=1}^3 \mu_n = 0$. This ensures that the masses $8\pi^2\nu_n$, defined by $\nu_n := \mu_{n+1} - \mu_n$, add up to one instanton unit. If two eigenvalues of the asymptotic holonomy coincide, one constituent becomes massless and the $SU(2)$ KvBLL caloron is recovered. In the case of three coinciding eigenvalue the asymptotic holonomy is in the center of $SU(3)$ and two constituents are massless. In this limit the ordinary Harrington-Shepard caloron is obtained. In case of $SU(2)$ the two eigenvalues of \mathcal{P} degenerate only for $\mathcal{P} = \pm 1$, which marks the constituent position \vec{y}_n by $P(\vec{y}) = \pm 1$ then. The range of the trace P of the $SU(3)$ Polyakov loop in the the complex plane is shown in Fig. 3.3.

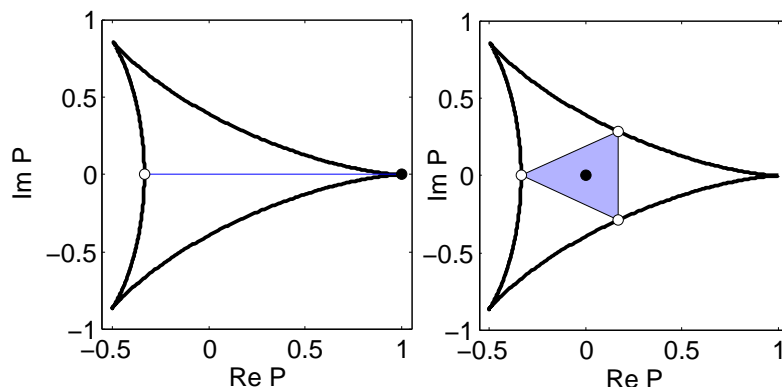


Figure 3.3: Polyakov loop in the complex plane; schematic distribution of Polyakov loop for a caloron with trivial (left) and non-trivial (right) asymptotic holonomy

If two of the eigenvalues coincide the value of the trace will lie on the boundary of the triangle. If the holonomy \mathcal{P}_∞ is in the centre $Z(3) = \{1, e^{\pm 2\pi i/3}\}$ of $SU(3)$, the value of its trace P_∞ will lie on one of the outer edges of the triangle and the holonomy is

said to be *trivial*. The case $\text{tr}(\mathcal{P}_\infty) = 0$ (filled circle in right figure) is the so-called maximally *non-trivial holonomy*. The Polyakov loop, calculated for the analytic $SU(3)$ caloron gauge field with separated monopole constituents, degenerates at the positions of the constituent monopoles [52] \vec{y}_n with

$$\begin{aligned} P(\vec{y}_1) &= \text{diag}(e^{-\pi i \mu_3}, e^{-\pi i \mu_3}, e^{2\pi i \mu_3}), \\ P(\vec{y}_2) &= \text{diag}(e^{2\pi i \mu_1}, e^{-\pi i \mu_1}, e^{-\pi i \mu_1}), \\ P(\vec{y}_3) &= \text{diag}(-e^{-\pi i \mu_2}, e^{2\pi i \mu_2}, -e^{-\pi i \mu_2}). \end{aligned} \quad (3.20)$$

In Fig. 3.3 the asymptotic holonomy of trivial holonomy (left) and maximally non-trivial holonomy (right) and the Polyakov loop at the constituent positions is shown by the black and white circles. The (left) plot in Fig. 3.3 sketches the distribution of the Polyakov loop for an embedded Harrington-Shepard caloron while the right is a $SU(3)$ caloron with maximally non-trivial holonomy. For $SU(2)$ it is known that the points where the eigenvalues of \mathcal{P} coincide will shift outwards from the constituent positions, while the centres of mass shifts inwards (e.g. [52] Fig. 2). Hence the correspondence between the position of a constituent monopole and the position where \mathcal{P} degenerates is not exact.

The construction of the $|Q| = 1$ KvBLL caloron also provides an analytic formula for the action density for $SU(N)$ in general. In particular the caloron potential $\psi(x)$ for $SU(3)$, which is needed to construct action density according to Eq. 3.19, is expressed

$$\begin{aligned} \psi(x) &:= \frac{1}{2} \text{tr}(\mathcal{A}_3 \mathcal{A}_2 \mathcal{A}_1) - \cos(2\pi t/\beta), \\ \mathcal{A}_m &:= \frac{1}{r_m} \begin{pmatrix} r_m & |\vec{\rho}_{m+1}| \\ 0 & r_{m+1} \end{pmatrix} \begin{pmatrix} \cosh(2\pi \nu_m r_m/\beta) & \sinh(2\pi \nu_m r_m/\beta) \\ \sinh(2\pi \nu_m r_m/\beta) & \cosh(2\pi \nu_m r_m/\beta) \end{pmatrix} \end{aligned} \quad (3.21)$$

with the definitions $r_m \equiv |\vec{x} - \vec{y}_m|$ and $\vec{\rho}_m \equiv \vec{y}_m - \vec{y}_{m-1}$. It is sufficient that two constituents are separated, that $\cos(2\pi t/\beta)$ in $\psi(x)$ can be neglected and the first term dominates the action Eq. 3.19. In this limit the caloron becomes static. If all distances between the constituents ρ_m are small in units of β the action density is time-dependent. By setting $\vec{y}_{m+1} = \vec{y}_m$ one can obtain the limit (at least for the action density) of a $SU(2)$ caloron. In Eq. 3.21 one obtains $\mathcal{A}_{m+1}[\nu_{m+1}] \mathcal{A}_m[\nu_m] = \mathcal{A}_{m+1}[\nu_m + \nu_{m+1}]$, which describes only a single constituent with the combined mass $8\pi^2(\nu_m + \nu_{m+1})$. For the scalar density of the fermionic zero-modes one also has a compact expression for all $SU(N)$ calorons. This formula reads

$$\psi_z^\dagger(x) \psi_z(x) = -\frac{1}{4\pi^2} \partial^2 \hat{f}_x(z, z), \quad (3.22)$$

where $\hat{f}(z, z')$ is the Green's function, that plays a role in the construction of calorons, and z the fermionic boundary condition $\psi_z(x + \beta \hat{1}) = e^{-2\pi i z} \psi_z(x)$. An exact expression for the Green's functions for an arbitrary $SU(N)$ caloron with $|Q| = 1$ can be given in a short form [53]. For $z = z'$ and if \vec{x} is close to \vec{y}_m and away from all other constituents, \hat{f} simplifies for $z \in [\mu_m, \mu_{m+1}]$ to

$$\hat{f}_x(z, z) = \frac{2\pi \sinh(2\pi r_m(z - \mu_m)) \sinh(2\pi r_m(\mu_{m+1} - z))}{r_m \sinh(2\pi \nu_m r_m)}. \quad (3.23)$$

The zero-mode is maximally localised for $z = (\mu_m + \mu_{m+1})/2$ on the m^{th} constituent and is static, provided the constituents are separated. For further reading about calorons consider the mathematical literature [20, 21, 44, 54–56].

3.4 Instanton model

In this section the current state and the history of the instanton model, especially for finite temperature, is reviewed. Shortly after the discovery of the BPST instanton 't Hooft performed the single loop calculation [46] of the single instanton amplitude. Starting from a $SU(2)$ gauge field theory with spinors and scalars, incorporated in the Lagrangian

$$\mathcal{L} = -\frac{1}{4}F_{\mu\nu}^a F_{\mu\nu}^a - D_\mu\phi^* D_\mu\phi - \bar{\psi}\not{D}\psi, \quad (3.24)$$

he calculated the vacuum-to-vacuum amplitude in the background of an instanton. With a classical solution A_μ^{cl} at hand the steps to be taken are analogous to the quantum mechanical calculation. The gauge field in Eq. 3.24 is replaced by $A_\mu \rightarrow A_\mu^{cl} + \delta A_\mu$. The integrations over fluctuations, which correspond to infinitesimal parameter changes of the instanton, are replaced by collective coordinates and the action, here restricted to the Yang-Mills part Eq. 3.2. The action is expanded up to second order

$$S[A_\mu^{cl} + \delta A_\mu] = \frac{8\pi^2}{g^2} + \frac{1}{2} \int d^4x d^4y \delta A_\mu(x) M_{\mu\nu}(x-y) \delta A_\nu(y) + \mathcal{O}(\delta A^3).$$

Again the first derivative term has dropped out because A_μ^{cl} is a solution of the equations of motion. One normalises the transition amplitude to the free one, regularises the divergent part of the quadratic fluctuation calculation² and separately treats the zero-modes. Due to the gauge freedom one has to account also for zero-modes which correspond to gauge transformations. The result for the instanton amplitude, expressed as an integral over collective coordinates, is

$$\mathcal{Z}_I = \int d^4y d\rho d\Omega(N_c) d(\rho) \quad \text{with} \quad d(\rho) \propto \frac{1}{\rho^5} (\Lambda\rho)^{\frac{11}{3}N_c - \frac{2}{3}N_f}. \quad (3.25)$$

Integrating over the instanton positions gives a volume factor, which was also encountered in the integration over kink positions, and the contribution from instanton orientations remains finite, since the gauge group is compact $\int d\Omega = 1$. The integral over the instanton sizes suppresses small instantons and unfortunately strongly diverges for large values of ρ . To have a meaningful result one must find a way to cut the instanton size distribution $d(\rho)$. This is qualitatively new in comparison with the quantum mechanical kink-gas, where the kinks had an intrinsic scale and the interaction could be neglected for a dilute gas of pseudo-particles. But in QCD there is no coupling that by itself determines the diluteness of instantons. Anyway, a

²in this way a cut-off Λ and a scale enters the calculation

single instanton is not relevant for the infinite volume. An ensemble of instanton and anti-instantons is more likely to represent the QCD vacuum. This might also provide a mechanism to solve the problem of the ρ integration, although a superposition of instantons and anti-instantons is no strict solution of the equation of motion. The idea of that vacuum structure was developed by Callan et.al. [7], who introduced a sharp infrared cut-off ρ_c to render the ρ integration finite. This cut-off only had to be sufficiently small in order to justify a dilute gas approximation by a small packing fraction. There has been criticism that such a cut-off violates symmetries of the Yang-Mills theory and certain low energy theorems and it appears arbitrary. The ambiguity in choosing some cut-off was overcome by the development of a self-consistent way to deal with an interaction $S_{\text{int}} = S(A_\mu^{\text{IA}}) - 2S_0$ between instantons and anti-instantons [8–10] to regularise the integration. This method seems to be more natural. The action of an overlapping instanton-antiinstanton pair will deviate from $2S_0$ since their superposition is no solution of the equation of motion then.

The approach of [8, 9] was to consider the statistical mechanics of an instanton-antiinstanton gas, whose interactions are of a hard core type for small distances and of dipole type, actually proposed by [7], for large distances. The hard core interaction makes the ρ distribution finite ranged such that the partition sum is reasonably defined. In [10] the partition sum has been estimated using an trial function $n(\rho)$ to replace the $d(\rho)$ distribution. From a variational principle $\delta \ln \mathcal{Z} / \delta n = 0$ they obtained the form

$$n(\rho) = d(\rho) \exp[-\text{const } \bar{n} \bar{\rho}^2 \rho^2], \quad (3.26)$$

depending on the actual size, the average size squared and average density. The prefactor $d(\rho)$ from 't Hooft's result is an upper bound for the instanton density. The interaction is repulsive in the average. Therefore, in the mean field approximation, it stabilises the ρ distribution. These models finally served to encourage the development of the random instanton liquid model for $T = 0$, which is characterised by a sharp ρ distribution around $\bar{\rho} \approx 0.3 - 0.4 \text{ fm}$ and an instanton density $\bar{n} \approx 1 \text{ fm}^{-4}$. These parameters enter the instanton gas model

$$n(\rho) = \bar{n} \delta(\rho - \bar{\rho}). \quad (3.27)$$

further developed by Shuryak [6]. There were many attempts to prove the instanton liquid model on the lattice, i.e. to obtain phenomenological parameters $\bar{\rho}$ and \bar{n} , compatible with the phenomenological expectation. Contrary to the topological susceptibility $\chi_t := \langle Q^2 \rangle / V$, which was confirmed very robustly, size and density and the very instanton nature of topological lumps remained strongly subjective [57, 58]. Introducing fermionic degrees of freedom to the theory results in an attractive instanton-antiinstanton interaction by quark exchange, an effect that is also seen in QCD lattice simulations [59].

However, this work deals with the structure of the vacuum at finite temperature $T := \beta^{-1}$. Since finite temperature sets a scale, the temperature itself, this might provide a natural cut-off for the maximal size of calorons. At a classical level the action of a caloron does not depend on the temperature and this effect can only enter by computation the quantum corrections. Indeed, Gross et.al. [19] performed

this calculations analogously to [46] and showed that the size distribution

$$n(\rho, T) = n(\rho, T = 0) \exp \left[-\frac{1}{3}(2N_c + N_f)(\pi\rho T)^2 - B(\pi\rho\lambda) \right] \quad (3.28)$$

is exponentially suppressed for large calorons $\rho \gg T^{-1}$. The authors already realised the possibility of fields, which possess a non-trivial holonomy or have a non-integer topological charge. However, expanding these fields in powers of A_0 shows that they are suppressed by $e^{-S_{\text{eff}}}$ with a 1-loop effective action of the form [19, 60, 61]

$$S_{\text{eff}} = \int d^4x \left[P(A_0) + E^2 f_E(A_0) + B^2 f_B(A_0) + \text{higher derivatives} \right]$$

where away from the lumps of action the quantity

$$P = \frac{v^2 \bar{v}^2}{3T(2\pi)^2} \Big|_{\text{mod } 2\pi T} \quad \text{with} \quad \cos\left(\frac{v}{2T}\right) := P_\infty(A_0) \quad (3.29)$$

alone determines the probability. In Eq. 3.29 $\bar{v} = 2\pi T - v$ is used in order to get it in the more convenient form [22]. The zeros of the perturbative potential energy $P(A_0)$ correspond to trivial asymptotic holonomy $P_\infty = \pm 1$. Fields with non-trivial holonomy have an additional energy proportional to the 3d volume V and are strongly suppressed. Hence only fields with trivial holonomy contribute.

This was the reason to restrict the calculation in [19] to calorons with trivial asymptotic holonomy. For this case the result Eq. 3.28 can be trusted for $T > T_{\text{crit}}$ as long as the caloron gas is dilute. One could use this to fit the T dependence of the topological susceptibility χ_t . From lattice simulations with finite temperature it is known [62] that $\chi_t(T)$ drops, continuously and fast, to zero above the critical temperature and that it is constant in the confined phase $T < T_{\text{crit}}$. Therefore Eq. 3.28 cannot be right in the confined phase.

However, approaching and crossing the critical temperature from above, the finite temperature gluodynamics rearranges to the disordered phase. So one can suspect that calorons with non-trivial holonomy, the KvBLL calorons, become the relevant degrees of freedom to describe the vacuum structure and, in a self-consistent manner, create a minimum of S_{eff} at $P_\infty = 0$. The argument, that non-trivial holonomy can become important for certain temperatures and the suppression Eq. 3.29 might be overruled by an ensemble of calorons with non-trivial holonomy, was first raised by Diakonov in [63]. Only very recently the vacuum-to-vacuum amplitude has been calculated by Diakonov et.al. [22]. The authors give an expression for the amplitude in the case of large constituent separations, $d \gg T^{-1}$. Written in terms of the 6 location and the holonomy parameters, specified for the $SU(2)$ KvBLL caloron (dyon-dyon) gauge field, the amplitude has the form

$$\begin{aligned} \mathcal{Z}_{DD} = & \int d^3y_1 d^3y_2 T^6 C \left(\frac{8\pi^2}{g^2} \right)^4 \left(\frac{\Lambda e^{\gamma_5}}{4\pi T} \right)^{22/3} (Td)^{-5/3} \left(2\pi + \frac{v\bar{v}}{T}d \right) \\ & \times (vd + 1)^{\frac{4v}{3\pi T} - 1} (\bar{v}d + 1)^{\frac{4\bar{v}}{3\pi T} - 1} \exp[-V P(v) - 2d\pi P''(v)] \end{aligned} \quad (3.30)$$

This formula permits to interpret the sign of P'' as the sign of the linear rising part of the potential between dyons. If the holonomy is not far from being trivial, $0.788 < |P_\infty| \leq 1$, ensuring that $P''(v) > 0$, the dyons attract each other, the non-dissociated caloron is stable and the converging integral defines the fugacity of a complete caloron. However, for $|P_\infty| < 0.788$ the sign of $P''(v)$ changes, the interaction between dyons becomes repulsive and the integration over dyon distances in Eq. 3.30 diverges. At this point the integration has to be replaced by some statistical mechanics of an interacting dyon-antidyon gas or liquid. This was concluded in [23] together with the important observation that below $T_{\text{crit}} = 1.125\Lambda$ trivial holonomy becomes unstable, as shown in Fig. 3.4. This is an attractive scenario for the deconfinement-confinement phase transition.

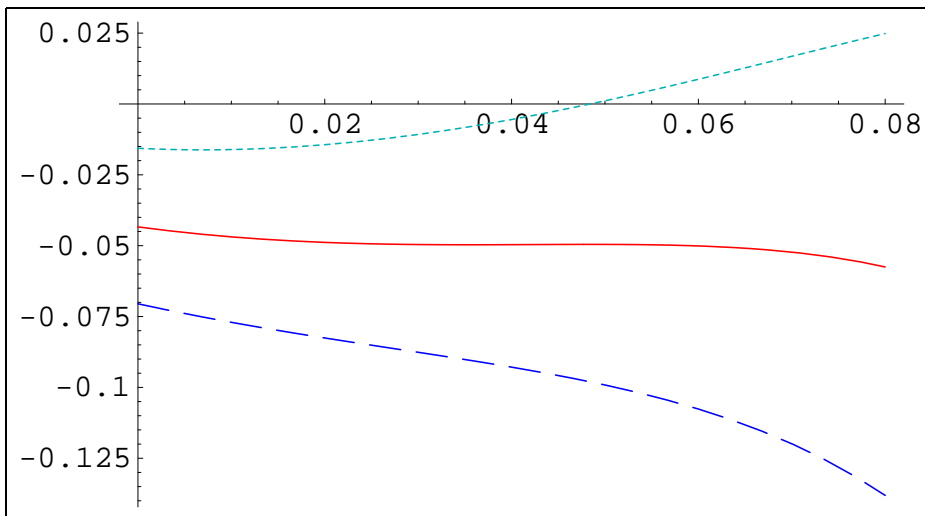


Figure 3.4: free energy of non-interacting caloron gas in units of T^3V for $T = 1.3\Lambda$ (dotted), $T = 1.125\Lambda$ (solid) and $T = 1.05\Lambda$ (dashed) as a function of v in units of $2\pi T$ (figure taken from [23])

The behaviour of $SU(3)$ calorons with non-trivial holonomy is qualitatively different from $SU(2)$. For example the Polyakov loop of the $SU(3)$ theory takes values in the complex plane and consists of up to three monopoles. From this point of view it is interesting to study classical fields on their own. In this sense this work might, on the one hand, help to understand the moduli space of KvBLL calorons, on the other hand, it might be technically interesting to develop lattice techniques to study the caloron content which can be applied to cooled, smeared or even Monte-Carlo fields itself. For this purpose the next chapter shortly describes the lattice method to obtain the classical fields from a Monte-Carlo ensemble. Furthermore the observables, that were said to characterise the caloron and described in the beginning of this chapter, are defined for the finite lattice.

Chapter 4

QCD on the lattice

4.1 Functional integral for lattice QCD

The numerical analysis of classical gauge fields is performed in the lattice gauge theory approach. Lattice gauge theory is a manifestly gauge invariant approach, which is suitable for studying non-perturbative QCD. Here the fundamental gauge fields are $SU(N)$ matrices¹, which are defined on bonds between neighbours of a four-dimensional cubic lattice. The gauge connection (parallel transporter) between a point x and $x + \hat{\mu}$ is denoted by $U_{x,\mu}$ and is called link variable. It is related to the continuum gauge field $A_\mu(x)$ by

$$U_{x,\mu} := \text{P.O.} \exp \left[\int_0^a dz A_\mu(x + \hat{\mu}z) \right] \quad (4.1)$$

where the symbol P.O. denotes the path ordering. The backward transporter is just identified with $U_{x,-\nu} = U_{x-\hat{\nu},\nu}^\dagger$ and the lattice the gauge fields generally obey the periodic boundary conditions in all directions $U_{x+aN_\nu\hat{\nu},\mu} \equiv U_{x,\mu}$. Under a general gauge transformation $\Omega(x) \in SU(N)$ the gauge connection Eq. 4.1 transforms as

$$U_{x,\mu} \xrightarrow{\Omega} U'_{x,\mu} = \Omega^\dagger(x) U_{x,\mu} \Omega(x + \hat{\mu}).$$

The simplest non-trivial gauge invariant quantity, which can be constructed on such a lattice is the plaquette. It is calculated by

$$U_\square = U_{x,\nu} U_{x+\nu,\mu} U_{x+\mu,\nu}^\dagger U_{x,\mu}^\dagger.$$

The simplest action of the gauge field encoded in the links Eq. 4.1 was proposed by Wilson [64] for the pure gauge sector and is also known as the (standard) Wilson plaquette action

$$S_g[U] = \beta \sum_\square \frac{1}{N} \text{Re} \text{tr} (\mathbb{1} - U_\square) \quad \text{for } SU(N). \quad (4.2)$$

With the identification $\beta = 2N/g^2$ one can recover (in the continuum limit $a \rightarrow 0$) the continuum action

¹ $SU(N)$ is the matrix group, such that $U \in GL(N, \mathbb{C})$ fulfils $UU^\dagger = \mathbb{1}$ and $\det U = 1$

$$S_{YM}[A_\mu] = -\frac{2}{g^2} \int d^4x \operatorname{tr} (F_{\mu\nu}(x)F_{\mu\nu}(x)) = S_g[U] + \mathcal{O}(a^5).$$

In order to quantise this gauge theory, a functional integral (path integral) for these fields has to be defined. The formal expression for the partition function of the system is

$$\mathcal{Z} = \int \mathcal{D}A_\mu \exp[-S[A_\mu]]$$

which is an analogue to the statistical weight in a thermodynamical model. The expectation value of some observable M , which is a functional of A_μ , is then

$$\langle M \rangle = \frac{1}{\mathcal{Z}} \int \mathcal{D}A_\mu M[A_\mu] \exp[-S[A_\mu]].$$

This expression is a highly dimensional integral over compact $SU(N)$ groups in the case of the lattice gauge theory. Corresponding expectation values for a function $M(U_{x,\mu})$ of the lattice gauge fields read

$$\langle M \rangle = \frac{1}{\mathcal{Z}} \int \prod_{x,\mu} dU_{x,\mu} M(U_{x,\mu}) \exp[-S_g[U]] \quad \text{with} \quad \mathcal{Z} = \int \prod_{x,\mu} dU_{x,\mu} \exp[-S_g[U]].$$

The unique integration measure dU for an integration in $SU(N)$ group space is the Haar measure. For a Monte-Carlo study with importance sampling, the gauge fields have to be generated according to the Haar measure dU and the weight factor $e^{-S[U]}$ that

$$P[U] = \mathcal{Z}^{-1} \exp[-S_g[U]] dU.$$

For $SU(N)$ this can be effectively implemented using a pseudoheatbath algorithm [65, 66], that works in subgroups [67] of $SU(N)$. Since this study is restricted to $N = 3$ three $SU(2)$ subgroups were used for simulation. The main part of this investigation of $SU(3)$ lattice gauge theory was done for $\beta = 5.65$, which corresponds to confined phase, on a 4×12^3 lattice. For this setting one can measure e.g. the plaquette expectation value $\langle \operatorname{Re} \operatorname{tr} ((1 - U_\square)/3) \rangle = 0.537783(8)$.

4.2 QCD at finite temperature

The classical theory has no intrinsic scale parameter. Therefore one has no idea of a lattice spacing a in the classical Yang-Mills theory. Therefore, in the classical theory the notion finite temperature refers to $S^1 \times \mathbb{R}^3$ as the domain of definition for the periodic gauge fields. On the lattice this can be realised by choosing some asymmetric $N_t \times N_s^3$ lattice, with $N_s \gg N_t$. In quantised finite temperature lattice gauge theory finite temperature is attained by sending $L = N_s a$ to infinity while the temperature $T = (N_t a)^{-1}$ remains fixed at some finite value. The lattice spacing $a(\beta)$ depends on the bare coupling β and has to be phenomenologically determined from some correlation function. Pure $SU(3)$ Yang-Mills theory with finite temperature

has an exact global $Z(3)$ symmetry. The notion $Z(3)$ refers to the centre of the group $SU(3)$, which is the largest subgroup that commutes with all elements of $SU(3)$. This group only consists of only three elements, which can be written as

$$SU(3) \supset Z(3) \ni z = \exp \left[2\pi i \frac{m}{3} \right] \mathbb{1} \quad m = \{0, 1, 2\}. \quad (4.3)$$

On the lattice this symmetry can be seen as follows. Multiplying all links in t direction in a $t = \text{const.}$ plane with a center element z leaves the action invariant since the plaquette variables are not changed

$$U'_\square = (zU_1)U_2(zU_3)^\dagger U_4^\dagger = |z|^2 U_1 U_2 U_3^\dagger U_4^\dagger = U_\square.$$

Each closed loop crosses a $t = \text{const.}$ plane either twice or not at all! The same holds for any other observable built from closed loops. However if an observable is made gauge invariant only due to the temporal periodic boundary conditions, it will pick up a phase factor z only once since it crosses this t plane only once. This applies for the Polyakov loop, which is the order parameter of this symmetry. On the lattice with N_t gauge links in the temporal direction the Polyakov loop is defined

$$\mathcal{P}(\vec{x}) := \prod_{n=0}^{N_t-1} U_{x+n\hat{t},t} \quad P(\vec{x}) := \frac{1}{3} \text{tr } \mathcal{P}(\vec{x}). \quad (4.4)$$

Under a gauge transformation $\mathcal{P}(\vec{x})$ transforms as $\Omega^\dagger(0, \vec{x}) \mathcal{P}(\vec{x}) \Omega(N_t, \vec{x})$ which, for periodic gauge transformations, conserves the trace of $\mathcal{P}(\vec{x})$. For the $Z(3)$ symmetry transformation, described above, the Polyakov loop becomes $z \cdot \mathcal{P}(\vec{x})$. For the statistical (quantised) system this symmetry implies $\langle P \rangle \equiv 0$ for all β if there are no external sources present. However, this symmetry is spontaneously broken in the deconfined phase for $\beta > \beta_{\text{crit}}$. A good indicator for this first order phase transition (for $SU(3)$) is the spatially averaged modulus of the Polyakov loop

$$\langle |P| \rangle := \left\langle V^{-1} \left| \sum_{\vec{x}} P(\vec{x}) \right| \right\rangle. \quad (4.5)$$

The β dependence of $\langle |P| \rangle$ for several lattices is shown in Fig. 4.1. In the case of $N_t = 4, 6$ the critical values $\beta_{\text{crit}} = 5.6925(2), 5.8941(5)$ [68] for the Wilson plaquette action (dashed line) agree qualitatively with our measurements. For $\beta < \beta_{\text{crit}}$ the symmetry $\langle |P| \rangle = 0$ is restored up to finite size effects and above the critical coupling the $\langle |P| \rangle$ has a non-vanishing expectation value. Our motivation to work just below the deconfinement transition is to ensure, that non-trivial holonomy dominates the classical fields.

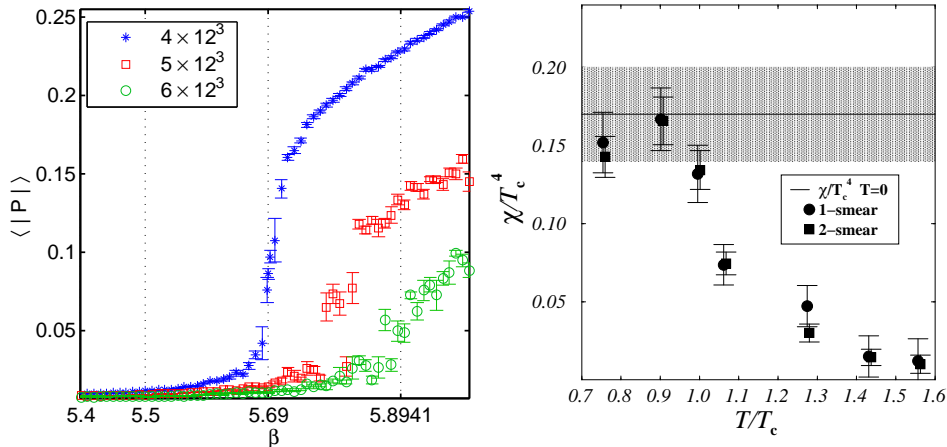


Figure 4.1: β dependence of $\langle |P| \rangle$ for $(4, 5, 6) \times 12^3$ lattices (left) and topological susceptibility for finite temperature pure $SU(3)$ theory, taken from Di Giacomo et.al [62] (right)

The topological susceptibility falls rapidly to zero above the critical temperature. Hence topological non-trivial fields are suppressed for $T \gg T_{crit}$. This effect is seen in the topological charge distribution Fig. 4.2 after 50 cooling steps. The fields shown there were generated in the confined $\beta = 5.6$ and deconfined $\beta = 5.8$ phase. Therefore a large scale statistics of cooled fields with non-trivial holonomy and from various topological sectors should start in the confined phase.

One can use the two-loop formula for asymptotic scaling as a crude approximation to determine the temperature scale T/T_{crit} . The scaling of $a(\beta) \Lambda = R(\beta)$ for sufficient large β is given by

$$R(\beta) = \left(\frac{\beta}{2N b_0} \right)^{b_1/(2b_0^2)} \exp \left[-\frac{\beta}{4N b_0} \right]$$

with the renormalisation coefficients $b_0 = \frac{11N}{48\pi^2}$ and $b_1 = \frac{34}{3} \left(\frac{N}{16\pi^2} \right)^2$. Deviations from scaling can be included by an additional function $\lambda(\beta)$ with $\lambda(\beta) := a\Lambda/R(\beta)$ [68]. With the data from [68], extrapolated back to $\beta = 5.65$, one obtains $T/T_{crit} \approx 0.91$ ($N_t = 4$) and $T/T_{crit} \approx 0.6$ ($N_t = 6$).

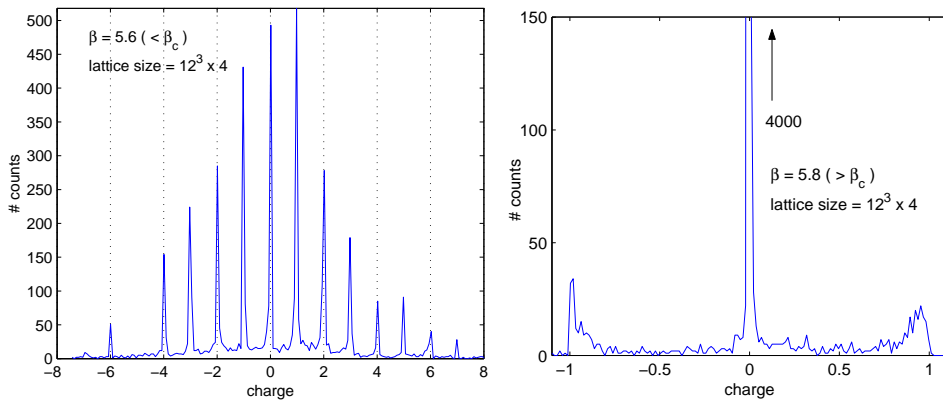


Figure 4.2: topological charge distribution for $\beta = 5.6$ and $\beta = 5.8$ for 4×12^3 lattice after 50 cooling steps

4.3 Improved actions

To consider the impact of improved actions different definitions or gauge actions can be used. We consider improved gauge actions with higher loop (irrelevant) operators where the couplings c_i can depend on the gauge coupling g or some external parameter ϵ . Until now only the plaquette U_\square was introduced. The loops encountered in the improved actions, to be introduced, are

$$\begin{aligned}
 R_\square &= \begin{array}{c} \overrightarrow{\hspace{1.5cm}} \\ \left[\begin{array}{c} \overrightarrow{\hspace{1.5cm}} \\ \overleftarrow{\hspace{1.5cm}} \\ \overrightarrow{\hspace{1.5cm}} \\ \overleftarrow{\hspace{1.5cm}} \end{array} \right] \\ \overleftarrow{\hspace{1.5cm}} \end{array} & \text{rectangle,} \\
 C_\square &= \begin{array}{c} \overrightarrow{\hspace{1.5cm}} \\ \left[\begin{array}{c} \overrightarrow{\hspace{1.5cm}} \\ \overrightarrow{\hspace{0.5cm}} \\ \overleftarrow{\hspace{0.5cm}} \\ \overleftarrow{\hspace{0.5cm}} \\ \overrightarrow{\hspace{0.5cm}} \\ \overrightarrow{\hspace{0.5cm}} \end{array} \right] \\ \overleftarrow{\hspace{1.5cm}} \end{array} & \text{parallelogram and} \\
 S_\square &= \begin{array}{c} \overrightarrow{\hspace{2cm}} \\ \left[\begin{array}{c} \overrightarrow{\hspace{2cm}} \\ \overleftarrow{\hspace{2cm}} \\ \overrightarrow{\hspace{2cm}} \\ \overleftarrow{\hspace{2cm}} \end{array} \right] \\ \overleftarrow{\hspace{2cm}} \end{array} & 2a \times 2a \text{ square.}
 \end{aligned}$$

An ansatz for an improved action S_{imp} with higher loop operators can be written in the following form

$$\begin{aligned}
 S_{\text{imp}}[U] = -\beta & \left[\sum_{\mu > \nu} c_1 \frac{1}{3} \text{Re tr} (\mathbb{1} - U_\square) + c_2 \frac{1}{3} \text{Re tr} (\mathbb{1} - R_\square) \right. \\
 & \left. + c_4(\epsilon) \frac{1}{3} \text{Re tr} (\mathbb{1} - S_\square) + \sum_{\mu > \nu > \sigma} c_3(g) \frac{1}{3} \text{Re tr} (\mathbb{1} - C_\square) \right]. \quad (4.6)
 \end{aligned}$$

One possible choice for a RG improved action is the tadpole improved Luescher-Weisz action [69]. There the couplings depend on $\langle \frac{1}{3} \text{Re tr} (U_\square) \rangle = u_0^4(g)$ and additionally on $\alpha = -(\ln u_0^4)/3.06839$ in the following form

$$c_1 = 1, \quad c_2(g) = -\frac{1}{20u_0^2} (1 + 0.4805 \alpha), \quad c_3(g) = -\frac{1}{u_0^2} 0.03325 \alpha \quad \text{and} \quad c_4 = 0.$$

This definition of an action is very costly and is not adjusted to improve the classical properties of instantons. For this purpose first explorations with Luescher-Weisz action were abandoned and the so-called square action, where the couplings depend on an adjustable parameter ϵ , was only used to cool equilibrium gauge fields

$$c_1(\epsilon) = \frac{4 - \epsilon}{3}, \quad c_2 = c_3 = 0, \quad c_4(\epsilon) = \frac{\epsilon - 1}{48}. \quad (4.7)$$

Using $\epsilon = 1$ the standard Wilson plaquette action is obtained. With $\epsilon = 0$ the $\mathcal{O}(a^2)$ tree level improved square action is obtained. For $\epsilon = -1$ the action is the so-called over-improved action and prevents instantons from shrinking of instantons due to lattice discretisation artifacts [27]. First explorations started with Luescher-Weisz action. Only the over-improved gauge action was helpful to circumvent the shrinking of instantons due to artifacts of the gauge action. However, mainly the Wilson gauge action was used in this work.

4.4 Cooling methods

The equation of motion, that corresponds to one of these lattice actions, has to be solved to obtain a classical gauge field. Since the equation of motion can be written using an variational principle $\delta S[U] = 0$ it is equivalent to look for local minima of $S[U]$. Throughout this work cooling with various definitions of actions was used. For all cooling methods one uses the decomposition of the action

$$S[U] = -\text{Re tr} (U_{x,\mu} M^\dagger) + \text{rest}, \quad (4.8)$$

where the matrix M in Eq. 4.8 is called the staple of (x, μ) and 'rest' is the part of the action which does not depend on the link $U_{x,\mu}$ in question. The staples for the Wilson action can be written as $M = \sum_{\nu \neq \mu} U_{x,\nu} U_{x+\nu,\mu} U_{x+\mu,\nu}^\dagger$ as shown in Fig. 4.3.

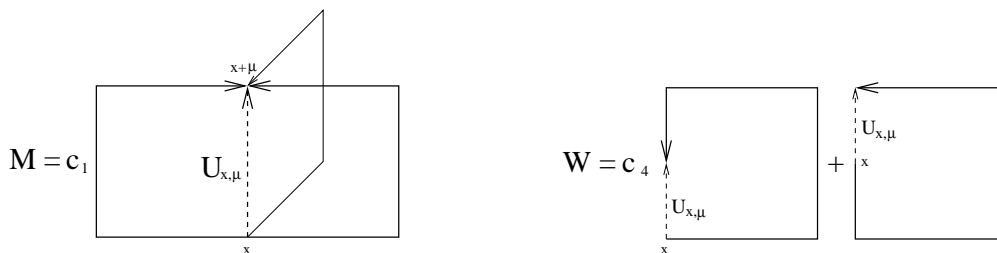


Figure 4.3: staples for Wilson plaquette action ($\epsilon = 1$) (left) and additional staples for square action ($\epsilon = -1$) (right)

An artificial dynamics is then introduced by replacing the old link $U_{x,\mu}$ by some other $SU(3)$ matrix U' , for which $S[U'] < S[U]$. To have some definite scheme one would use the maximal choice, that is the projection described in Appendix A. Hence cooling with respect to Wilson plaquette action or over-improved square action is achieved by replacing the link variable

$$U_{x,\mu} \rightarrow \mathbf{P}_{SU(3)}(M) \quad \text{or} \quad \mathbf{P}_{SU(3)}(M + W)$$

where $\mathbf{P}_{SU(3)}$, the ReTrMax projection Eq. A.1, is used and the new link is replaced immediately after the projection. In the heatbath of neighbouring links the replaced link is a solution of the equation of motions. Iterating this over the whole lattice is a so-called cooling step.

Another method to relax the gauge field is the APE-smearing. The original gauge field $W_{x,\mu}^{(0)} := U_{x,\mu}$ is mapped to a gauge field $W_{x,\mu}^{(n)}$ by defining an APE-blocking step

$$W_{x,\mu}^{(n+1)} = \mathbf{P}_{SU(3)} \left((1 - \alpha) W_{x,\mu}^{(n)} + \frac{\alpha}{6} \sum_{\pm\nu \neq \pm\mu} W_{x,\nu}^{(n)} W_{x+\nu,\mu}^{(n)} W_{x+\mu,\nu}^{\dagger(n)} \right).$$

This blocking steps under-relaxes the change, that would be proposed by the cooling step. Usually a small number of APE-blocking steps $n = 10$ is combined with $\alpha = 0.45$ to leave the long range structure of gauge fields intact. Since it under-relaxes this method is not suitable to obtain classical solutions on the lattice but to remove UV fluctuations from the gauge fields. Assuming one can implement the elementary projection step, the cooling method is suited for all gauge actions, which can be linearised in the elementary link variable. Classical solutions can be very conveniently obtained by the cooling method.

4.5 Detecting classical fields on the lattice

After having obtained classical gauge fields the main part of this work was to identify and categorise these field configurations and their topology. In the beginning of the last section the observables, which need to be measured, were introduced but need to be defined on the lattice.

4.5.1 Gluonic observables on the lattice

The standard Wilson gauge action for $SU(3)$ is defined analogous to Eq. 4.2 as $S_g[U] = \sum_{\square} \frac{\beta}{3} \text{Re tr}(\mathbb{1} - U_{\square})$. Averaging all possible loops $U_{x,\mu\nu}$ in a $\mu - \nu$ plane which are attached to a certain point x point is called *clover average* of the loops at x and is used to obtain a smoother definition of the action density². For standard Wilson gauge action this yields a definition for the local action density

$$s_g(x) := \frac{1}{12} \sum_{\substack{\text{clover avg.} \\ \mu < \nu}} \text{Re tr}(\mathbb{1} - U_{x,\mu\nu}). \quad (4.9)$$

Fixing a $\mu - \nu$ plane and calculating the clover averaged loops open at x and projected to the algebra with Eq. 4.11 gives the naive definition of the field strength $F_{\mu\nu}(x)$. Since the topological charge derived from this expression strongly deviates from an integer value, even for classical fields, this definition was not found sufficient to make an analysis for higher charge sectors. For the measurements of topological properties of classical fields with $|Q| > 1$ it was found crucial to use an improved operator for the field strength [41].

$$F_{\mu\nu}(x) := \sum_{\text{clover avg.}} (k_1 C_{\mu\nu}^{(1,1)} + k_2 C_{\mu\nu}^{(2,2)} + k_3 C^{(1,2)} + k_4 C^{(1,3)} + k_5 C_{\mu\nu}^{(3,3)})_{\text{algebra}} \quad (4.10)$$

The matrix $C_{\mu\nu}^{(n,n)}$ is an $n \times n$ gauge invariant Wilson loop starting at the point x . The subscript algebra denotes making the expression traceless and anti-hermitian. This is also the standard procedure if one wants to extract the $A_{\mu}^a(x)$ from the $U_{x,\mu}$ fields.

$$(U)_{\text{algebra}} = \frac{1}{2} \left[(U - U^{\dagger}) - \frac{1}{3} \text{tr}(U - U^{\dagger}) \right] \quad (4.11)$$

With the choice of $k_5 = 1/90$ the the 3-loop $\mathcal{O}(a^4)$ -improved field-strength tensor is obtained

$$\begin{aligned} k_1 &= 19/9 - 55k_5 = 3/2, & k_2 &= 1/36 - 16k_5 = -3/20, \\ k_3 &= 64k_5 - 32/45 = 0, & k_4 &= 1/15 - 6k_5 = 0. \end{aligned} \quad (4.12)$$

This definition is computationally cheaper compared to choices which employ all coefficients and the topological charge, calculated from the improved field strength, deviates $\mathcal{O}(10^{-3})$ from integer values in the case of a smooth gauge field. For equilibrium fields the topological charge is not well-defined. The improved field strength provides an improved definition for the action and the topological charge

²the β dependence of the action is omitted here

$$S[U]/S_0 = -\frac{1}{8\pi^2} \sum_x \sum_{\mu < \nu} \sum_{i,j=1}^3 F_{\mu\nu}^{ij}(x) F_{\mu\nu}^{ji}(x) \quad (4.13)$$

$$Q[U] = -\frac{1}{8\pi^2} \sum_x \sum_{\substack{\mu < \nu \\ \rho < \sigma}} \sum_{i,j=1}^3 \epsilon_{\mu\nu\rho\sigma} F_{\mu\nu}^{ij}(x) F_{\rho\sigma}^{ji}(x) \quad (4.14)$$

The field strength here is Eq. 4.10 with the couplings taken from Eq. 4.12 and the definition of the topological charge according to Eq. 3.4. The field strength $F_{\mu\nu}$ takes its values in the fundamental representation of the $SU(3)$ Lie algebra and is a 3×3 complex matrix with the elements $F_{\mu\nu}^{ij}$.

With the Polyakov loop operator Eq. 4.4 the asymptotic holonomy is defined as follows. First the 4-dimensional action density $s(x)$ is projected down to 3 dimension $s(\vec{x})$ by summing it over the 1st (temporal) direction $s(\vec{x}) := \sum_t s(t, \vec{x})$. Ten percent of all points \vec{x} in the volume with the smallest spatial action $s(\vec{x})$ are defined as the asymptotic region V_∞ . The asymptotic holonomy is then calculated by averaging³

$$P_\infty := \frac{1}{V_\infty} \sum_{\vec{x} \in V_\infty} P(\vec{x}) \quad \text{and} \quad (4.15)$$

$$\mathcal{P}_\infty := \exp(2\pi i \text{diag}(\mu_1^\infty, \mu_2^\infty, \mu_3^\infty)) \quad \text{with} \quad (4.16)$$

$$\mu_m^\infty := \frac{1}{V_\infty} \sum_{\vec{x} \in V_\infty} \mu_m(\vec{x}). \quad (4.17)$$

The angles $\mu_m(\vec{x})$ are just the eigenvalues of the Polyakov loop operator $\mathcal{P}(\vec{x})$, defined in Eq. 4.4. Certainly these eigenvalues are gauge invariant.

4.5.2 Fermionic observables on the lattice

As already mentioned, an important observable is the spectrum of the massless Dirac operator. Here one is especially interested in the lowest eigenvalues and corresponding eigenmodes of the Dirac operator with arbitrary temporal fermionic boundary conditions

$$\psi(x + \beta\hat{1}) = \exp[2\pi i\xi] \psi(x). \quad (4.18)$$

On the lattice the so called *doubling problem* occurs. Eigenmodes on the edge of the Brillouin zone give rise to unphysical zero-momentum modes. Historically the Wilson Dirac operator has been proposed to avoid doubling at the expense of violating chiral symmetry explicitly. A further improvement with respect to $\mathcal{O}(a^2)$ corrections is the clover-improved Wilson-Dirac operator⁴, which is defined

$$\begin{aligned} M(x, y) &= \delta_{x,y} - \kappa \sum_{\mu=1}^4 \left[(\mathbb{1} - \gamma_\mu) U_{x,\hat{\mu}} \delta_{x+\mu,y} + (\mathbb{1} + \gamma_\mu) U_{x-\hat{\mu},x}^\dagger \delta_{x-\mu,y} \right] \\ \not{D}(x, y) &= M(x, y) + \frac{i}{2} \kappa c_{sw} \sigma_{\mu\nu} F_{\mu\nu}(x) \delta_{x,y} \quad \text{with} \quad \sigma_{\mu\nu} = \frac{i}{2} [\gamma_\mu, \gamma_\nu]. \end{aligned} \quad (4.19)$$

³**Note:** This procedure makes only sense if the eigenvalues $\{\mu_n\}$ are sorted.

⁴colour and spinor indices are omitted

For the massless and classical improved Dirac operator one has to chose the parameter $\kappa = 1/8$ (massless) and $c_{sw} = 1$ (tree level improved). In the case of finite temperature it is interesting to study the dependency of the Dirac operator on the temporal boundary condition Eq. 4.18. Chosing some boundary condition for the improved Dirac operator induces a family of operators Eq. 4.20

$$\mathbb{D}^{(\xi)}(x, y) \simeq \mathbb{D}(x, y) + \gamma^0 \frac{2\pi i \xi}{\beta} \delta_{xy}. \quad (4.20)$$

This corresponds to the formula used in the construction of KvBLL calorons and circumvents the boundary conditions by an extra term. Nevertheless, for this work the boundary conditions are explicitly used by applying this phase factor to the neighbour terms in Eq. 4.19. This operator, represented as a general complex $N \times N$ matrix acts on complex vectors ψ by

$$(\mathbb{D}^{(\xi)}\psi)_{r\alpha}(x) = \sum_{y,s,\beta} \mathbb{D}_{r\alpha,s\beta}^{(\xi)}(x, y) \psi_{s\beta}(y) \quad (4.21)$$

where $\psi_{r\alpha}(x)$ is a complex field with four spinor indices α and 3 colour indices r defined on the $N_t N_s^3$ points of the lattice. Hence the Dirac operator is a complex $N \times N$ matrix with $N = 12 N_t N_s^3$. The computation of eigenvectors $\psi^{(\lambda)}$ and eigenvalues and λ for the eigenvalue problem

$$\mathbb{D}^{(\xi)}\psi^{(\lambda)} = \lambda\psi^{(\lambda)} \quad (4.22)$$

is a large scale problem. For example one has $N = 82944$ for a 4×12^3 lattice or $N = 576000$ for a 6×20^3 $N = 576000$ lattice. To solve this problem the ARPACK code package [70], that uses the implicit restarted Arnoldi algorithm, is used to calculate 10-80 eigenvectors $\psi^{(\lambda)}$ and eigenvalues λ of $\mathbb{D}^{(\xi)}$ with the smallest modulus for some fixed values of the boundary condition ξ . From the zero-modes the zero-mode density ρ and the chiral density χ are computed to study localisation of topology. On the lattice both quantities are defined by

$$\rho(x) := \sum_{a,k} \psi_{ak}^{(0)\dagger}(x) \psi_{ak}^{(0)}(x) \quad \chi(x) := \sum_{a,k} (\psi^{(0)\dagger}(x) \gamma_5 \psi^{(0)}(x))_{ak}. \quad (4.23)$$

The localisation of a normalised eigenmode is measured with the *inverse participation ratio IPR* which is defined as

$$IPR := V \sum_x \rho(x)^2 \in [1, V] \quad (4.24)$$

and ranges from 1 to $V = N_t N_s^3$. This quantity was already used to study localisation eigenmodes of the Dirac operator [25]. For a maximally localised mode $\rho(x) = \delta_{x_0,x}$ one has $IPR = V$ while it becomes $IPR = 1$ for a maximally spread (constant) density $\rho(x) = V^{-1}$. As already seen in the quantum mechanical model the eigenmodes, that correspond to a symmetry⁵ of the pseudo-particle, are localised while the continuum eigenmodes have $IPR \approx 1$.

Now all observables, which are needed to investigate the semiclassical structure of cooled gauge fields, is at our disposal and will be used in the next chapters.

⁵The symmetry is not obvious in this case.

Chapter 5

Classical solutions on the lattice - examples

In this chapter the search for $SU(3)$ lattice calorons is presented. Solutions of the lattice equation of motions are obtained by cooling thermalised gauge fields and compared with discretised analytic expressions for the KvBLL gauge field. The observables, mentioned in the previous chapter, are computed for these fields and tested for the typical behaviour of KvBLL calorons. The techniques and observables developed in the present chapter also enter the statistical analysis of the next chapter.

5.1 Systematics of the investigation

To acquire classical solutions of Euclidean $SU(3)$ Yang-Mills theory at finite temperature, which are the subject of this study, lattice gauge fields are cooled with over-improved and Wilson gauge action. The original gauge fields are generated with standard Wilson gauge action at $\beta = 5.65$. This corresponds to confinement close to the deconfinement phase transition $T/T_{\text{crit}} \approx 0.91, 0.6$ for $N_t = 4, 6$. In this state the average Polyakov loop vanishes and remains so for a part of the cooling history. The different lattice sizes 4×12^3 , 6×12^3 , 4×20^3 , 6×20^3 and 12^4 are chosen to study how the yield of classical configurations from cooling depends on the lattice geometry.

Starting from the deconfined phase only fields with trivial asymptotic holonomy are obtained by cooling if a suitable stopping criterion has applied. Our study here is restricted to the confinement phase since the KvBLL solutions have generic non-trivial asymptotic holonomy. To which extent a lattice gauge field can be regarded classical is measured by the *violation of (anti) self-duality* δ_F , defined by

$$\delta_F := \frac{1}{32\pi^2} \sum_x \left| \text{tr}(F_{\mu\nu} F_{\mu\nu}) - \left| \text{tr}(F_{\mu\nu} \tilde{F}_{\mu\nu}) \right| \right|. \quad (5.1)$$

For a self-dual or anti-selfdual gauge field, this quantity vanishes. Since this quantity measures the *local* violation of (anti) self-duality also superpositions of self-dual and anti-selfdual calorons may have small values of δ_F . So this criterion is found to be equivalent to definitions of the violation of equation of motion used in previous

works [29, 71] for $SU(2)$. During the process of cooling δ_F , the action, the topological charge and the *non-staticity*, which is defined as

$$\delta_t := \frac{N_t \sum_x |s(x + \hat{t}) - s(x)|}{4 \sum_x s(x)}, \quad (5.2)$$

are monitored. If the action density $s(x)$ of a given gauge field only weakly depends on t , the non-staticity is close to zero. Assuming that the gauge field has maximally non-trivial holonomy at least two dyons can be distinguished by the two maxima of the action density if the non-staticity is lower than the bifurcation value $\delta_t^* = 0.27$ for $SU(2)$ and $SU(3)$ [72]. Then if the non-staticity of the caloron with maximally non-trivial holonomy is even smaller than $\delta_t^{**} = 0.06$ it is possible to see three separated dyons in the analytical action profile for a $SU(3)$ KvBLL caloron. These branching points were calculated from the analytical formula for the action density of the KvBLL caloron for a symmetric setup of constituents. The prefactor $N_t/4$ in δ_t is chosen conventionally following the previous work for $SU(2)$ which used $N_t = 4$ [29].

Excessive cooling with Wilson action will lead to the trivial vacuum $S \rightarrow 0$ and $Q \rightarrow 0$, apart from a few ultimately stable cases. That is why a stopping condition for the cooling has to be introduced to define, when a gauge field is adequately classical and to stop cooling. From the technical observables non-staticity δ_t and the violation of (anti) self-duality two self-containing stopping conditions (A) and (B) were formulated, with the goal to *explore the moduli space of calorons as far as possible*. These conditions are

- (A) stop the cooling if the violation of (anti) self-duality δ_F passes through a minimum and $\delta_F < 0.1$ or
- (B) stop the cooling if either the violation of (anti) self-duality passes through a minimum or the non-staticity does, depending on what happens first. Additionally $\delta_F < 0.2$ is required.

Both conditions (A) and (B) result in nearly (anti) self-dual gauge fields representing various topological sectors. In particular, in most cases configurations with some integer topological charge Q and action $S \gtrsim S_0|Q|$ are found.

The first stopping condition is the traditional choice. Cool the gauge field until the equation of motion are fulfilled as good as possible and the violation of the equation of motion is sufficiently small. There are some reasons that this stopping condition might be too strict. Like in the kink-gas model superpositions of semi-classical objects (kinks and anti-kink or instanton and anti-instanton) are no strict solution of the equations of motion. Nevertheless they provide a realistic model of the vacuum structure. On the other hand it is impossible to model the moduli space for an infinite volume. The numerical investigation can only be done for a discrete torus, where one can obtain a charge 1 solution only at the expense of violating the (anti) self-duality [55]. Accepting a certain violation of the equation of motion is a compromise between the moduli spaces of the torus and finite temperature $S^1 \times \mathbb{R}^3$. Furthermore lattice artifacts of the action will bias the semiclassical content of fields.

Hence one should not insist in perfect solutions to the equation of motion. Stopping condition (B) tends to stop cooling in an earlier stage of cooling.

To characterise classical fields the observables introduced in Chapter 3 and Chapter 4 are measured. The topological charge Q , the normalised action S/S_0 and the violation of (anti) self-duality characterise to which extent the field is classical and to which topological sector Q it belongs. These quantities are derived from the $\mathcal{O}(a^4)$ improved field strength. A perfect (anti)self-dual solution has $Q \in \mathbb{Z}$, $S = S_0|Q|$ and $\delta_F = 0$. From the previously defined Polyakov loop \mathcal{P} the holonomy \mathcal{P}_∞ , the positions \vec{y}_n and overall number of the constituent monopoles is determined.

The most robust definition of a constituent monopole is given with the help of the Polyakov loop operator $\mathcal{P}(\vec{y}) \simeq \text{diag}(e^{i\phi_1(\vec{y})}, e^{i\phi_2(\vec{y})}, e^{i\phi_3(\vec{y})})$. For sufficiently separated constituents a monopole at \vec{y} exists if two eigenvalues of $\mathcal{P}(\vec{y})$ approach each other. For the caloron solution in the continuum they would coincide. This definition is still applicable to define monopoles if only a single peak is visible in the topological charge or action density. In the numerical work a monopole is found by searching for the local minimum \vec{y} of the function $f(\vec{y})$ defined as follows

$$f(\vec{y}) := \min_{i,j} |e^{i\phi_i(\vec{y})} - e^{i\phi_j(\vec{y})}| \quad (5.3)$$

in 3 dimensional space with the additional constraint

$$\min_{\phi \in [0, 2\pi)} |P(\vec{y}) - (2e^{i\phi} + e^{-2i\phi})/3| < 0.05.$$

This constraint ensures that the eigenvalues are sufficiently degenerated and (approaching some ϕ) which guarantees that $P(\vec{x})$ is sufficiently close to the boundary in Fig. 3.3.

For well separated constituents these positions can be compared with the local maxima of the action density. To avoid spurious positions only maxima, which have $s(x) > 0.1 \max_y s(y)$ are considered. For all examples of this chapter and a subset of the later ensembles the spectrum of the clover improved Dirac operator with adjustable temporal boundary conditions was computed. Depending on the fermionic boundary condition $\xi \in [0, 1]$ the maxima of the zero-mode density and the inverse participation ratio IPR are computed. These maxima can be compared with the positions \vec{y} , computed from $\mathcal{P}(\vec{y})$. To compare with the analytical prediction of the fermionic mode notice that $z = 1 - \xi$. The zero-mode is localised on the m^{th} constituent for $z \in (\mu_m, \mu_{m+1})$ and delocalises for $z \approx \mu_m$. For consistency the index theorem $n_- - n_+ = Q$ is checked for all configurations. It is also instructive to check the predicted interplay Eq. 3.21 between the asymptotic holonomy and the monopole behaviour, known from the analytical solution for separated constituents.

In this chapter examples for topological charge $|Q| = 1, 2$ with either trivial or maximally non-trivial holonomy are chosen as extremal cases of 'old' Harrington-Shepard versus 'new' KvBLL calorons. Especially the property of the zero-mode jumping is described with great care since recent investigations make use of this criterion for thermalised gauge fields [25, 26].

5.2 Constructed calorons with $|Q| = 1$

The presentation of KvBLL calorons is started by showing two lattice gauge fields, which are obtained by putting the analytic solution $A_\mu(x)$ for a $SU(3)$ charge 1 KvBLL caloron on the lattice [73]. For a generic gauge field A_μ link $U_{x,\mu}$ is constructed by a partitioning into N sub-links and approximately calculated by

$$U_{x,\mu} := \mathbf{P}_{SU(3)}(\mathbb{1} + \alpha A_\mu(x')) \cdots \mathbf{P}_{SU(3)}(\mathbb{1} + \alpha A_\mu(x' + (N-1)\alpha\hat{\mu})). \quad (5.4)$$

The abbreviation $\alpha = a/N$, $x' = x + a\hat{\mu}/2$ and the projection to the gauge group $\mathbf{P}_{SU(3)}$ are used for the evaluation of the sub-links. This procedure is performed for all links on a 6×20^3 lattice, where the links conventionally have to obey periodic boundary conditions for all directions. Since this definitely not the case for the analytic formula A_μ , the discretised lattice field has to be adapted to the periodic boundary conditions by making $\mathcal{O}(10)$ cooling steps. The analytical formula simplifies when all monopole constituents are placed in the $x - y$ plane. The parameters which are used for the caloron with trivial and non-trivial holonomy are shown in Tab. 5.1.

	1	2	3	holonomy	trivial	non-trivial
x	6.5	16.5	11.5	μ_1	-0.05	-0.30
y	6.5	6.5	16.5	μ_2	0.01	0.05
z	11.5	11.5	11.5	μ_3	0.04	0.25

Table 5.1: position of constituents (left) and eigenvalues of holonomy \mathcal{P}_∞ (right).

The S^1 coordinate of the caloron field is $t = 1$. For trivial holonomy $\mathcal{P}_\infty \rightarrow \mathbb{1}$ the eigenvalues are chosen not to coincide exactly to avoid numerical instability. Direct fitting of cooled gauge fields by the lattice version of the KvBLL solution is not feasible because (i) the construction of all links starting from the continuum KvBLL gauge field is very time consuming, (ii) the gauge connection is not periodic in spatial direction and (iii) the constituents are placed in the $x - y$ plane. Moreover the gauge would have to be fixed for the cooled caloron. Fitting to the zero-mode density is actually possible, as will be shown in the last part of this chapter.

5.2.1 KvBLL caloron with non-trivial holonomy

The first example is the constructed KvBLL caloron with non-trivial holonomy. This gauge field was designed to have $\text{tr}(\mathcal{P}_\infty) = 0$ and $Q = -1$ and the constituents were organised in the $x - y$ plane with constant z position according to Tab. 5.1. After relaxing the boundary conditions the observables, which were described in the previous chapter, are measured as shown in Tab. 5.2.

KvBLL caloron / non-trivial holonomy	
S/S_0	1.33
Q	-1.00
δ_F	0.3
$\text{index}(\not{D})$	-1
δ_t	1.0×10^{-2}
-0.34	
holonomy $\{\mu_i\}$	0.00
+0.34	
local extrema of $q(x)$ (t, x, y, z)	$r_1 = (1, 07, 07, 12)$ $r_2 = (6, 15, 09, 12)$ $r_3 = (2, 12, 14, 12)$
monopole position (x, y, z)	$\vec{y}_1 = (06, 06, 12)$ $\vec{y}_2 = (17, 07, 12)$ $\vec{y}_3 = (12, 16, 12)$

Table 5.2: gluonic observables of KvBLL caloron (non-trivial)

The positions, holonomy and topological charge fit very well to the setting in Tab. 5.1 but the gauge field is obviously not yet anti-selfdual. The violation of anti-selfduality $\delta_F = 0.3$ is quite large and corresponds to the action value $S/S_0 = 1.33 \approx |Q| + \delta_F$. But note that this solution is constructed for $S^1 \times \mathbb{R}^3$ and not for T^4 and that the strong overlap effect, visible in Fig. 5.1, will have an impact on the classical solutions. Applying further $\mathcal{O}(10^3)$ cooling steps with Wilson action to cure this problem decreases the violation of anti-selfduality. At the same time the monopole constituents approach each other and the caloron becomes non-static. In this case the only observable which exhibits the non-trivial substructure in this state of cooling would be the Polyakov loop.

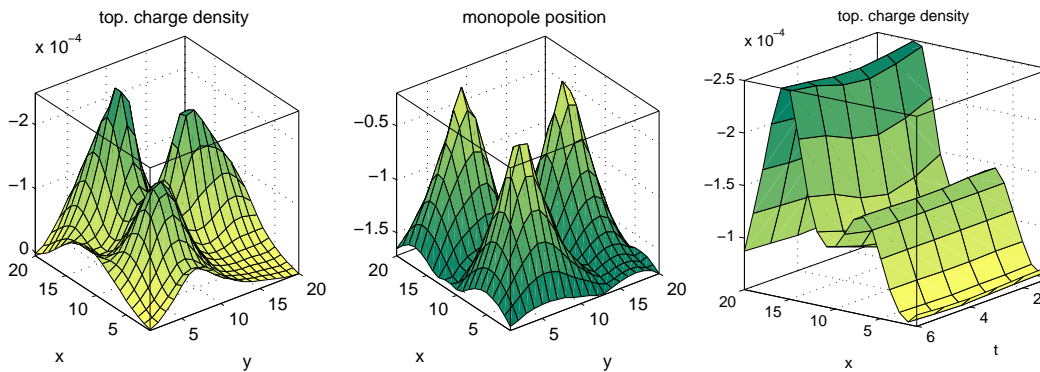


Figure 5.1: topological charge profile (left); monopole position $-f(\vec{y})$ (middle) and topological charge profile in temporal direction (right) are shown

In Fig. 5.1 the topological charge profile of the discretised KvBLL caloron in a fixed plane and the constituent monopole position as a peak in the surface plot of $f(\vec{y})$ are shown. The scalar field $f(\vec{y})$ is projected down to two dimensions by taking the minimal value along the remaining direction which gives to know whether the

eigenvalues coincide at any 2d position coinciding with the self-dual lumps. The topological charge density, allows one to judge how static the caloron actually is.

A further question that arises is whether the asymptotic holonomy \mathcal{P}_∞ is actually well defined. Therefore one needs to check whether the limit $\lim_{|\vec{x}| \rightarrow \infty} \mathcal{P}(\vec{x})$ is justified and the Polyakov loop becomes constant at spatial infinity. Since the Polyakov loop can only become constant up to a gauge transformation it is only meaningful to average over the eigenvalues of the asymptotic Polyakov loop, like it is done in Eq. 4.16. In Fig. 5.2 (lhs.) the eigenvalues of the Polyakov loop $\mathcal{P}(x)$ are plotted versus the spatial action¹ $s(\vec{x}) = \sum_t s(x)$. Typically points with small action have definite eigenvalues and points with larger action have not. Hence the asymptotic holonomy \mathcal{P}_∞ is well defined. This might not be very surprising in the view of the continuum solution but it seems worthwhile check to what extent this is also true on a finite lattice.

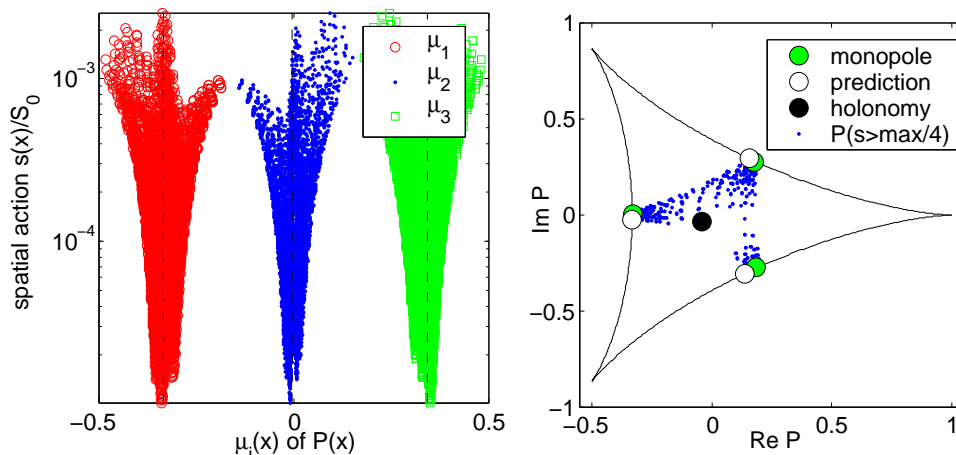


Figure 5.2: scatter plot of Polyakov loop eigenvalues μ_i versus spatial action (left) and scatter plot of Polyakov loop (trace) in the complex plane with predicted values for the monopoles (right)

As already mentioned, there is also a correlation between the Polyakov loop at the positions of the caloron constituents and the asymptotic holonomy known for $SU(3)$. The numerical observation for the analytical solution in case of separated constituents is that the Polyakov loop $\mathcal{P}(\vec{y}_m)$ at the m^{th} constituent is given by Eq. 3.21.

Although it is a numerical observation for the analytical KvBLL gauge fields it is a further evidence that the classical solution on the lattice behaves as it is known for the analytic KvBLL solution. This prediction of $\mathcal{P}(\vec{y}_m)$ can be checked with the finding at the monopole position for the discretised caloron what is actually shown in Tab. 5.3. An explanation for the deviation could be that the constituents were placed between the lattice points Tab. 5.1 to avoid numerical instability during the construction of the links for the lattice KvBLL caloron. In the scatter plot of $\mathcal{P}(\vec{x})$ also the prediction for the values at the position of the monopoles is shown Fig. 5.2 (rhs.). In general the predicted values for P Eq. 3.21 are touched by high action lattice points.

¹The action is summed up over the time direction and assigned to a 3d coordinate.

	prediction	found
\vec{y}_1	$0.15 - 0.30i$	$0.18 - 0.27i$
\vec{y}_2	$0.16 + 0.30i$	$0.18 + 0.28i$
\vec{y}_3	$-0.33 - 0.02i$	$-0.33 + 0.01i$

Table 5.3: prediction and the finding of the Polyakov loop at the monopole position (compare with Fig. 5.2)

The spectrum of the clover-improved Dirac operator is measured with the adjustable temporal fermionic boundary condition $\psi(x + \hat{t}\beta) = e^{2\pi i\xi} \psi(x)$. In Fig. 5.3 the imaginary part of some low lying eigenvalues² and the corresponding inverse participation ratio is shown for several values of the boundary condition ξ . Since the holonomy is maximally non-trivial, $\text{tr}(\mathcal{P}_\infty) = 0$, one would expect the jumping for $\xi = \{0, 1/3, 2/3\}$ what corresponds to the values $\mu_i = \{-1/3, 0, +1/3\}$ in Tab. 5.1 or Tab. 5.2. The zero-mode density is maximally localised in the middle of the intervals for the boundary conditions $\xi = \{1/6, 1/2, 5/6\}$. This behaviour was actually found and is shown³ in the right part of Fig. 5.3.

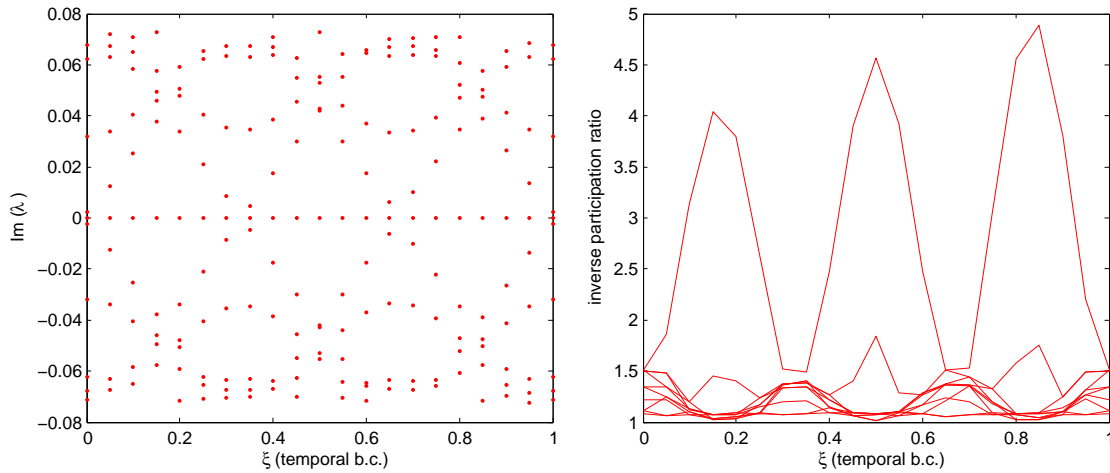


Figure 5.3: fermionic flow depending on (temporal) fermionic boundary condition

The strong dependence of the gap between imaginary value of zero-eigenvalue and the next eigenvalue is very pronounced in Fig. 5.3. In Tab. 5.4 additionally the position of the maximum of the zero-mode density for different values of the boundary condition is shown. Note that this values has no meaning if the mode is delocalised ($IPR \approx 1$).

²ten eigenvalues with the smallest modulus

³Unfortunately this is not shown in a high resolution in ξ since the calculation for 6×20^3 lattice needs many computer resources.

ξ	t	x	y	z	IPR
0.0	1	12	01	20	1.1
0.1	1	07	07	12	3.1
0.2	1	07	07	12	3.8
0.3	1	06	06	12	1.5
0.4	1	12	16	12	2.5
0.5	1	12	16	12	4.6
0.6	1	12	17	12	2.5
0.7	1	17	07	12	1.5
0.8	1	16	08	12	4.6
0.9	1	16	08	12	3.8
1.0	1	12	01	20	1.1

x	y	z	enumeration
6	6	12	1 st
17	7	12	2 nd
12	16	12	3 rd

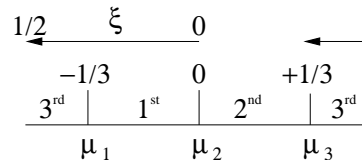


Table 5.4: localisation of zero-mode density ρ (left) and monopole position again (right). the schematic plot visualises that the zero-mode is localised on the 1st constituent for $\xi \in (0, \frac{1}{3})$, on the 3rd for $\xi \in (\frac{1}{3}, \frac{2}{3})$ and on the 2nd for $\xi \in (\frac{2}{3}, 1)$.

After having enumerated the monopole positions following Eq. 3.21, the maximum of the zero-modes density coincides with the monopole position, defined by coinciding eigenvalues of \mathcal{P} , for the designated value of ξ in Tab. 5.4.

The anti-selfdual gauge field obtained by discretising an analytical expression for a KvBLL caloron shows the typical behaviour of the analytically accessible observables. The three constituent positions, which were put into the analytic formula Tab. 5.1, are recovered by the

1. local maxima of the action density and topological charge density Tab. 5.2,
2. three-dimensional points, where two eigenvalues of $\mathcal{P}(\vec{x})$ coincide Tab. 5.2,
3. the points where the fermionic zero-mode density ρ settles for the predicted values of the fermionic boundary condition Tab. 5.4.

The numerical observation for the Polyakov loop at the monopole position is confirmed and determined by the asymptotic holonomy. In the absence of really asymptotic distances the asymptotic holonomy, defined by the average of $\mathcal{P}(\vec{x})$ over points with low action, is well defined. The only deficiency is the large violation of anti-selfduality.

5.2.2 KvBLL caloron with trivial holonomy

The second example is the discretised field of KvBLL caloron with trivial holonomy $\mathcal{P}_\infty \rightarrow \mathbf{1}$. The analytic formula differs in the choice of the asymptotic holonomy in Tab. 5.1 but the position parameters are unchanged. After adapting the periodic boundary conditions to the 6×20^3 gauge field the following observables are measured.

KvBLL caloron / trivial holonomy	
S/S_0	1.33
Q	-1.00
δ_F	0.3
$\text{index}(\not{D})$	-1
δ_t	0.08
	-0.05
holonomy $\{\mu_i\}$	0.00
	0.05
extrema of $q(x)$	$r=(1,12,17,11)$
monopole position	not well defined (see Fig. 5.4 rhs.)

Table 5.5: gluonic observables of KvBLL caloron (trivial)

Since the asymptotic holonomy resides in the center of the gauge group $\mathcal{P}_\infty \in Z(3)$ the three eigenvalues already coincide in the asymptotic region. Therefore it makes no sense to speak of a position of a constituent monopole defined by degenerated eigenvalues in the present case of trivial holonomy. The 3rd constituent has the full mass S_0 and is actually observed. Comparing with the non-trivial caloron this is indeed consistent. In Fig. 5.4 the profile of the topological charge density and the (would-be) localisation of monopoles due to doubly degenerate eigenvalues of the Polyakov loop is shown.

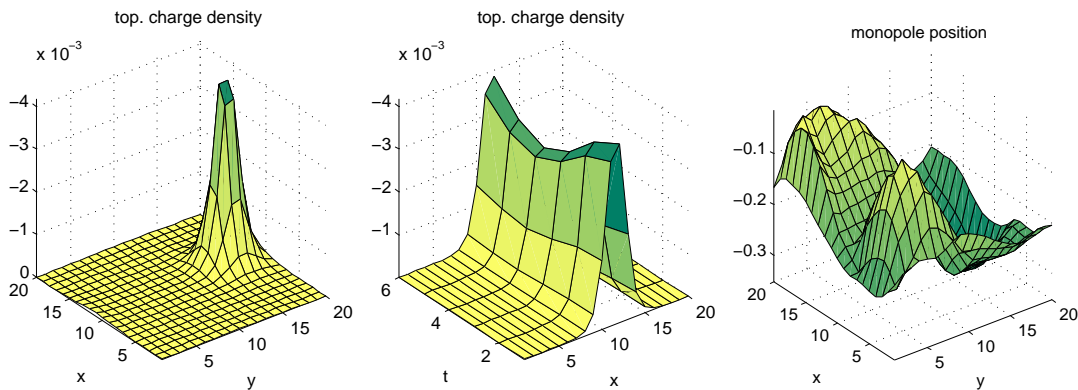


Figure 5.4: topological charge density $q(x)$ of the KvBLL solution with trivial holonomy for different slices (left,middle) and the position of the constituent monopoles (right)

Obviously the positions of the monopoles \vec{y}_1, \vec{y}_2 , defined by the twofold degenerated eigenvalues, are not correlated to a position of some gluonic maximum. With our monopole-finder Eq. 5.3 a lot of spurious constituent monopoles are found. In Fig. 5.5 the eigenvalues are again plotted versus the spatial action. At spatial 'infinity' the eigenvalues of the Polyakov loop become constant and the asymptotic holonomy is again well defined. The scatter plot of the Polyakov loop in Fig. 5.5

shows the signature of a Harrington-Shepard caloron with trivial holonomy like it was shown in the left panel of Fig. 3.3. The Polyakov loop at the position of the maximum of the action density comes close to $\mathcal{P}(\vec{x}) \simeq \text{diag}(-1, -1, +1)$ as it would be expected for such an $SU(2)$ embedded trivial caloron, and the trace comes close to $P(\vec{x}) = -1/3$. The other values are $\mathcal{P}(\vec{y}_{1/2}) = \mathbb{1}$ what actually corresponds to the asymptotic area. The masses for the corresponding constituents vanish and hence they cannot be observed. Analytically it is argued [52] that these monopoles might be recovered in a suitable limit but this seems difficult to be arranged for the lattice.

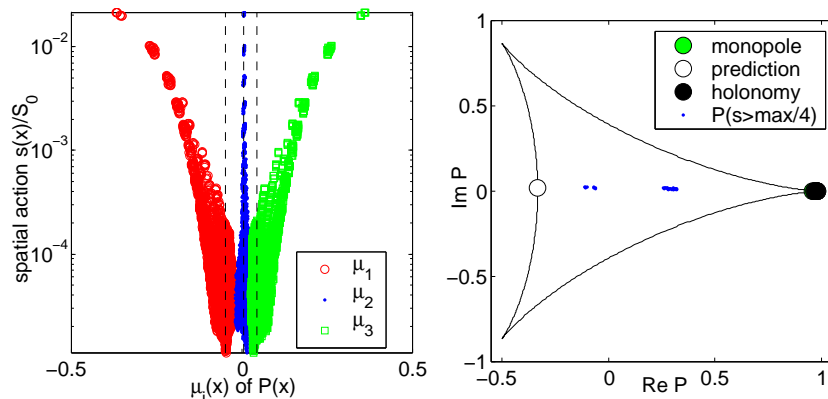


Figure 5.5: Polyakov loop eigenvalues versus the spatial action (left) and the scatter plot of $P(\vec{x})$ for points with large action in the complex plane

The fermionic flow for the trivial caloron is shown in Fig. 5.6. Comparing with Fig. 5.3 it is visible that the zero-mode delocalises maximally for periodic temporal boundary conditions but is maximally localised only for *one* ξ and hence also only on *one* position. This is actually the position of the 3rd constituent with the maximal localisation at $\xi_{max} = (\mu_3 + \mu_4)/2 = 1/2$.

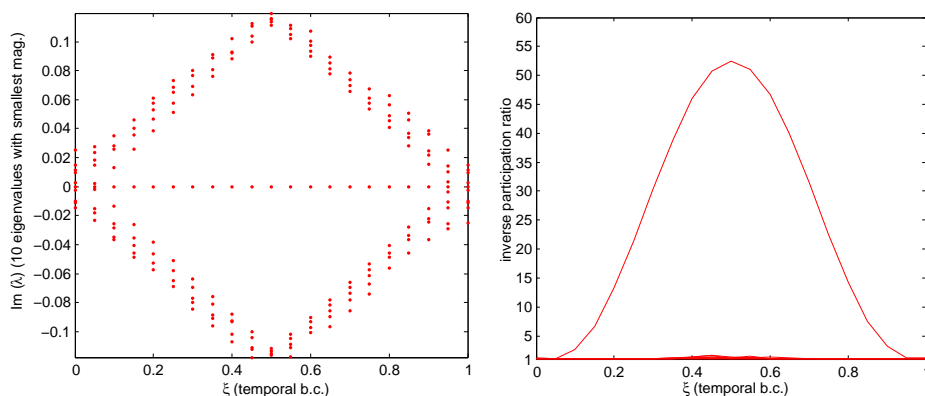


Figure 5.6: fermionic flow depending on (temporal) fermionic boundary condition

For the sake of completeness also the constant positions for different values of the boundary conditions are shown in Tab. 5.6. In fact there is no monopole position available, but the position coincides with the gluonic maximum and the input parameter. Note again that giving a position is meaningless for $IPR \approx 1$. Comparing

with the caloron with non-trivial holonomy also the difference in the maximal value of the inverse participation ratio IPR is noticeable. Partially this is due to the static nature of the non-trivial caloron but looking at the gluonic densities Fig. 5.1 it is obvious that overlapping effects due to the spatial boundary conditions are less important here.

ξ	t	x	y	z	IPR
0.0	1	01	12	11	1.1
0.2	1	12	17	12	13.2
0.4	1	12	16	12	46.0
0.6	1	12	16	12	46.7
0.8	1	12	17	12	14.3
1.0	1	01	12	11	1.1

Table 5.6: localisation of the fermionic density ρ ; no monopole position available

Trivial holonomy is also covered by the KvBLL caloron solution. For $\mathcal{P}_\infty = \mathbb{1}$ one obtains the gauge field for the Harrington-Shepard caloron. In the language of the KvBLL caloron this means that with $\mathcal{P}_\infty \rightarrow \mathbb{1}$ two constituent monopoles are massless $\nu_{1,2} \rightarrow 0$ and cannot be seen in the gluonic or fermionic densities. The Polyakov loop \mathcal{P} is not only degenerate at some spatial points but rather in a large portion of space. In this case an interpretation of constituent monopoles, to be identified on the lattice by isolated minima of the distance between eigenvalues, makes no sense. A proper cut to the holonomy should be imposed to exclude these cases from an investigation which uses the definition of coinciding eigenvalues as a definition of a constituent.

5.3 Cooled calorons with $|Q| = 1$

The following examples for calorons are obtained by cooling from equilibrium configurations, generated at $\beta = 5.65$ with respect to various definitions of the action and stopping criteria on different lattice sizes.

5.3.1 Non-trivial caloron from standard cooling

The *standard* strategy in order to obtain self-dual gauge fields is to use Wilson gauge action to cool an equilibrium gauge field until (A) the violation of (anti) self-duality is minimal. With this approach no static dissociated caloron with dyonic constituents and charge 1 was obtained from $\mathcal{O}(1000)$ cooled gauge fields, even if the holonomy happened to remain maximally non-trivial. This might answer the question, why dissociated charge 1 KvBLL calorons were not seen in earlier cooling studies. The gauge field example to be presented now was cooled on a 4×12^3 lattice and has non-trivial holonomy but is not static. Due to the exit criterion the violation of the lattice equation of motion δ_F is smaller than the values for the discretised calorons discussed before. The action density in Fig. 5.7 clearly shows only one localisation.

Cooled caloron with (A)	
S/S_0	1.03
Q	-1.00
δ_F	0.03
$\text{index}(\not{D})$	-1
δ_t	0.23
<hr/>	
holonomy $\{\mu_i\}$	0.003
	0.379
<hr/>	
extrema of $q(x)$	$r = (3, 06, 09, 06)$
<hr/>	
monopole position	$\vec{y}_1 = (05, 09, 04)$
	$\vec{y}_2 = (06, 10, 08)$
	$\vec{y}_3 = (06, 08, 06)$

Table 5.7: gluonic observables of CFG157

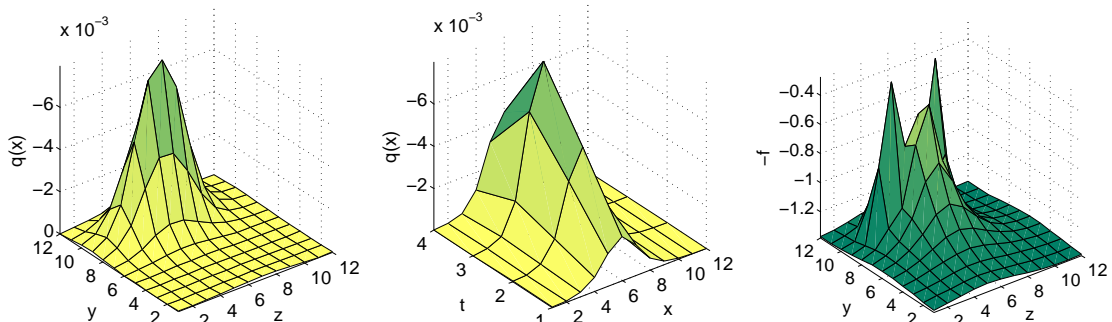


Figure 5.7: topological charge density $q(x)$ (left,middle) and position of the constituent monopole (right).

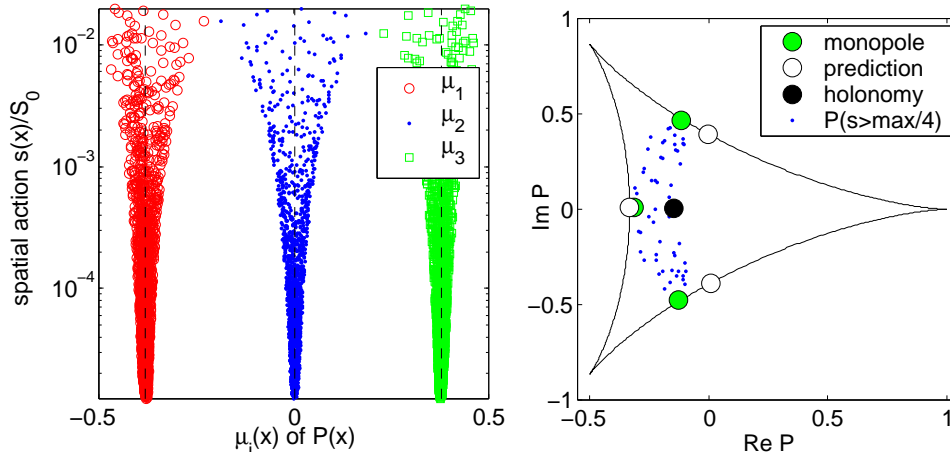


Figure 5.8: scatter plot of eigenvalues of $\mathcal{P}(\vec{x})$ versus the spatial action (left) and scatter plot of $P(\vec{x})$ in the complex plane with constituent monopoles (points where eigenvalues coincide) and predictions

From the observables measured on this gauge field it can be seen in Tab. 5.7 that the caloron with non-trivial holonomy is not static ($\delta_t = 0.23$) and that there are no further dyonic lumps visible (only one relevant local extremum in the local topological charge $q(x)$ and in the local action $s(x)$). The action density and the topological charge density allow no substructure but the Polyakov loop does. However, the prediction of $\mathcal{P}(\vec{y})$ by Eq. 3.21 deviates from its actual value, shown in Tab. 5.8.

ξ	t	x	y	z	IPR
0.0	3	06	09	06	4.5
0.1	3	05	09	05	6.8
0.2	3	05	09	05	9.4
0.3	3	06	09	05	8.1
0.4	3	06	09	05	6.2
0.5	3	06	09	06	6.4
0.6	3	06	09	06	6.3
0.7	3	06	09	07	8.1
0.8	3	06	10	07	9.3
0.9	3	06	10	07	6.6
1.0	3	06	09	06	4.5

	prediction	found
\vec{y}_1	$0.01 - 0.39i$	$-0.12 - 0.47i$
\vec{y}_2	$0.00 + 0.39i$	$-0.12 + 0.47i$
\vec{y}_2	$-0.33 - 0.01i$	$-0.32 + 0.01i$

x	y	z	enumeration
5	9	4	1 st
6	10	8	2 nd
6	8	6	3 rd

Table 5.8: This table shows the localisation of the fermionic density (left) and the prediction of $\mathcal{P}(\vec{y}_n)$ compared with the actual finding (upper right).

The consistent ordered monopoles are shown in the lower right part of Tab. 5.8. Again the zero-mode should be placed on the 1st constituent for $\xi \in (0, 0.4)$ on the 3rd for $\xi \in (0.4, 0.6)$ and for $\xi \in (0.6, 1)$ on the 2nd. Simply because constituents strongly overlap this behaviour is barely visible. The fermionic part in the same table shows that there is a no jumping over large distances and no full delocalisation for the zero-mode which would be the case at $\xi = \{0, 0.4, 0.6\}$ if separated monopoles would

be present. The *slight movement* along the z -axis visible in Tab. 5.8 or Fig. 5.10 and the variation of the inverse participation in ratio in Fig. 5.9 at the suspected values of ξ are hints to the non-trivial substructure, that can also be seen in the Polyakov loop pattern in Fig. 5.8. Further evidence for the constituent picture comes from the fact, that the topological charge density, shown in Fig. 5.7 and Fig. 5.10, is not rotational symmetric around the center of mass like it would be expected for an instanton gauge field. It is rather extended in the z -direction.

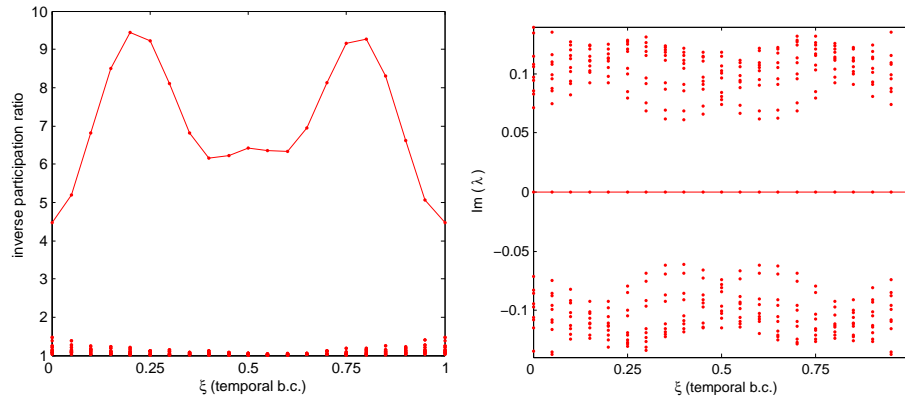


Figure 5.9: inverse participation ratio (left plot) and imaginary eigenvalue-flow (right plot) as a function of the temporal boundary condition

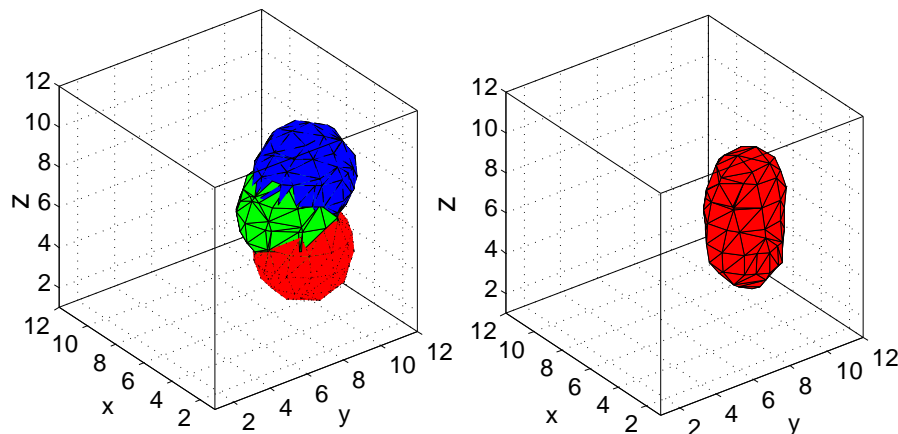


Figure 5.10: zero-mode density ρ for $\xi = \{0.2, 0.5, 0.8\}$ (red/points, green/lines, blue/dashed) (left) and topological charge density (right) as isosurface plots

The later analysis makes clear why it is not possible to obtain a $|Q| = 1$ static solution with dissociated dyonic structure using Wilson gauge action and simultaneously insisting on minimal violation of the equation of motion (as they are defined here) even among a large statistics of cooled gauge fields. The cooling history⁴ for this configuration shows, that this solution was already static during the process of cooling. In the last stage of cooling however the dyonic constituents merge, the action density becomes non-static and only afterwards the stopping criterion (A) is

⁴observables are measured during the process of cooling to see, what is 'dynamical' preferred

fulfilled. The importance of non-trivial holonomy is still visible but the moduli space of classical solution cannot be fully explored using this standard cooling method !

In order to illustrate how cooling with Wilson gauge action acts on a gauge field and how the instability of calorons evolves, a cooling history for the total action S/S_0 , the topological charge Q and the non-staticity δ_t are shown for this example in Fig. 5.11. That the dynamical effect of suppressing static calorons can be reduced by the stopping condition (B) is also illustrated in the same figure. The states of cooling where the stopping criteria apply are marked with (A) and (B).

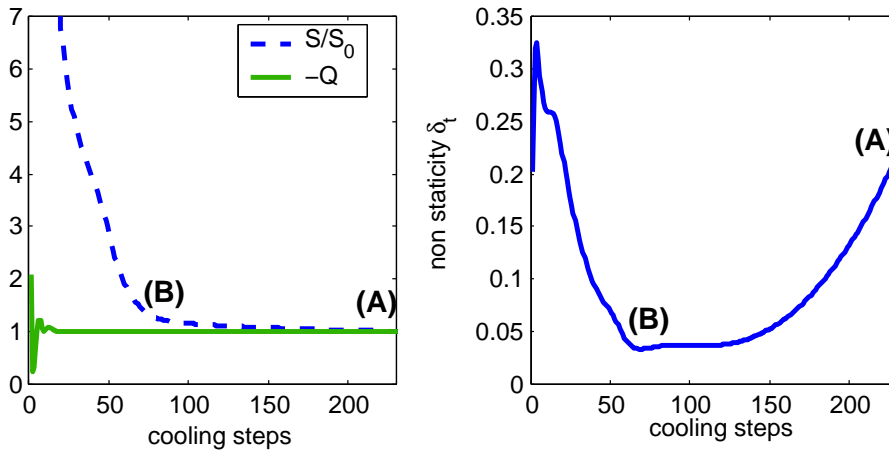


Figure 5.11: This figure shows the cooling history for configuration 157. The (left) figure shows the action normalised to instanton units and the topological charge, while the (right) figure shows the non-staticity δ_f as a function of the cooling sweeps.

As usual the topological charge settles early in the cooling history, even if the gauge field is far from being self-dual. The gauge field only has to be sufficiently smooth in order to possess a well defined topological charge. The monotonic decreasing action reaches a plateau $S = S_0 |Q|$ only in the last stage of cooling before the stopping condition (A) is fulfilled (in the last cooling step). In the right plot in Fig. 5.11 it is visible that the gauge field reaches a plateau after 60 cooling steps where it is static for 50 – 100 cooling steps. During these 50 – 100 cooling steps the constituent monopoles approach each other and the action density becomes time-dependent. One can prevent this behaviour using an improved action like over-improved action that prevents instantons from shrinking or caloron constituents from approaching each other [27, 74]. Another possibility is to use some modified stopping criterion like (B), that triggers to static calorons and would stop here after ≈ 60 iterations. But first the effect of cooling by the use of the improved action is tested.

5.3.2 Non-trivial caloron from improved cooling

The following example is a caloron with maximally non-trivial holonomy, obtained from cooling with the over-improved action according to Eq. 4.7. Actually, this 4×12^3 lattice gauge field was the first cooled gauge field with charge 1 obtained with cooling and still unmodified stopping condition (A). Using improved actions for cooling is known to stabilise instantons and to prevent them from shrinking and finally falling through the lattice [27, 74]. Any lattice gauge action S_{latt} explicitly breaks the scale invariance of the instanton solution

$$S_{latt}[U, \rho, a] = S_0 \left(1 + \left(\frac{a}{\rho} \right)^2 d_2 + \mathcal{O}(a/\rho)^4 \right) \quad \text{for } \rho \gg a. \quad (5.5)$$

The sign of the coefficient d_2 determines whether the instanton shrinks or inflates. Since cooling lowers the lattice action it is accompanied by a decreasing the instanton radius ρ if $d_2 < 0$ and by an increasing radius ρ (stabilising effect) for $d_2 > 0$. For standard Wilson gauge action one has $d_2 < 0$ and the instanton will shrink. For the square action Eq. 4.7 $d_2 = -\epsilon/5$ is known [27] and called over-improved action for the choice $\epsilon = -1$. We also observed that one will more likely obtain a dissociated, static charge 1 caloron if using the over-improved action with stopping condition (A). This example is obtained from an ensemble of $\mathcal{O}(100)$ gauge fields which were cooled with the over-improved action. It is characterised by the following observables.

Cooled caloron with improvement	
S/S_0	1.19
Q	1.00
δ_F	0.19
$\text{index}(\not{D})$	1
δ_t	0.05
-0.381	
holonomy $\{\mu_i\}$	$\mu_i =$ 0.044
0.337	
local extrema of $q(x)$	$r_1 = (4, 10, 10, 03)$ $r_{2a} = (4, 08, 06, 03)$ $r_{2b} = (4, 07, 05, 03)$
monopole position	$\vec{y}_1 = (10, 10, 03)$ $\vec{y}_2 = (06, 03, 04)$ $\vec{y}_3 = (08, 06, 02)$

Table 5.9: gluonic observables of CFG92OI

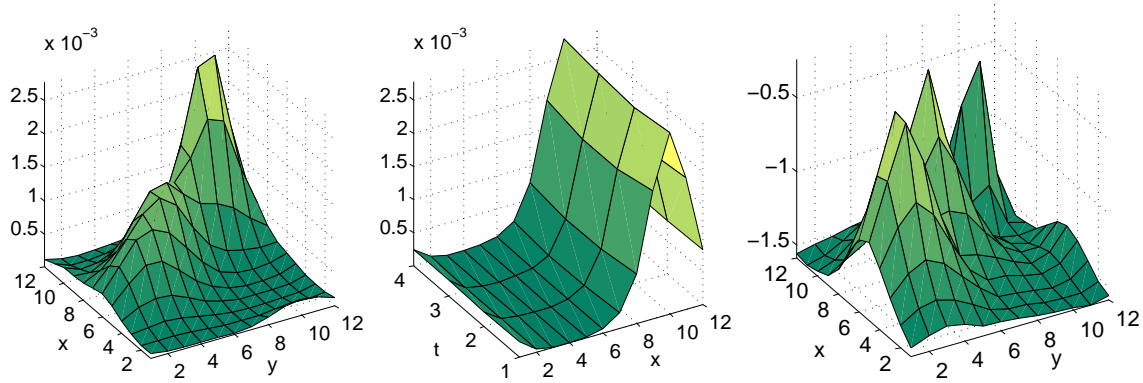


Figure 5.12: topological charge density (left,middle) and position of the constituent monopole (right)

ξ	t	x	y	z	IPR
0.0	4	10	10	03	2.6
0.1	4	10	10	03	5.9
0.2	4	10	10	03	6.9
0.3	4	10	10	03	3.4
0.4	2	07	05	03	1.4
0.5	4	08	05	03	3.3
0.6	4	07	05	03	3.8
0.7	4	07	04	03	3.5
0.8	1	06	03	04	3.7
0.9	1	06	03	04	2.3
1.0	4	10	10	03	2.6

	prediction	found
\vec{y}_1	$0.15 - 0.30i$	$+0.09 - 0.32i$
\vec{y}_2	$-0.00 + 0.39i$	$-0.08 + 0.44i$
\vec{y}_2	$-0.34 + 0.18i$	$-0.34 + 0.19i$

x	y	z	enumeration
10	10	3	1 st
6	3	4	2 nd
8	6	2	3 rd

Table 5.10: This table shows the localisation of the fermionic density (left) and the prediction of $\mathcal{P}(\vec{y}_n)$ compared with the actual finding (upper right). The (lower right) part shows the monopoles positions, enumerated by the analytic relation between holonomy eigenvalues $\{\mu_m\}$ and the m^{th} constituent.

The profile of the local topological charge shows separated self-dual lumps. Although only two self-dual lumps are identified through the topological charge density Tab. 5.9, three distinguishable monopoles are identified using the Polyakov loop criterion Fig. 5.12. The monopole positions are reproduced by the localisation of the zero-mode for the corresponding values ξ of the temporal fermionic boundary condition. The distribution of the local Polyakov loop in Fig. 5.13 also shows the triangle like behaviour, which was already observed in case of the KvBLL caloron with non-trivial holonomy. The Polyakov loop, as it is predicted from the asymptotic holonomy in Fig. 3.21, is also reproduced for the extremal points in Fig. 5.13 in this case. That no pronounced KvBLL caloron with three constituents was observed on the 4×12^3 can be understood because of the *small volume*. Earlier studies for $SU(2)$ were performed on a 4×16^3 lattice! It might also be that using improved gauge actions is not sufficient to fully cure the instability for calorons with periodic

boundary conditions⁵. Hence a refinement of the stopping criterion is useful, also if an improved action is available for cooling.

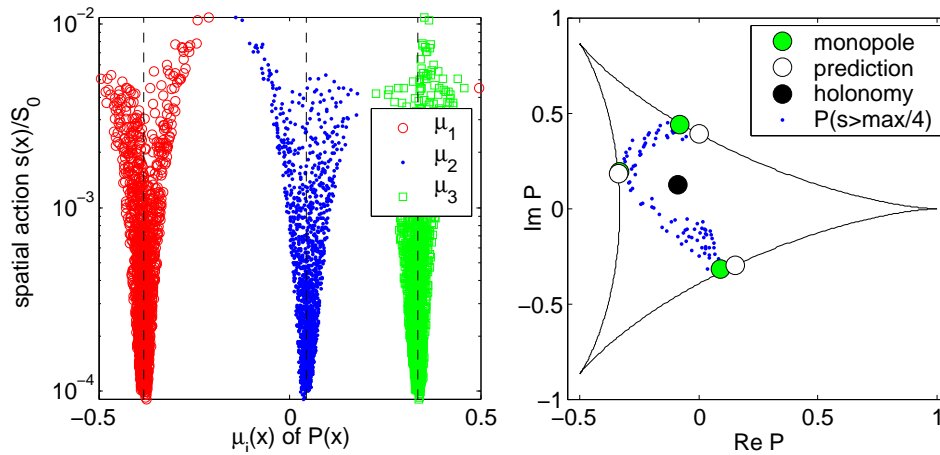


Figure 5.13: distribution of Polyakov loop values with the prediction of monopoles from the asymptotic holonomy.

A more detailed fermionic analysis is shown for this gauge field. The zero-mode of the $Q = 1$ gauge field is a γ^5 eigenfunction with $\lambda_0^5 = -1.000$ ($n_- = 1$, $n_+ = 0$). The corresponding eigenvalue of the Dirac operator λ_0 has a real part $\propto 10^{-4}$ and an imaginary part that is zero on the level of the computational accuracy⁶. For non-zero-modes the γ_5 matrix element $\int d^4x \psi(x)\gamma_5\psi(x)$ is zero up to the numerical precision. In Tab. 5.9 it is visible, that the zero-mode is localised at the monopole position for the proper value of the boundary condition.

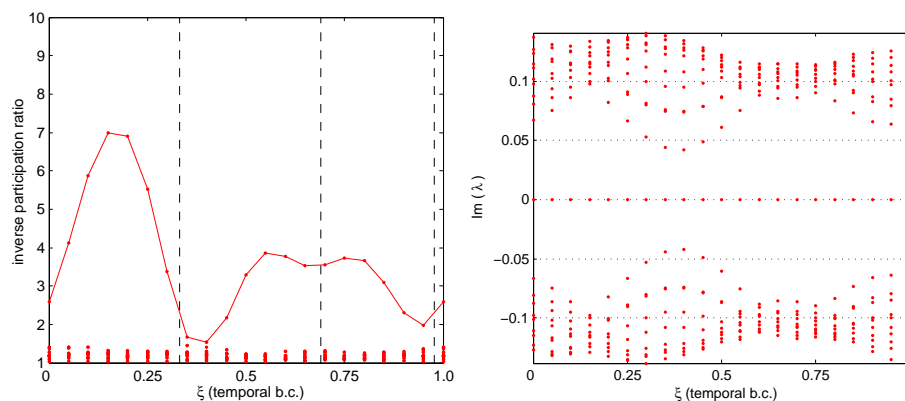


Figure 5.14: inverse participation ratio (left) and imaginary eigenvalue-flow (right) as a function of the temporal boundary condition.

⁵It is known for $SU(2)$ that using improved gauge action *or* suitably twisted boundary conditions charge 1 calorons become ultimately stable on the lattice [27, 74].

⁶single precision $\propto 10^{-8}$ is used for the fermionic investigation

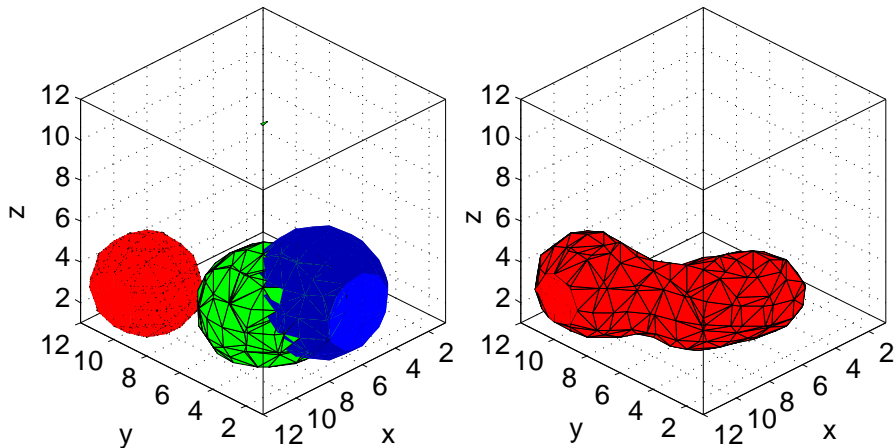


Figure 5.15: localisation of the zero-mode density (left) and the corresponding isosurface of the topological charge (right). The red (dotted) surface corresponds to $\xi = 0.3$, the green (full lines) to $\xi = 0.6$ and the blue (without lines) to $\xi = 0.8$.

The inverse participation ratio and the eigenvalue flow for various boundary conditions is shown in Fig. 5.14. The zero-mode delocalises and changes the position Tab. 5.9, similar to the analytical solution or the discretised KvBLL caloron with non-trivial holonomy in Fig. 5.3. The actual localisation of the zero-mode for different values of ξ is also shown in Fig. 5.15 and can be compared with the topological charge density, which is also shown there.

The properties of the discretised KvBLL caloron are reproduced by the gauge field which was produced by over-improved cooling. The dissociation into three dyons can already be seen from the monopole content Tab. 5.9 and the non-trivial pattern of the Polyakov loop in Fig. 5.13 although only two maxima are visible in the topological charge density Fig. 5.12. These findings are corroborated by the behaviour of the spectrum of the Dirac operator in Fig. 5.14 and Fig. 5.15.

5.3.3 Summary for $|Q| = 1$ calorons

The KvBLL calorons, which are discretised and put on the lattice are the reference examples for the analytical behaviour of KvBLL calorons. The analytical behaviour for the action and topological charge density, the Polyakov loop and the spectrum of the Dirac operator for these references is reproduced by cooled gauge fields.

For the calorons, which are obtained by different cooling actions and the stopping criterion (A) a similar behaviour is found. Using Wilson gauge action to obtain (anti) self-dual gauge fields by cooling with usual stopping condition (A) is not suitable to get static KvBLL calorons. The over-improved gauge action makes it more probable to see static and dissociated calorons but is more time consuming. Anyhow, even for non-static calorons with non-trivial holonomy a structure, e.g. in the Polyakov loop Fig. 5.8, is observed and points toward the importance of calorons with non-trivial holonomy. Since the moduli space of classical solution needs to be explored as far as possible a modified stopping condition like (B) needs to be introduced! An example that was obtained by the combined stopping criterion (B) with Wilson gauge action will be shown later in Sect. 5.6.

5.4 Cooled calorons with $|Q| = 2$

Caloron solutions with higher topological charge were known only for trivial holonomy. Recent works by Bruckmann et.al. [24] analytically expand this view with the explicit parametrisation of charge two calorons with non-trivial holonomy in case of $SU(2)$. Generic charge Q solutions in $SU(3)$ depend on $12|Q|$ parameters. This shows that the interpretation in terms of $|Q| = 1$ parameter has to be extended. Nevertheless, we remain investigating the charge two case with the observables, used in the last section. There is no technical restriction to obtain higher charges calorons on the lattice, like it can be seen in the distribution of topological in Fig. 5.16.

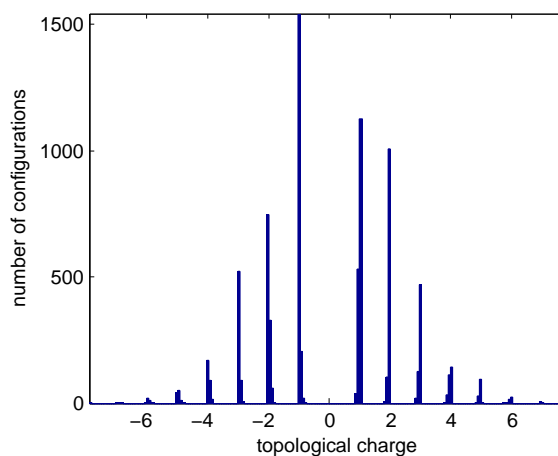


Figure 5.16: Distribution of topological charges for 4×12^3 lattice calorons.

There is no analytic expression for a $SU(3)$ KvBLL caloron with charge two so far available to us. Hence the further investigation classical solution with higher topological charge is restricted to gauge fields obtained by the cooling method. It is observed that the classical fields with $|Q| = 2$ also have the behaviour, that was found typical for the $|Q| = 1$ KvBLL caloron. These fields are not destabilised during cooling to such an extend, as it was shown to be unavoidable for lattice charge 1 calorons.

5.4.1 Caloron with non-trivial holonomy

In the case of $|Q| = 2$ it was possible to obtain classical gauge fields which persist longer on a self-dual plateau against cooling and have a lower violation of self-duality compared to $|Q| = 1$. This was already observed in a study of stability of self-dual gauge fields on the torus by Leinweber et.al [41]. Therefore the standard Wilson gauge action is, surprisingly, sufficient to obtain classical gauge fields with higher charges. In this case the combined stopping criterion (B) was used to stop cooling of the 4×20^3 lattice gauge field. This serves as an example for a static self-dual caloron with maximal non-trivial holonomy.

Cooled caloron	
S/S_0	2.04
Q	2.00
δ_F	0.04
$\text{index}(\not{D})$	2
δ_t	0.007
-0.3241	
holonomy $\{\mu_i\}$	$\mu_i =$
	0.0044
	0.3197
local extrema of $q(x)$	5 separated lumps shown in Fig. 5.17
monopole position	6 separated constituents shown in Fig. 5.17

Table 5.11: gluonic observables of CFG170

In Tab. 5.11 the global observables are shown. Contrary to the calorons with $|Q| = 1$ the violation of the equation of motion $\delta_F = 0.04$ is small. The low value of the non-staticity already points out the dissociated nature of the caloron. This becomes evident by identifying the constituents by the topological charge density, the zero-mode density or the monopoles of this fields. In Fig. 5.17 the localised constituents of the caloron are visualised by showing the action density and the function $f(\vec{y})$, defined in Eq. 5.3, as an isosurface⁷ plot. The six constituents can be counted in this figure if one avoids double counting due to the periodic boundary conditions. Hence these observables make sense to investigate on the characteristic behaviour of these fields.

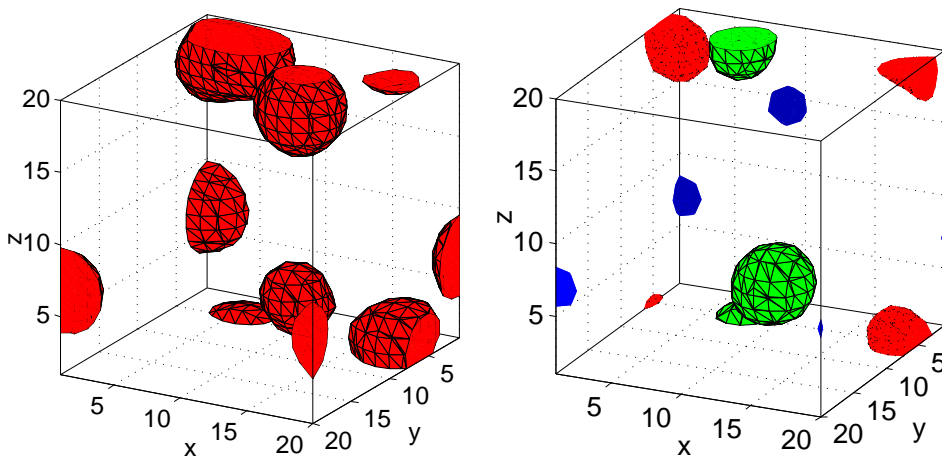


Figure 5.17: spatial topological charge density $q(\vec{x}) = \sum_t q(x)$ (left) and constituent monopoles by and isosurface plot of $f(\vec{x})$; note that two constituents overlap in $q(x)$

⁷For a charge 2 solution with six constituents this is much more transparent than showing 2d surface plots.

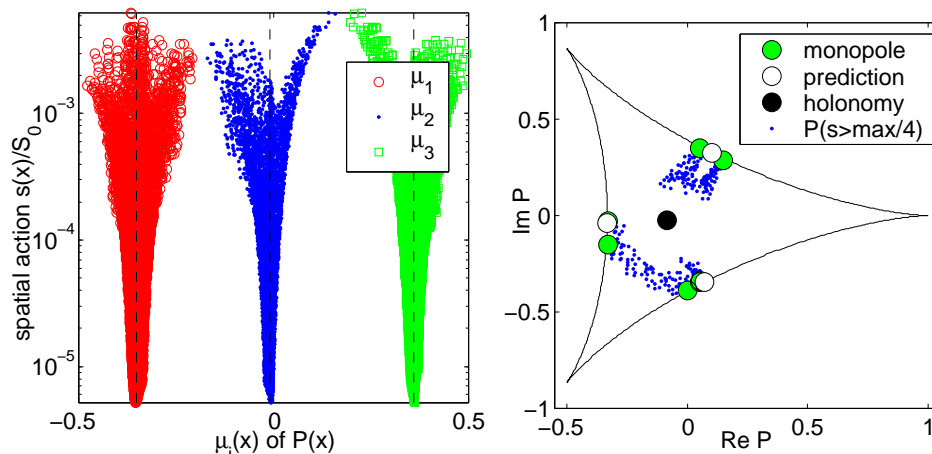


Figure 5.18: definiteness of holonomy as eigenvalues are plotted versus the spatial action (left) and the scatter-plot of Polyakov loop (right) with predictions from the holonomy and the monopoles, which were found.

Again the holonomy is well defined, since the eigenvalues of the Polyakov loop in Fig. 5.18 become constant for points with a small spatial action. Especially the significant triangle pattern, known from the discretised KvBLL caloron with unit topological charge, becomes also visible (twice) in this figure. The constituents align their Polyakov loop in compliance with the asymptotic holonomy. The spectrum of the Dirac operator is again used and both zero-modes show the behaviour of a two KvBLL caloron superposition under the influence of the same asymptotic holonomy. Due to the degeneracy of the kernel of the Dirac operator, the choice of a special zero-mode or to track the ξ dependent flow only for one zero-mode seems artificial and an ordering the eigenmodes impossible. To overcome this ambiguity the sum over zero-modes

$$\rho_{\text{zm}}(x) = \sum_{\text{kernel } \not{D}} \psi_n^\dagger(x) \psi_n(x), \quad (5.6)$$

which does not depend on a special choice of base, is shown in Fig. 5.19. The left part of this figure shows again the monopoles, while the right one visualises ρ_{zm} for different values of ξ .

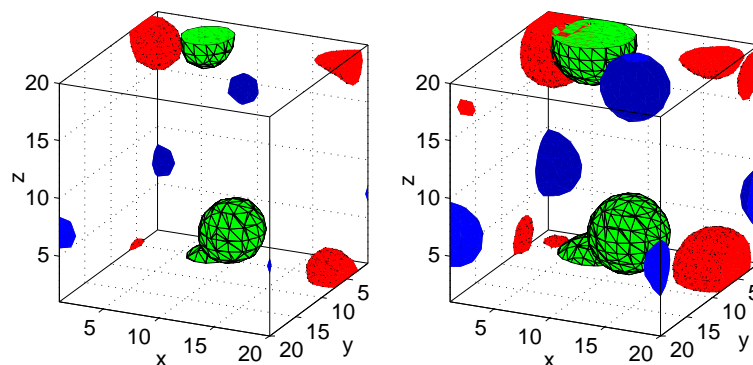


Figure 5.19: ρ_{zm} for different fermionic boundary conditions (red/points $\xi_1 = 0.15$, green/lines $\xi_2 = 0.5$, no shading $\xi_3 = 0.85$)

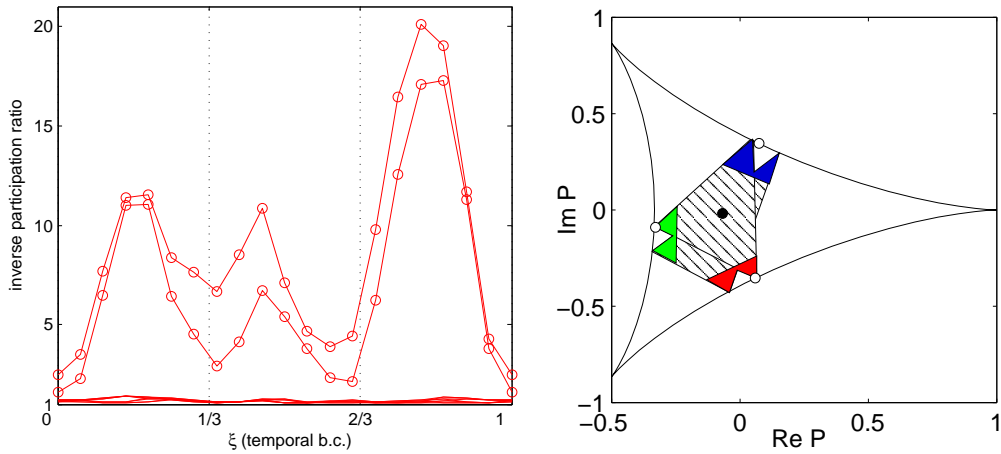


Figure 5.20: inverse participation ratio (left) and a sketch of Fig. 5.18

Neglecting the ordering problem, the behaviour of the inverse participation ratio in Fig. 5.20 and the localisation of a single zero-mode is very similar to the KvBLL caloron with non-trivial holonomy. The right panel of this figure shows how the colour code, which is used in Fig. 5.19, is associated with the Polyakov loop at the constituent. Using Eq. 3.21 this allows to order the constituents and to check whether the zero-mode is localised on the right constituent for some value of ξ . This is indeed the case because the zero-mode is localised on the

constituent	with colour code	b.c.
1 st pair	red (points)	for ξ_1 ,
2 nd pair	blue (no marks)	for ξ_3 ,
3 rd pair	green (lines)	for ξ_2 .

The jumping takes place in the order $1 \rightarrow 3 \rightarrow 2$, as it was explained in Tab. 5.4 and expected from the analytic solution of the $Q = 1$ KvBLL caloron, if the fermionic boundary condition ξ runs $0 \rightarrow 1$.

Using similar tools and observables like for the KvBLL caloron seems useful to explore the properties of higher charge calorons. At least with non-trivial holonomy and if well separated constituents the charge 2 caloron looks like a superposition of charge 1 KvBLL calorons but seemingly free of the instability of the charge 1 case. This is suggested by the Polyakov loop pattern and the investigation of the spectrum of the Dirac operator. A problem how to order the zero-modes makes it difficult to track the localisation of a fermionic eigenmode.

5.4.2 Caloron with trivial holonomy

It is not very probable to obtain a caloron that has trivial holonomy with cooling starting from the confinement phase. On the other hand the yield of higher charge calorons starting from the deconfined phase is low. Hence this caloron was cooled using fixed (cold) temporal links at the boundary. This means that $U_{x,\hat{1}} = \mathbb{1}$ is fixed for the x values at the spatial boundaries of the lattice during heating and cooling. After some amount of cooling the average Polyakov loop for this field is close to trivial holonomy and the fixed links are made dynamic again until a $|Q| = 2$ gauge field is obtained. To accelerate this process, the cooling was done for a $SU(2)$ gauge field on a 4×16^3 lattice. This fields was then embedded into $SU(3)$, after the violation of anti-selfduality was minimal (A) for the $SU(2)$ field.

(Semi)cooled caloron	
S/S_0	2.01
Q	-1.98
δ_F	0.02
index(\mathcal{D})	$4 - 6 = -2$ for $\xi = 0, 1$ $0 - 2 = -2$ for $\xi \in (0, 1)$
δ_t	0.17
holonomy $\{\mu_i\}$	0 $4 \cdot 10^{-2}$
local extrema of $q(x)$	2 separated narrow lumps
monopole position	not well defined (see Fig. 5.21)

Table 5.12: gluonic observables of cooled caloron

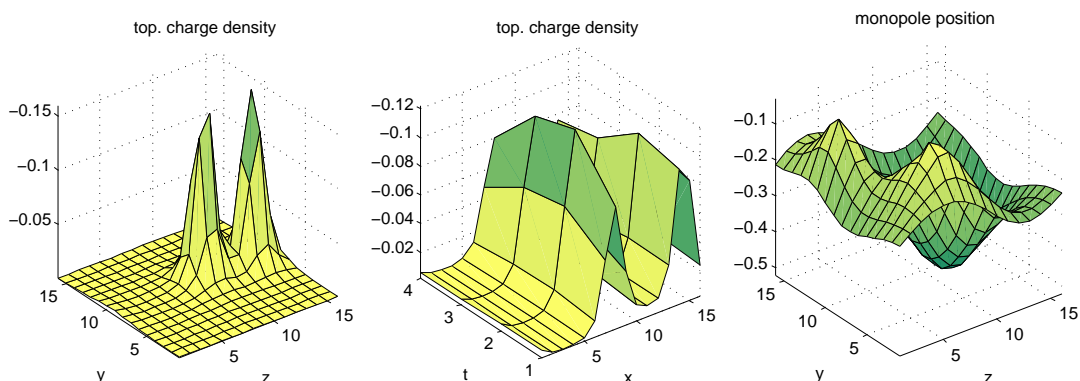


Figure 5.21: (left,middle) Topological charge density $q(x)$ and (right) the position of the constituent monopoles are shown.

Notice that the violation of anti-selfduality is very small for this field but that it is very narrow localised in space and not static. Like for the discretised solution it

makes no sense to define the monopoles by coinciding eigenvalues for trivial holonomy because they are massless and spread over a large region and hence cannot be recovered on the lattice.

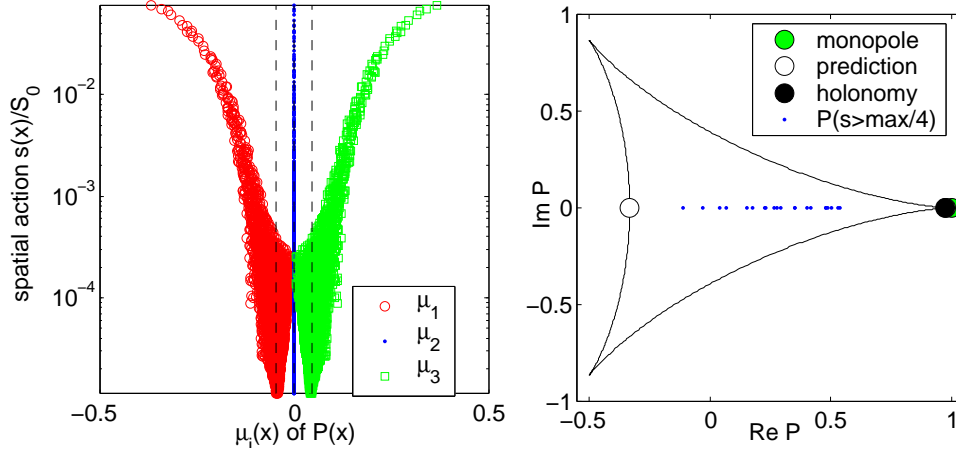


Figure 5.22: eigenvalues of Polyakov loop versus spatial action (left) and scatter plot of Polyakov loop in the complex plane (right)

The Polyakov loop is arranged like it was already seen for the constructed solution with trivial holonomy and approximately resembles the Harrington-Shepard caloron solution.

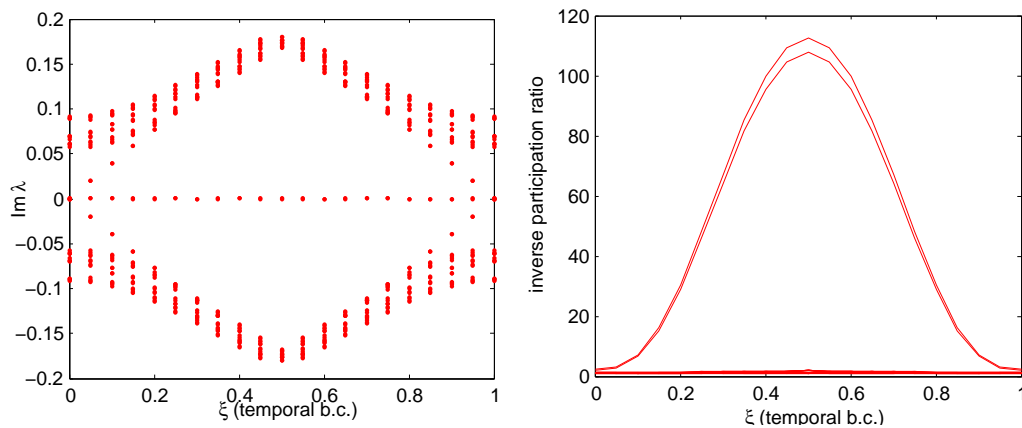


Figure 5.23: flow of imaginary part of eigenvalues (left) and inverse participation ratio for the two zero-mode densities (right)

It is noticeable, that the eigenvalues in Fig. 5.23 come close to zero. With the clover improved Dirac operator it is even possible to find six zero-modes for exact periodic boundary conditions. Summing up the chiral density of all zero-modes still gives rise to $\sum_{\text{kernel } \not{D}} \psi_n \gamma_5 \psi_n \approx 2$ for this operator (for details see Appendix B).

It is also visible that the inverse participation is maximal for antisymmetric boundary conditions and that the corresponding density $\psi^\dagger \psi^{(\xi=0.5)}$ is very narrow localised. This corresponds to the observations for the constructed KvBLL caloron with trivial holonomy.

5.4.3 Summary for $|Q| = 2$ calorons

Investigating higher charge (anti) self-dual gauge fields suffers less from instabilities than it is observed for calorons with topological charge 1. This is especially interesting since the knowledge of moduli space is still incomplete for $SU(3)$. To examine those gauge fields it is instructive to use observables like Polyakov loop, field strength and the spectrum of the Dirac operator with boundary conditions to probe the nearly (anti) self-dual gauge fields.

The general behaviour of KvBLL calorons is also found for the $|Q| = 2$ case with non-trivial holonomy on the lattice. In the example $|Q|N_c = 6$ lumps were found Fig. 5.17. These findings are confirmed by the maxima of the zero mode density and the monopole positions, defined by positions where the Polyakov loop eigenvalue approach each other. For trivial holonomy four of the six monopole constituents (of the charge two caloron) are massless and only two self-dual lumps are observed. The zero-modes are pinned down on top of each of those lumps and delocalise only for symmetric boundary conditions.

5.5 Caloron-anticaloron superposition with $Q = 0$

Since the stopping criteria (A) and (B) trigger to a local violation of (anti) self-duality, gauge fields which are described as a superposition of calorons and anti-calorons are also found with a low rate ($\approx 2\%$ for the 4×12^3 lattice). The violation of the equation of motion of those semi-classical objects is small if they are well separated. Therefore in the relatively small volume only objects with $S/S_0 = 3$ and $|Q| = 1$ or $S/S_0 = 2$ and $Q = 0$ are found. Here only one example with $S/S_0 = 2$ and $Q = 0$, which was cooled with criterion (A) and Wilson gauge action on a 4×12^3 lattice, is shown. This is also very interesting because generically a superposition of calorons and anti-calorons (or dyons and anti-dyons) rather than self-dual (or anti self-dual) KvBLL calorons are the relevant degrees of freedom in a semi-classical approach with a caloron liquid.

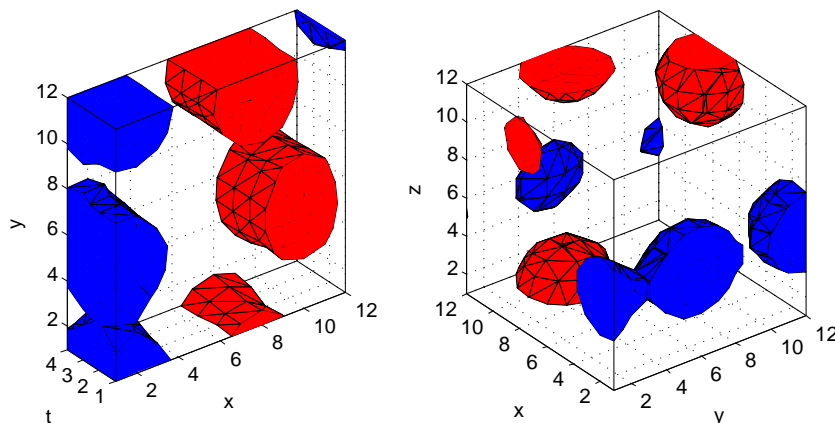


Figure 5.24: The local topological charge (red=positive, blue=negative) for different slices. The remaining direction is summed up.

The topological charge profile in Fig. 5.24 already shows that this gauge field is a superposition of a self-dual and an anti-selfdual caloron. The four local maxima give rise to a $SU(2)$ caloron-anticaloron superposition. The global gluonic observables of this gauge field are given in Tab. 5.13

Cooled caloron	
S/S_0	2.01
Q	$\approx 10^{-4}$
δ_F	0.17
$\text{index}(\mathcal{D})$	0
δ_t	0.06
holonomy $\{\mu_i\}$	$\mu_i = -0.18$ -0.08 0.26
local extrema of $q(x)$	$r_1^- = (2, 01, 06, 05)$ $r_2^- = (3, 02, 12, 05)$ $r_1^+ = (4, 10, 05, 01)$ $r_2^+ = (4, 08, 11, 11)$
monopole position	6 constituents

Table 5.13: gluonic observables of cooled caloron

The gauge field is static $\delta_t = 0.06$ and violates the equation of motion, given that it is a $S = 2S_0$ and $Q = 0$ field, with $\delta_F = 0.17$ in a moderate way. The Polyakov loop, which is almost degenerated to a real line, also motivates to speak of a $SU(2)$ embedding. However, it is possible to separate six monopole constituents in Fig. 5.25, defined by degenerated eigenvalues of the Polyakov loop.

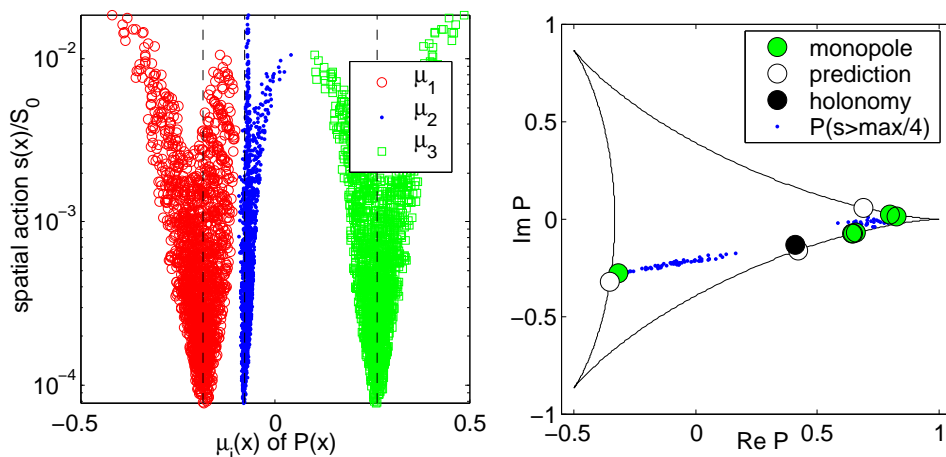


Figure 5.25: eigenvalues of Polyakov loop versus the spatial action (left) and the scatter plot of Polyakov loop in the complex plane (right)

The eigenvalue flow for the Dirac operator shows no zero mode for any value of the boundary condition. Nevertheless it is interesting to see the flow and investigate

on the properties of the low lying eigenmodes. For this configuration a jumping for these near zero-modes is visible Tab. 5.14.

ξ	$\text{Im } \lambda / 10^{-3}$	t	x	y	z	IPR
0.0	4.8	3	02	12	05	2.8
0.1	8.5	3	02	12	06	1.6
0.2	8.9	3	01	06	06	1.3
0.3	8.0	3	01	06	05	2.9
0.4	9.1	3	01	06	05	5.3
0.5	8.7	3	01	06	05	5.7
0.6	4.9	3	01	06	05	3.6
0.7	5.7	3	01	06	06	1.6
0.8	13	3	02	12	05	1.8
0.9	8.1	3	02	12	05	3.2
1.0	4.8	3	02	12	05	2.8

Table 5.14: the behaviour of the eigenmode of \mathcal{D} with the smallest positive imaginary part. Since the mode with λ^* can be obtained by $\gamma_5 \psi_\lambda$, IPR and position will be the same for this pair and is not shown.

In Fig. 5.26 the eigenvalue flow is shown. For the superposition of classical gauge fields with a self-dual and an anti-selfdual part the index theorem is only trivially fulfilled with $n_+ = n_- \equiv 0$.

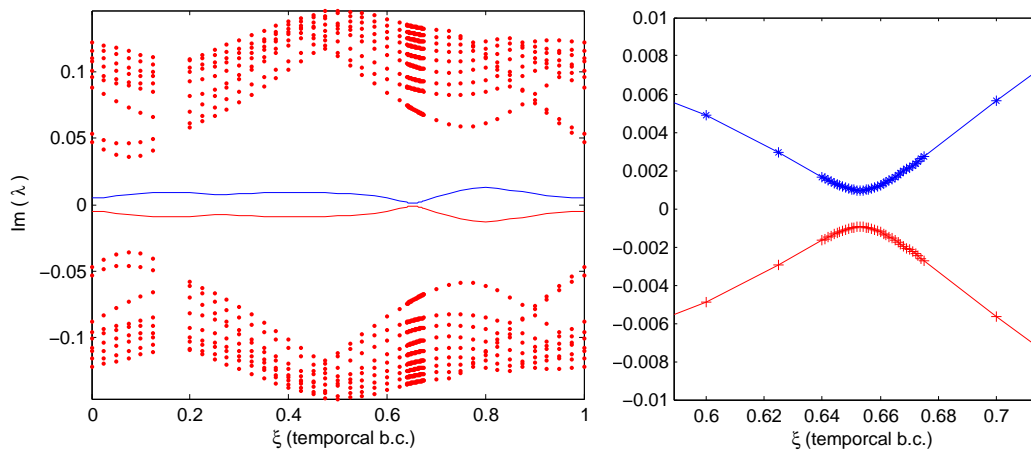


Figure 5.26: Flow of $\text{Im}(\lambda)$ of as a function of b.c. with a closer look at the region of interest. No crossing happens!

Since only two jumps are observed in Tab. 5.14 and Fig. 5.27 (rhs) possibly not all 'hot-spots' (caloron constituents) are visited. Looking at the chiral density for anti-periodic boundary conditions Fig. 5.27 shows that the mode is always located on *two* positions, which correspond to opposite topological charge (compare with Fig. 5.24 rhs.).

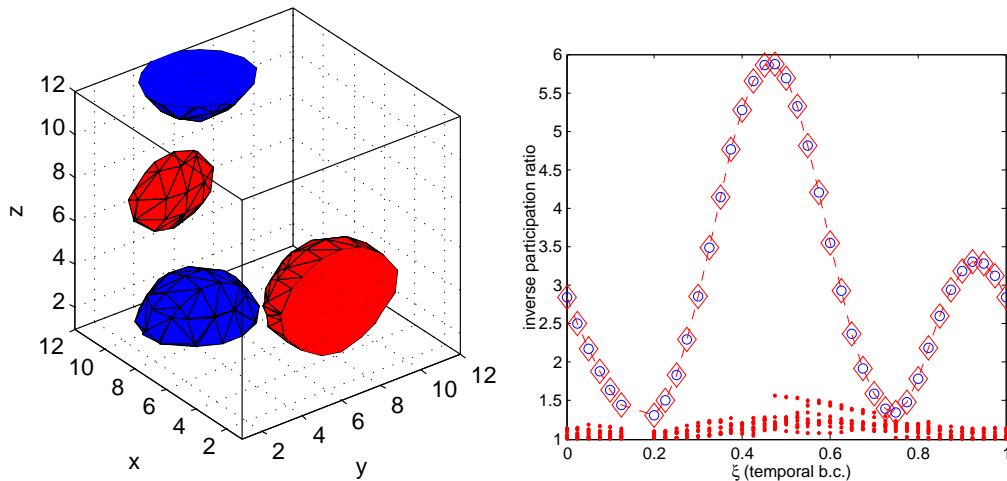


Figure 5.27: (left) chiral density $\psi\gamma_5\psi$ for anti-periodic b.c. $\xi = 0.5$ and inverse participation ratio IPR as a function of b.c.; circles (diamonds) show the IPR of lowest positive (negative) eigenvalue respectively

A new feature shown in Fig. 5.27, which explicitly shows that near zero-modes are entangled with the behaviour of the calorons, is that non-zero-modes are also localised $IPR > 1$. For previously shown purely (anti) self-dual calorons the non-zero-modes had $IPR \approx 1$ with a weak dependence on the boundary condition. For the next-to-zero mode of the present $Q = 0$ example a localisation behaviour similar to the KvBLL caloron is unlikely since the eigenmodes of \not{D} are obviously not chiral.

Resuming this section it can be seen that one can obtain also classical gauge fields with $S/S_0 > |Q|$, but these fields violate the equation of motions if the self-dual and anti-selfdual lumps are not sufficiently separated. The behaviour of the Dirac operator is *not simply a superposition of a positive and negative chiral mode* since the degeneracy of eigenvalues is lifted through an caloron-anticaloron interaction. Hence one must be cautious with the interpretation of jumping. Nevertheless, the low lying eigenmodes modes also show a localisation behaviour closely related to the classical solution.

5.6 Fitting an analytical expression

Although the gauge field is practically impossible to fit, there are observables like the action density $s(x)$ Eq. 3.21 or the zero-mode density $\rho(x)$ Eq. 3.22 which are easily accessible and where analytic formulas are known for $SU(3)$ (or even $SU(N)$). The gauge field on which such a fit is attempted is obtained by cooling with Wilson gauge action and stopping condition (B). The lattice geometry is 4×20^3 . This gauge field has the topological charge $|Q| = 1$ and maximally non-trivial holonomy. Since the constituents are well separated the KvBLL pattern is very pronounced.

The most promising analytic expression for a fit is the zero-mode density. Since the zero-mode is only localised on one constituent at a time the effect of the boundary conditions can be minimised. Therefore the $\xi \equiv 1 - z$ values⁸ with the maximal

⁸the definition fermionic b.c. is against the literature

localisation $z_m = 1/2[\mu_m + \mu_{m+1}]$ are chosen. For maximally non-trivial holonomy this happens at $z = \{1/6, 1/2, 5/6\}$. The formula Eq. 3.23 for the Green function $\hat{f}_x(z, z')$, which enters the definition of the fit function $\psi^\dagger \psi^{(\xi)}$, simplifies in the case of well separated monopole constituents and $z \in [\mu_m, \mu_{m+1}]$ to

$$\hat{f}_x^{zm}(z, z) = \pi(r_m \beta)^{-1} \tanh(\pi r_m \nu_m / \beta). \quad (5.7)$$

From this the zero mode density can be calculated by Eq. 3.23 and, for the three values of ξ , the matching with the theoretical prediction is performed by minimising the function

$$\chi = \sum_x \left| \psi^\dagger \psi(x) - (\psi_\xi^\dagger \psi_\xi)^{zm}(x) \right|$$

with respect to the constituent position \vec{y}_n and its mass ν_n . But first have a glance at the gluonic and fermionic observables. In Fig. 5.28 an isosurface plot for the topological charge density and for the zero-mode density is shown. The effect of the periodic boundary conditions is clearly visible what makes it difficult to fit the analytic formula for the action density to the lattice profile.

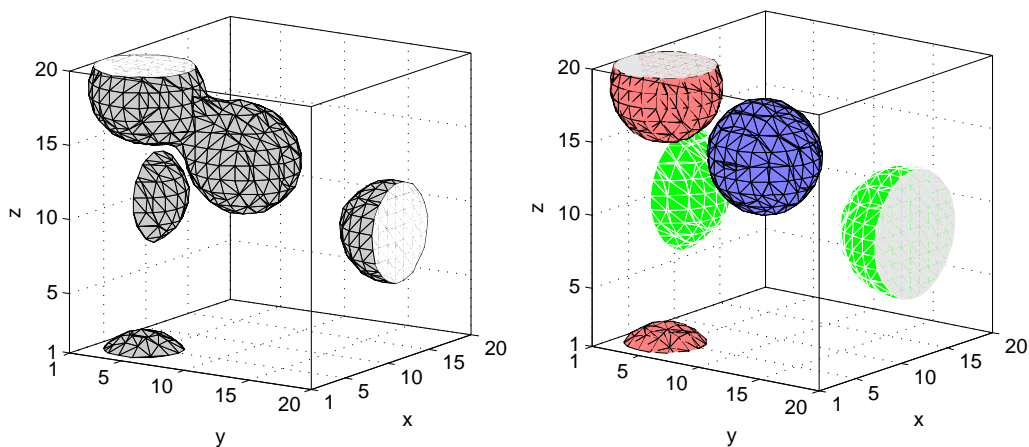


Figure 5.28: (left) isosurface plot of spatial part of topological charge density; (right) the zero-mode density $\psi^\dagger \psi$ for $\xi_1 = 1/6$, (red sphere/dashed lines), $\xi_2 = 1/2$ (green/white lines) and $\xi_3 = 5/6$ (blue/black lines) for ξ_i

The monopole constituents, defined by the positions of coinciding eigenvalues of the Polyakov loop operator or by the center of mass of self-dual lumps, fall together with the maximum of the zero-mode density $\rho(x)$ for the different boundary conditions. This feature shows very impressively the connection of the analytical prediction for the KvBLL caloron and the numerical result for classical gauge fields which are obtained from cooling. Note that the localisation shown in Fig. 5.29 is indeed maximal for $\xi = \{1/6, 1/2, 5/6\}$. From the gluonic observables the following parameters are determined. The actual holonomy is $\mu_m = \{-0.363, -0.001, 0.364\}$ ($\nu_m = \{0.364, 0.361, 0.275\}$).

dyon	monopole position	$P(\vec{y}_i)$
1 (red)	$\vec{y}_1 = (05, 04, 19)$	$0.096 - 0.323 i$
2 (blue)	$\vec{y}_2 = (09, 10, 14)$	$0.061 + 0.341 i$
3 (green)	$\vec{y}_3 = (12, 20, 09)$	$-0.328 + 0.030 i$

constituent	ξ	x	y	z	$\alpha = \pi\nu_m/\beta$	χ_{\min}
1	0.15	4.8	4.3	18.6	0.36	0.04
3	0.50	11.5	19.3	9.6	0.28	0.06
2	0.85	8.8	9.5	13.7	0.34	0.05

Table 5.15: positions from monopoles and holonomy (upper table) and parameters from fit (lower table)

The positions, which now can take non-integer values are shown in Tab. 5.15. Since the eigenmodes are normalised, the value of $\chi(\xi = 0.15) = 0.04$ corresponds to a deviation of 4% what is mainly due to the periodic spatial boundary conditions. In Fig. 5.30 one can see that this fit is nevertheless working good and deviates for small densities.

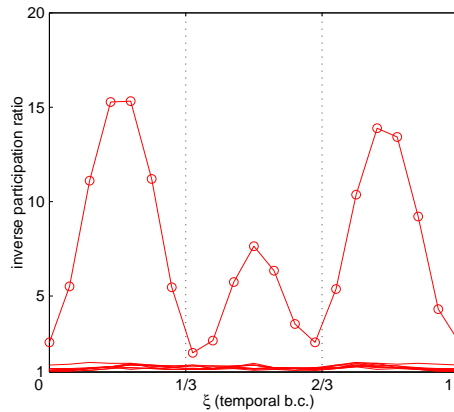


Figure 5.29: inverse participation ratio IPR as a function of the fermionic b.c.

The eigenmode density is shown in the left part of Fig. 5.30 for the density (full lines) of the zero-mode determined by ARPACK and compared with the fitted density (dashed lines). In this plot the coordinates $t = 2$ and $z = 19$ are fixed and the dependence of $\psi^\dagger\psi$ on x is shown. Different lines correspond to different values of y so that $\psi^\dagger\psi$ in the $x-y$ plane is sufficiently covered. Clearly the fit is not compatible with the periodic boundary conditions at $x \approx 15$. Nevertheless the density is well described where the fit is not effected by the boundary condition. The right plot of the same figure shows that action density. Obviously the periodic boundary conditions are not fulfilled but the isosurface looks very similar to Fig. 5.28.

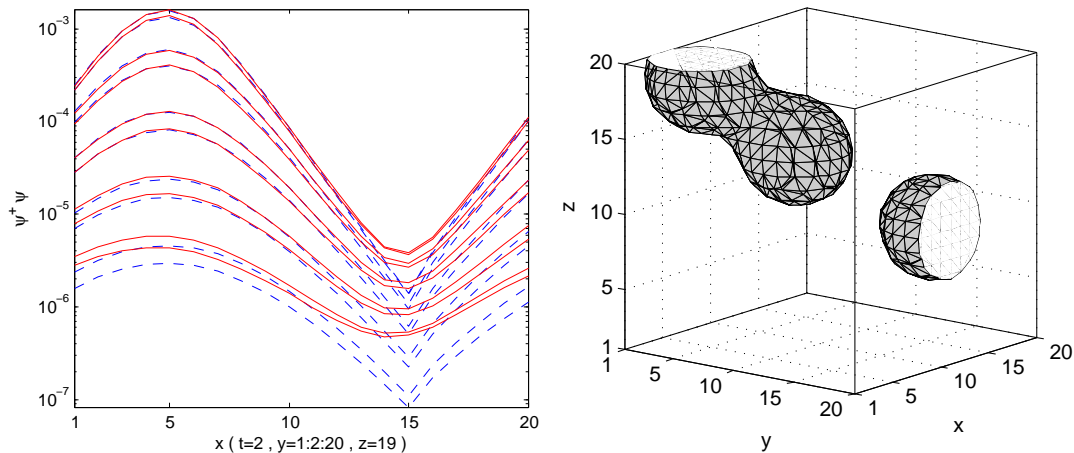


Figure 5.30: fit to the eigenmode for $\xi_1 = 0.15$, dashed lines shows analytical prediction, full lines show $\psi^\dagger\psi$ obtained by ARPACK (left) and analytical spatial action with input from fit (right)

5.7 Summary

The local structure of analytic and discretised KvBLL solutions is reproduced for calorons obtained by different actions and stopping conditions. The composition of the caloron moduli space found after cooling actually depends on the method that is used. For $|Q| = 1$ this effect is most striking. For example, it is not possible to obtain static charge 1 calorons by cooling with respect to Wilson gauge action and using the minimal violation of self-duality (A) as a stopping criterion. Still the structure can only be described in terms of KvBLL calorons with non-trivial holonomy in the sector of less separated constituents. The non-trivial substructure is always visible for calorons with non-trivial holonomy. Only with the use of improved actions or an alternative stopping criterion static and dissociated calorons with charge 1 can be found.

Problems of stability apparently do not exist for the examples of classical lattice gauge fields with higher topological charge. This might be a hint that the instability is indeed connected with the instability of classical solution with charge 1 on the torus [55]. Some recent studies [41] affirm that this effect might be observable on the lattice. In some cases a caloron with $|Q| = 2$ might be interpreted as a superposition of KvBLL calorons with unit topological charge, which does not see the instability of its caloron building block.

Fitting to analytical formulas for the KvBLL solution has systematic uncertainties due to the spatial periodic boundary conditions on the lattice. This makes fitting only possible if these effects might be neglected. This is the case for the zero-mode, since it is localised only on one monopole constituent. From these examples one must conclude that the characteristic behaviour of $SU(3)$ KvBLL calorons is found on the lattice!

Chapter 6

Classical solutions on the lattice - statistical properties

So far the classical gauge fields were only discussed on an exemplary basis. The next step is to make a statistical analysis on a larger set of classical gauge fields. In the forthcoming chapter the moduli space of the self-dual gauge fields is explored and compared to the known behaviour of KvBLL-caloron solutions. Several lattice sizes are used to investigate the dependence on the aspect ratio N_t/N_s . For this purpose again the topological charge, action density, Polyakov loop and the spectrum of the Dirac operator, which were found to characterise the examples, are measured on a large number of cooled gauge fields. Due to the experience gained in the investigation of examples in the previous chapters it is clear that cooling with Wilson gauge action is sufficient to accomplish this task if the combined stopping criterion (B) is used. Improved or over-improved cooling would be better but requires much more computer time.

Due to the fact that there is no strict self-dual $|Q| = 1$ solution on the torus T^4 [55] drastic differences between charge 1 and self-dual fields of higher topological charge are expected to show up in a lattice study. This was already observed in the last chapter and will become more pronounced with statistics. First searches for classical solutions failed to find any static charge 1 solution, consisting of several separated monopole constituents (or dyons) and rather a non-static (anti) self-dual lump containing all action S_0 was observed instead. A showcase for this behaviour was discussed in Sect. 5.3.1. After recalling the problem inherent to stopping condition (A) with respect to the the statistical properties only the combined stopping condition (B) will be used to explore a large part of the caloron moduli space. This underlines our previous findings and supports the claim, that KvBLL calorons with non-trivial holonomy can be seen on the lattice and become important degrees of freedom in the confined phase.

6.1 Problems finding calorons in $SU(3)$

The first ensemble of cooled gauge fields was produced by demanding that the violation of (anti) self-duality goes through a minimum during the cooling, which is

stopped there. With this stopping criterion (A) an ensemble of 6000 classical 4×12^3 configurations is obtained from a Monte-Carlo ensemble. The sector with $Q = 0$ is omitted from the ensemble. The ensemble was generated using Wilson gauge action in the confined phase at $\beta = 5.65$. Like the example Sect. 5.3.1, each configuration has been cooled with respect to the Wilson gauge action. Non-trivial holonomy is no exception but rather the generic case after cooling has stopped. This can be seen in the distribution of the modulus of the asymptotic holonomy $|P_\infty|$ in Fig. 6.1.

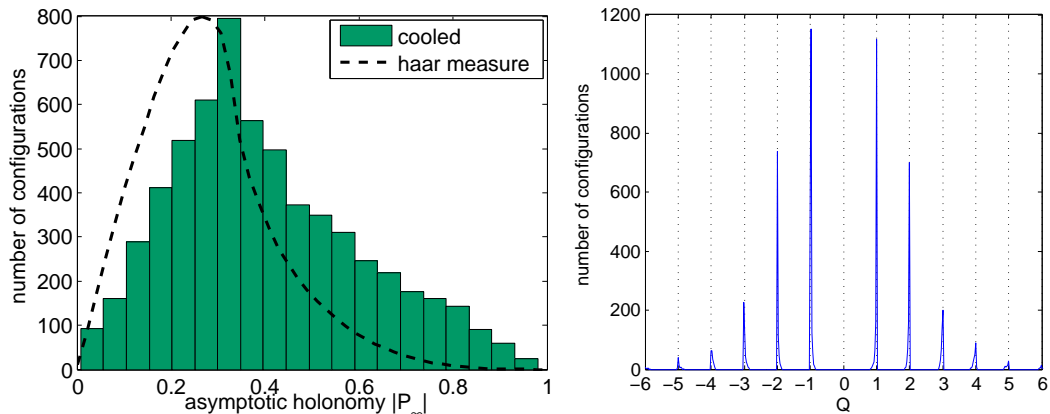


Figure 6.1: distribution of asymptotic holonomies for the whole ensemble (left) and distribution of topological charges (right)

Obviously, the (anti) self-dual lattice gauge fields obtained in this way cannot be described in terms of calorons with trivial holonomy. The distribution of the violation of the (anti) self-duality δ_F in Fig. 6.2 shows, that the gauge fields of the various topological sectors $|Q| \neq 1$ obtained with stopping criterion (A) are overwhelmingly close to being (anti) self-dual. The plot for $|Q| = 1$ alone shows a little surprise. One might have expected that calorons with smallest action, hence the calorons with $|Q| = 1$, violate the equation of motion on the lattice to a minimal extent. But the distribution for this charge shows that there exists a lower positive bound for the violation of self-duality δ_F by calorons.

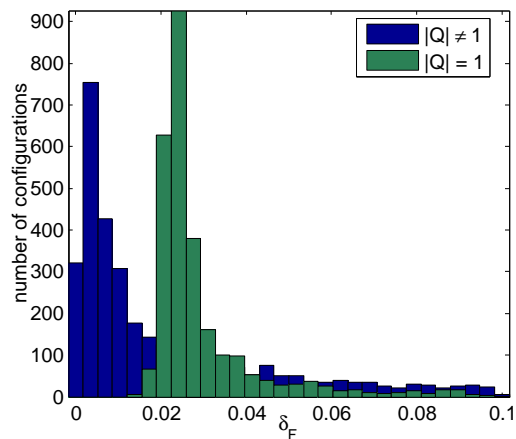


Figure 6.2: violation of self-duality δ_F

One can ask whether the moduli space is complete and in particular whether the ensemble contains static charge 1 calorons. In Fig. 6.3 the distribution of the non-staticity δ_t of the (anti) self-dual lattice calorons for different topological sectors $|Q|$ is shown. In order to guide the eye the first branching point δ_t^* ($1 \rightarrow 2$ lumps) is shown as a dashed line. Here $\delta_t < \delta_t^*$ indicates that at last two dyons are visible in the analytic action density of a $|Q| = 1$ caloron, provided that the holonomy is maximally non-trivial. Static calorons are found for $|Q| = 2, 3, 4$ but not for $|Q| = 1$. The few $|Q| = 1$ configurations with $\delta_t < \delta_t^*$ were not reliably resolved as dissociated calorons, since the distance between lumps of topological charge did not exceed one lattice spacing in every direction. The general behaviour can be made more clear by counting the number of local maxima in the topological charge density of the (anti) self-dual fields, as it is done in the left panel of Fig. 6.3. Of course, only relevant maxima (maxima with a modulus of at least 10% of the global maximum) contribute here. The chance to see constituents is enhanced if a cut $|P_\infty| < 0.2$ is introduced in Fig. 6.3, since the constituents then have comparable masses.

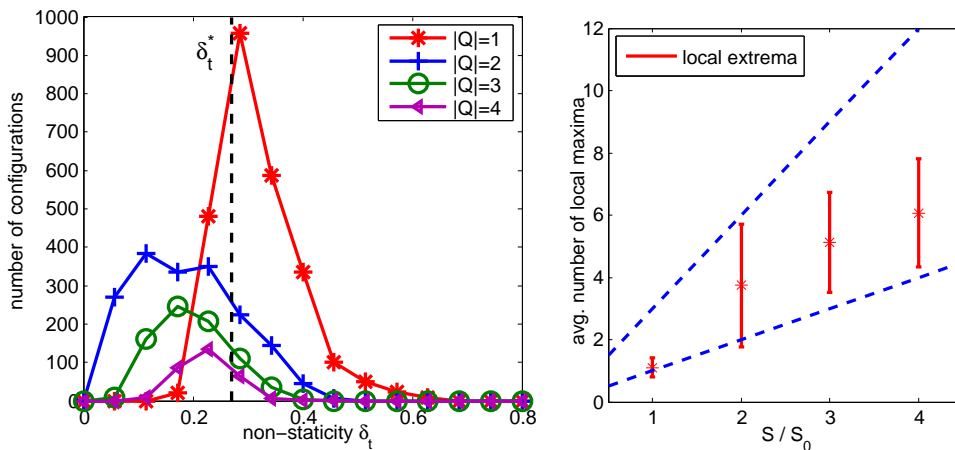


Figure 6.3: distribution of non-staticity for various topological sectors (left) and average number of local maxima for topological sectors (right) with cut $|P_\infty| < 0.2$. **Note:** The bars in the right panel show the standard deviation!

The lower line of in the right figure corresponds to the expectation for trivial caloron with only one peak per unit of $|Q|$ while the steeper curve represents the (extremal) KvBLL case where all $3|Q|$ monopole constituents are visible. Again, there are no signs of dissociated calorons for $|Q| = 1$ visible, but surely for $|Q| > 1$. It needs to be emphasised that this is in agreement with the interpretation in terms of the analytical KvBLL solution. If the constituents are not separated one can still have non-trivial holonomy but the caloron becomes non-static. In this sense the left and the right panel of Fig. 6.3 support this interpretation. For $|Q| > 1$ static calorons are found. A zero-mode analysis for a subset of $\mathcal{O}(100)$ calorons with $|Q| = 1$ and four values of the fermionic boundary condition $\xi = \{0, 1/3, 1/2, 2/3\}$ has shown no signs of zero-mode jumping.

The strategy to produce an ensemble of classical fields with stopping condition (A) has been finally abandoned, since the moduli space for $|Q| = 1$ would be effectively restricted to non-dissociated calorons only.

6.2 Moduli space of lattice calorons

In this section the moduli space for lattice calorons is explored finally in a more complete way and compared to the KvBLL caloron solutions. The comparison focuses on some basic statements that can be made for $SU(3)$ calorons.

1. The caloron with topological charge Q is built from $3|Q|$ constituents.
2. Caloron solutions are characterised by asymptotic holonomy \mathcal{P}_∞ and (3d) positions. If the constituents are separated, the caloron with non-trivial holonomy is static.
3. For different values of the temporal fermionic boundary condition jumping of the zero-mode can be observed.

The previous chapter has made clear that a modified stopping criterion needs to be introduced to make calorons sufficiently (anti) self-dual on one hand and to find static, dissociated calorons on the other hand. For this reason for the remaining part of this chapter the stopping condition (B) will be used. Only fields with $|Q| > 0$ are taken into account. Still restricting ourselves to cooling with Wilson gauge action, gauge fields of various lattice sizes are selected with this stopping condition. The statistics obtained with this method for a number of lattices is shown in Tab. 6.1. Since some configuration do not fulfil condition (B) at any time during cooling, the effective statistics of classical fields is smaller.

lattice size	number of configurations	condition (B) is fulfilled
4×12^3	10000	7840
6×12^3	6000	5627
12^4	1600	1448
4×20^3	≈ 200	–
6×20^3	≈ 100	–

Table 6.1: ensemble of gauge fields generated at $\beta = 5.65$ with Wilson gauge action

Lattice data for 4×20^3 and 6×20^3 have been collected to examine the effect of a larger volume, for the 6×12^3 lattices in order to investigate the effect of a larger aspect ratio N_t/N_s . In case of the symmetric 12^4 lattice the cooled gauge fields are more likely to be interpreted in terms of $O(4)$ -symmetric instantons (on the torus) with various asymptotic holonomies.

After cooling the topological charge is well defined for the improved operator and the deviation of the topological charge from an integer value is generally small. For the 4×12^3 ensemble 67% of the cooled configurations deviate less than 0.01 from an integer value. In Fig. 6.4 the distribution of the topological charge ($Q = 0$ is excluded) and the distribution of the modulus of asymptotic holonomy are shown.

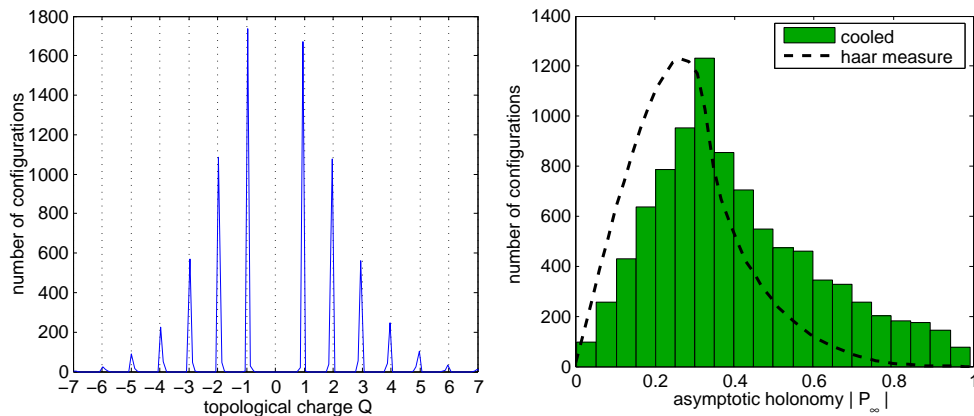


Figure 6.4: topological charge Q_{3li} and the distribution of asymptotic holonomy.

Non-trivial holonomy is still essential to describe the calorons obtained by cooling starting from the confinement phase. The effect of the combined stopping condition (B) is that the statistics is split up into two almost disjoint parts for $|Q| = 1$, and to a smaller extent also for $|Q| = 2$. These parts (a) and (b) (see Fig. 6.5) mainly depend on whether cooling stopped because of (b) a minimal value for δ_F or (a) a minimal value of δ_t respectively. The distribution of the topological charge and the asymptotic holonomy in Fig. 6.4 are qualitatively like the previous ones in Fig. 6.1.

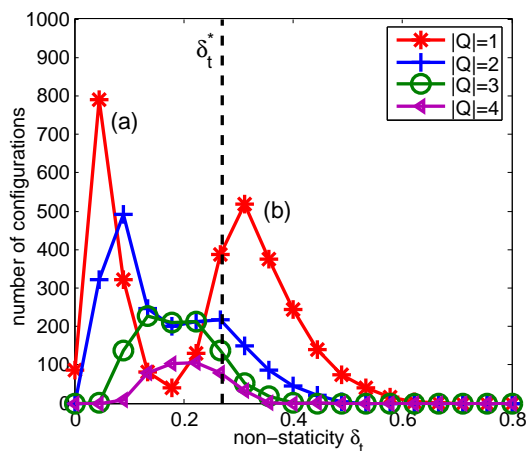


Figure 6.5: distribution of non-stationarity for various topological sectors (left) and the violation of self-duality (right)

The part (b) violates the equation of motion on the lattice less than (a), but only (a) contains static and dissociated calorons. Both parts together could not be obtained by a single stopping condition. For $|Q| = 1$ the combined stopping condition is a compromise between having a field belonging either to the moduli space of the torus, which in the strict sense excludes $|Q| = 1$ calorons with a finite size, or to the moduli space of $S^1 \times \mathbb{R}^3$, where static calorons would dominate according to the assumption the constituent positions are distributed randomly ($d \gg \beta$). Both parts account for the moduli space of approximate caloron solutions on the lattice. This partitioning into part (a) and (b) will be also visible (and marked) in some other figures.

Now we are asking whether all these lattice calorons consist of $3|Q|$ constituents. A robust definition of constituent monopoles was given in the beginning of the last chapter and was already successfully used to identify $3|Q|$ monopoles. Unfortunately this criterion will not work if the gauge fields have trivial holonomy or are not sufficiently smooth. For trivial holonomy $\mathcal{P}_\infty \in Z(3)$ three eigenvalues are degenerated in the asymptotic region and the (massless) monopoles cannot be located on the lattice using this criterion. On the other hand, if the fields are not sufficiently cooled and the field is not yet classical the Polyakov loop is still fuzzy and no signals (e.g. positions) from a single configurations can be obtained. Since the ensemble was cooled until the fields are sufficiently (anti) self-dual the second problem poses no danger. In Fig. 6.6 the results for the number of monopoles, obtained with this definition, for different cuts applied to the asymptotic holonomy $|P_\infty|$ and the non-staticity δ_t are shown. Over-counting constituents in calorons with trivial holonomy would actually pose a problem.

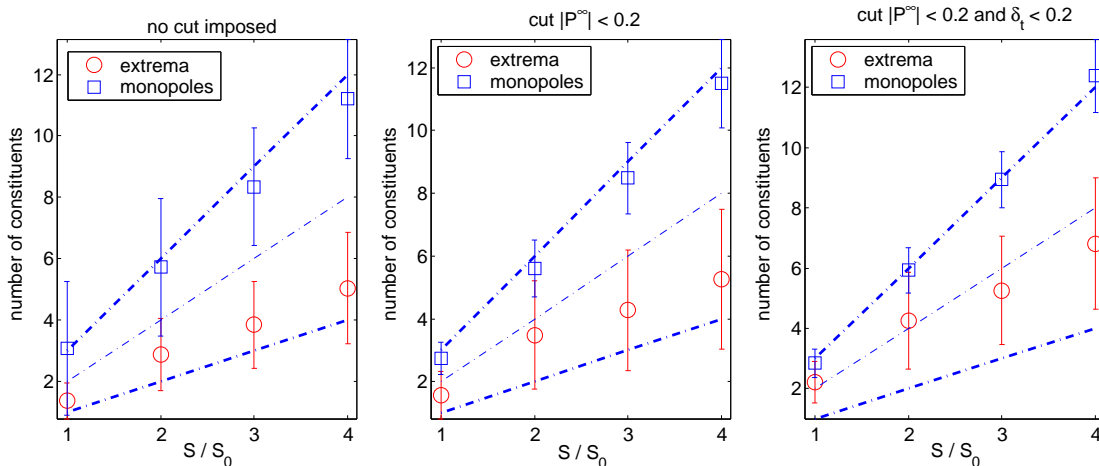


Figure 6.6: number of monopoles through local maxima and Polyakov loop criterion with cuts to $|P_\infty|$ and δ_t . **Note:** The bars show the standard deviation!

Introducing the cut to the holonomy is acting to suppress the case of (nearly) trivial holonomy where the definition of the monopoles will not work. Indeed, if the cut $|P_\infty| < 0.2$ is introduced the standard deviation of the number of monopoles becomes smaller and the result is only compatible with $3|Q|$ constituent monopoles. The latter cut to the non-staticity δ_t is applied, since dissociated calorons are discernible as static ones for non-trivial holonomy and this enhances the the number of local maxima in the action. The gain due to this cut is marginal and the average number of local maxima identified in the topological charge is smaller than $3|Q|$ but systematically larger than $|Q|$. This behaviour is further illustrated by the distribution of the number of monopoles for single topological sectors is shown Fig. 6.6. Again the cut $|P_\infty| < 0.2$ is used to get rid of trivial asymptotic holonomy.

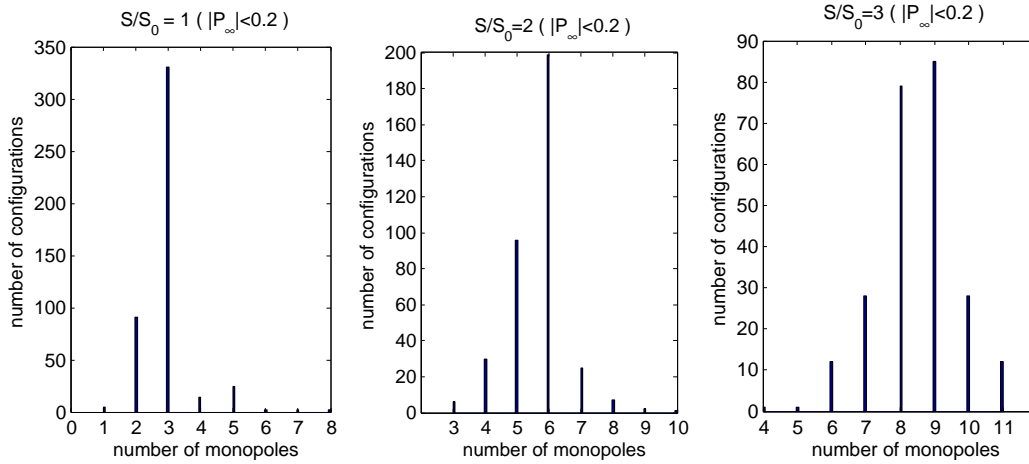


Figure 6.7: distribution of monopole number for $S/S_0 = 1, 2, 3$ with $|P_\infty| < 0.2$

The number of configurations in Fig. 6.7 is dominated by cases with a number of monopoles equal to $3|Q|$. The over-counting can be further suppressed by a more strict cut to the holonomy. From the analytic action form of the density for $|Q| = 1$ it is known that a caloron with separated constituents gives rise to a static action density whereas a non-dissociated caloron is localised in 4 dimensions and hence is not static. In Fig. 6.8 (rhs.) this relation is shown to be realised for the clusters formed in the moduli space obtained by the combined stopping condition (B). If the constituents are separated the caloron is static and if all constituents come close the caloron is time-dependent.

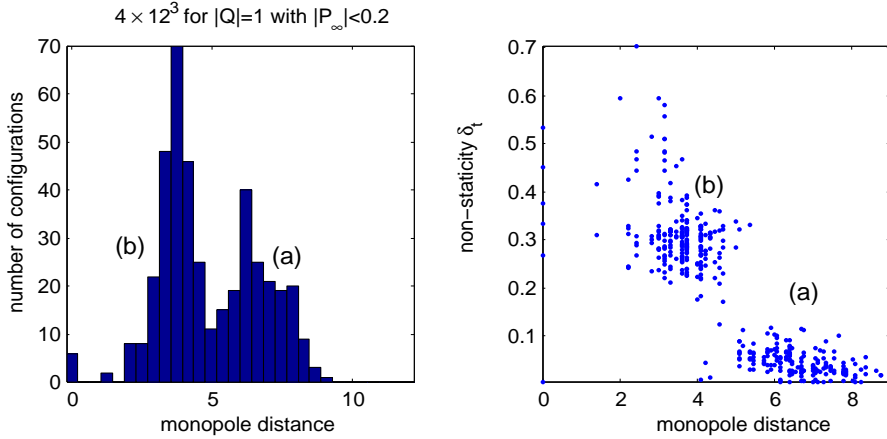


Figure 6.8: distribution of average monopole distance (left) and scatter-plot of non-staticity δ_t versus average monopole distance (right) restricted to $|P_\infty| < 0.2$ and topological charge $|Q| = 1$

For a subsample of 200 configurations with $1 \leq |Q| \leq 4$ the spectrum of the clover-improved Dirac operator was computed. The boundary conditions were taken at the midpoints between the eigenvalues of the asymptotic holonomy $(1 - \xi_n) = (\mu_{n+1} + \mu_n)/2$, where the zero-mode is expected to be maximally localised on the n^{th} constituent. If the n^{th} constituent is massless $\nu_n = 0$, the zero-mode density will

be also delocalised for this ξ_n . The jumping range d_{nm} between the maxima of the zero-mode density for charge 1 and different boundary conditions is computed by

$$d_{nm} = |r(\xi_n) - r(\xi_m)|_{\text{torus}}.$$

The torus distance is the length of the smallest straight line on the flat torus and r is the position of the maximum of $\psi^\dagger\psi$ for the specified boundary condition. The histogram for the jumping range for possible combinations of boundary conditions is shown in Fig. 6.9. To avoid false signals from delocalised modes the jumping range is not shown if $IPR < 2$.

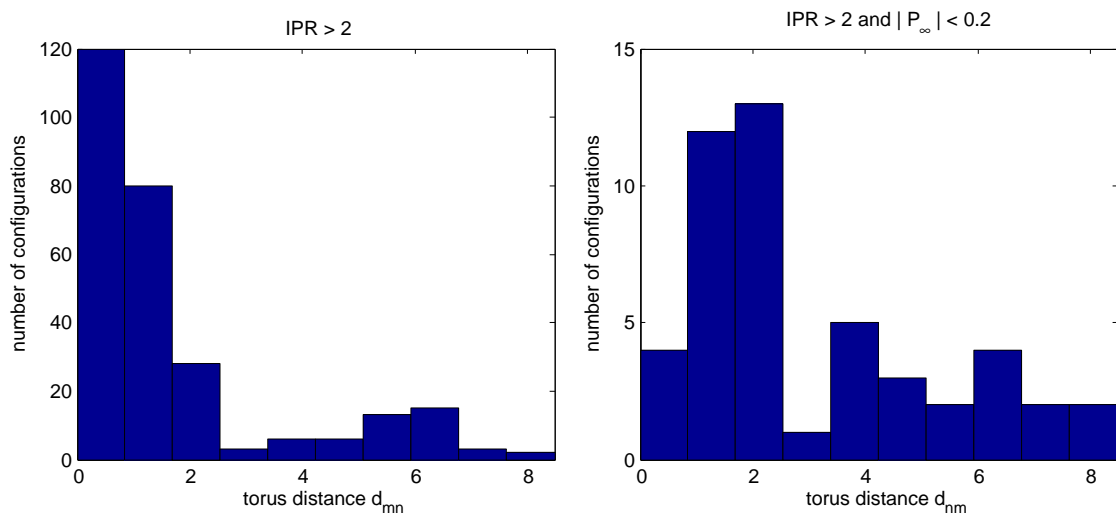


Figure 6.9: distance between maxima of zero-mode density for different b.c. only with $IPR > 2$ (left) and with $IPR > 2$ and $|P_\infty| < 0.2$ (right).

Jumping over large distances (on the torus) is visible. Again the behaviour typical for KvBLL-caloron is enhanced, if a cut with respect to the asymptotic holonomy $|P_\infty| < 0.2$ is imposed.

Within the statistics it is possible to give evidence that lattice caloron configuration for $SU(3)$ consist of $3|Q|$ monopoles. Through the definition of monopoles by coinciding eigenvalues of the Polyakov loop this is even possible for a relatively small volume of 4×12^3 . In order to get rid of false signals from trivial holonomy only configurations with $|P_\infty| < 0.2$ are allowed to contribute. For $|Q| = 1$, and to a smaller extent also for $|Q| = 2$, two nearly separated parts of the moduli space become visible. This supports using the stopping criterion (B) since the accessible part of the caloron moduli space is extended and the typical behaviour of KvBLL calorons becomes visible.

6.3 Dependence on the aspect ratio N_t/N_s

The aspect ratio and the volume together¹ define to which extent the lattice models $S^1 \times \mathbb{R}^3$. For this study the aspect ratio needs to be small and the volume big such that the overlap effect in space can be neglected. If the aspect ratio is sent to one, more instanton-like classical solutions are expected. For $SU(2)$ a 'Recombination² of dyons into calorons' was observed to take place during this limit [29]. In order to study this behaviour the cases $N_t/N_s = 6/12$ and $N_t/N_s = 12/12$ are studied on ensembles which were cooled with the stopping condition (B). The yield of classical configurations is shown in the upper part of Fig. 6.10. Similar to [29] static calorons vanish, if the aspect ratio N_t/N_s is increased (lower part of Fig. 6.10).

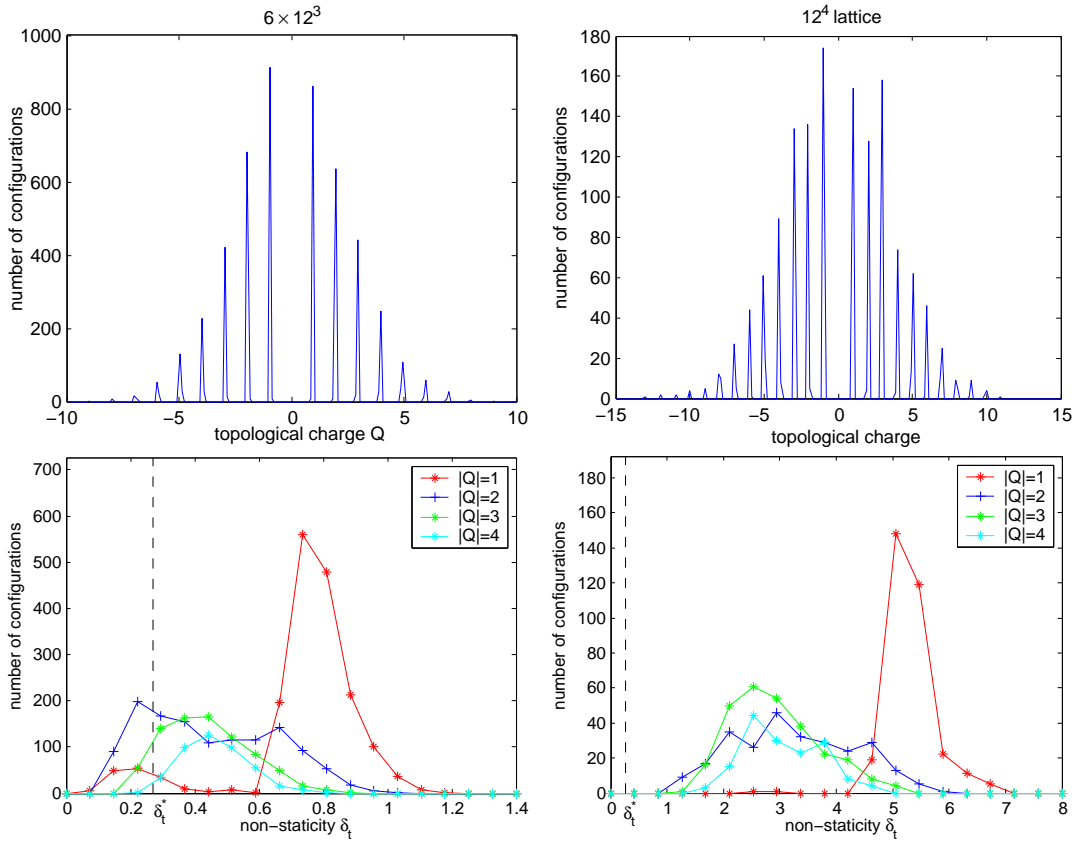


Figure 6.10: distribution of non-staticity and topological charge for 6×12^3 (left) and 12^4 (right) lattice

The distribution of the modulus of the asymptotic holonomy is not much different from Fig. 6.4 for both ensembles, non-trivial holonomy is still important approaching the symmetric torus. In Fig. 6.11 the number of constituents, found for different topological sectors $|Q|$, for $N_t = 6$ is shown. Different cuts with respect to the holonomy $|P_\infty|$ and non-staticity δ_t are applied.

¹**Note:** This also depends on the caloron size.

²dissociated dyonic constituents recombine into one non-dissociated calorons

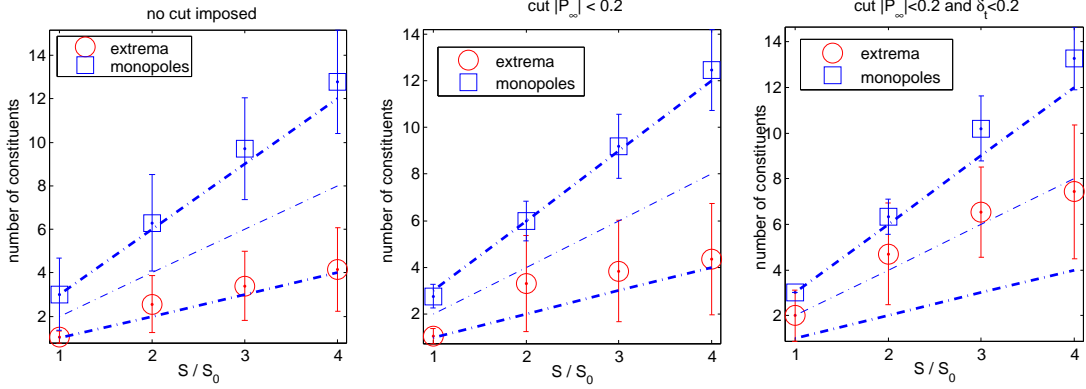


Figure 6.11: Dissociation into constituents from local maxima of action and monopole counting (defined by coinciding eigenvalues) for 6×12^3 lattice with different cuts imposed.

Despite the bigger aspect ratio $3|Q|$ monopoles are found while a lower number of local extrema in the topological charge is observed Fig. 6.11. This has not been checked on the symmetric lattice, since the role of the Polyakov loop in a certain direction is not well-defined in this case.

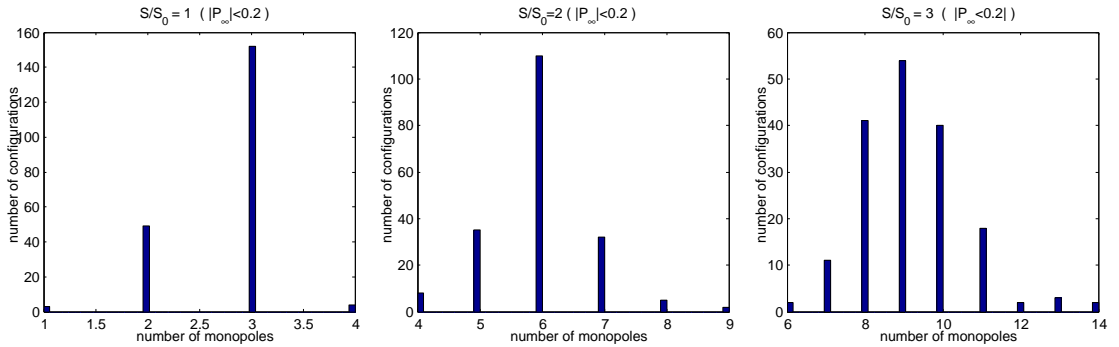


Figure 6.12: Distribution of number of monopoles for different topological (self-dual) sectors. The figures show the results for $|Q| = 1, 2, 3$ (left, middle, right).

Imposing a cut on the asymptotic holonomy makes the definition of the monopoles useful and it can be seen in Fig. 6.12 that mainly $3|Q|$ monopoles are discernible in the (anti) self-dual charge Q sector. A clear signal is observed for $|Q| = 1$ and washed out for higher charges. For $|Q| = 3$ finite volume effects will certainly become important since for $|Q| = 3$ nine constituents need to be packed into the relatively small volume.

The recombination into static non-dissociated calorons is also observed for $SU(3)$ if N_t/N_s is increased Fig. 6.10 but the monopoles can still be observed in the non-trivial substructure of the Polyakov loop.

6.4 Dependence on the volume N_s^3

The main effect in the finite volume is to restrict possible positions and distances of monopole constituents to a finite (periodic) box. Hence the monopole distance in units of the temporal extent r/β cannot become larger than $L/\beta = N_s/N_t$. Increasing the volume N_s^3 with a fixed N_t increases the possible distances in units of β between caloron constituents. Assuming that the distribution of the distances between constituents scales, independent of N_t , with the volume, almost all calorons are static since the distances between constituents become arbitrarily large. Considering gauge fields, cooled with the combined stopping condition (B) and Wilson gauge action, this is illustrated in Fig. 6.13. Due to the small statistics the distribution of topological charges is quite irregular.

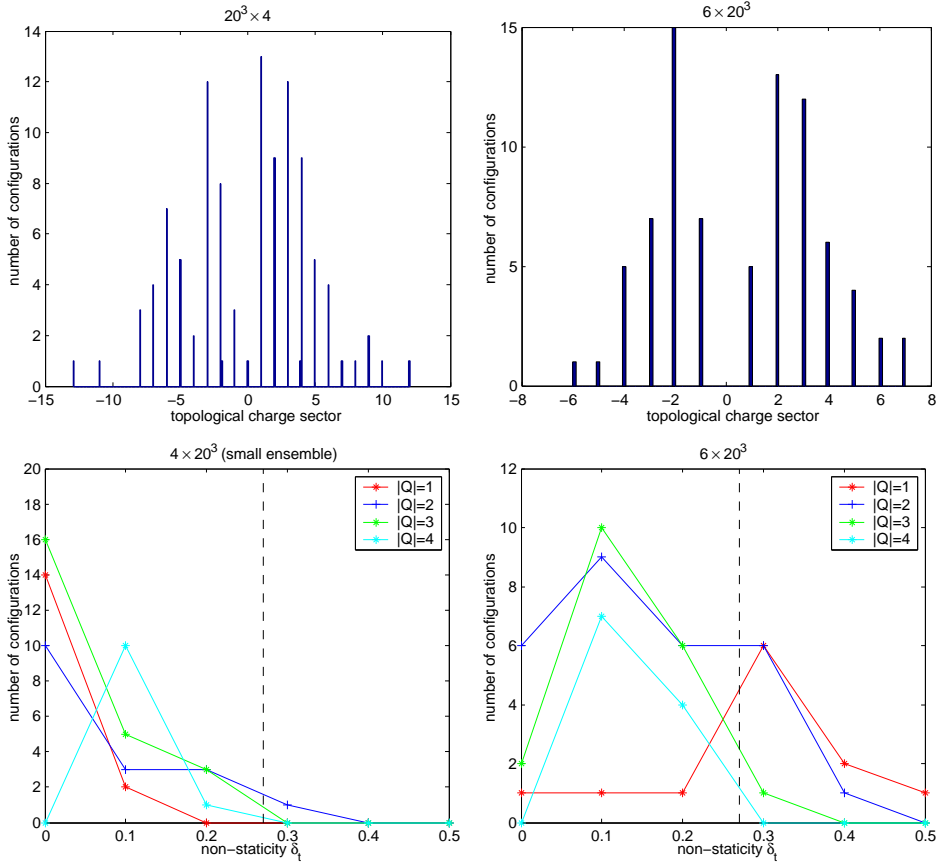


Figure 6.13: Distribution of topological charges (upper panel) and distribution of δ_t for 4×20^3 (left) and 6×20^3 (right)

For the 6×20^3 lattice the aspect ratio is close to the value of the 4×12^3 lattice and the distribution of δ_t already moves away from zero. Especially for the 4×20^3 lattice, where one has significant higher distances and a lower aspect ratio $N_t/N_s = 0.2$, static and dissociated calorons dominate the statistics. Almost all classical configurations of the topological sectors $|Q| = 1 \dots 4$ obtained for this lattice size have a non-staticity which is lower than the bifurcation value $\delta_t^* = 0.27$, shown as the dashed line.

6.5 Non-caloron configurations from cooling

By cooling one can also find non-caloron configurations which are stable with respect to cooling but not (anti) self-dual. They are very stable with respect to cooling and do not satisfy any of our stopping conditions (A) or (B) at any time. Cooling was stopped by fiat after 1000 steps to handle these leftover configurations. Since they have been recorded it is possible to show these fields and their frequency for the $Q = 0$ sector. In Fig. 6.14 the distribution of S/S_0 and the scatter plot of the non-staticity δ_t versus the normalised action S/S_0 is shown.

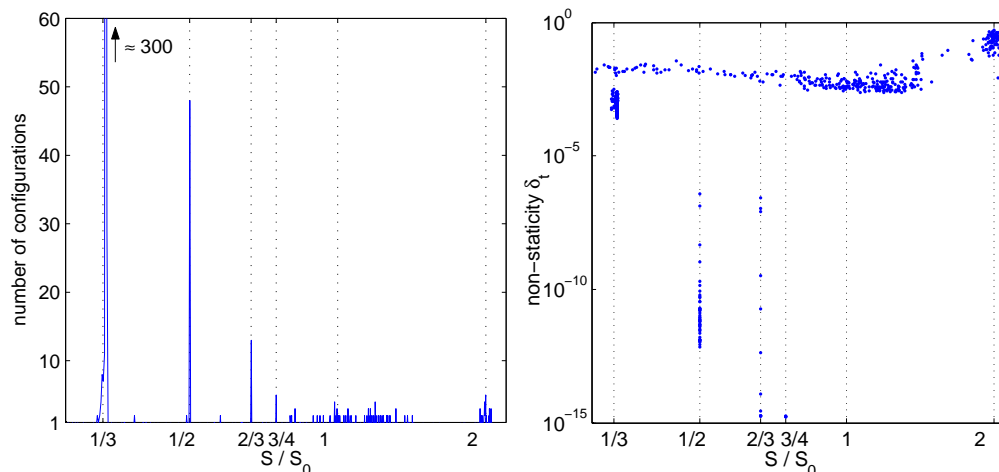


Figure 6.14: action S/S_0 (left) and the scatter plot showing non-staticity δ_t versus S/S_0 for stable fields with $Q=0$ and $N_t/N_s = 4/12$

Gauge fields which have a constant action $S_0 N_t/N_s$ and are stable with respect to cooling were already found in previous cooling studies [75]. These so-called Dirac sheet configurations can be described in terms of Abelian, constant curvature solutions and are well understood [76].

$$F_{\mu\nu} = i \frac{\tau_3}{2} \frac{2\pi n_{\mu\nu}}{l_\mu l_\nu} \quad n_{\mu\nu} \in \mathbb{Z} \text{ and } n_{\mu\nu} = -n_{\nu\mu}. \quad (6.1)$$

Within the 10000 configurations there are 380 configurations ($\approx 4\%$) of that type. They have a constant curvature $F_{\mu\nu}$ (hence $\delta_t \ll 1$ see Fig. 6.14 right panel) are Abelian and have an action $S = S_0 (N_t/N_s \pm 0.01)$. The Dirac sheets with $S/S_0 = 1/3$ are not very static because they were actually expected and intercepted by a special trigger before 1000 steps of cooling were applied to them. The frequency of Dirac sheets agrees qualitatively with [75]. There it was also found that in the limit $N_s \rightarrow \infty$ the measure of these configurations vanishes. Hence they are artifacts of the finite volume. In Fig. 6.14 marginally stable fields with $S = S_0 \{1/2, 2/3, 3/4\}$ are shown. Multiples of $1/3$ are expected for the same aspect ratio but $1/2$ cannot be explained in terms of $SU(2)$ solutions like Eq. 6.1. The yield of $Q = 0$ fields with $S = 2S_0$ is most likely from caloron-anticaloron superpositions and with $S = S_0$ from dyon-antidyon events, which were also observed in the previous $SU(2)$ cooling studies [71]. For $N_t/N_s = 6/12$ stable and static fields with $S = S_0 \{3/8, N_t/N_s, 3/4\}$ are observed with the statistics $\{92, 82, 7\}$ out of the 6000 cooled configurations.

6.6 Summary

This chapter confirms on a statistical basis what was already shown in the last one. At finite temperature and $T < T_{\text{crit}}$ there are lattice solutions of the equation of motion which need to be described in terms of calorons with non-trivial asymptotic holonomy. These calorons can be described in terms of $3|Q|$ monopole positions defined by coinciding eigenvalues for the Polyakov loop operator (Figs. (6.6, 6.7, 6.11 and 6.12)). It is visible in Fig. 6.5 that the calorons are static if the constituents are separated and not static if they are close to each other. Preliminary results presented in Fig. 6.9 confirm that zero-mode jumping takes place. This was already observed for selected classical configurations in the last chapter. If the temperature is lowered the dissociated calorons recombine into single (anti) self-dual and non-static lumps but can be embedded in a non-trivial holonomy and thus possess a non-trivial substructure in the Polyakov loop. A larger volume makes static and dissociated calorons more probable and enhances the KvBLL pattern.

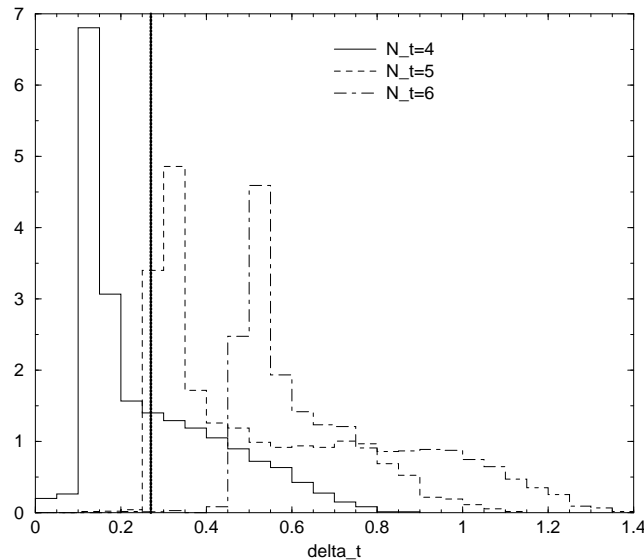


Figure 6.15: results from the $SU(2)$ cooling study [29] on $N_t \times 16^3$ lattices for $|Q| = 1$.

The results (e.g. Fig. 6.10) for the different aspect ratios N_t/N_s qualitatively agree with the former results for $SU(2)$, shown in Fig. 6.15, but can hardly be compared quantitatively. The result of cooling also strongly depends on the cooling method and especially also depends on the stopping condition. Additionally non-caloron fields, which were already observed in case of $SU(2)$ are also found here and give rise to new constant curvature fields within $SU(3)$.

Chapter 7

Summary and Outlook

7.1 Summary

With the goal to prepare for an understanding of the non-perturbative vacuum structure of QCD, the quantum mechanical kink-gas was introduced and compared with a numerical evaluation of the path-integral. The applicability of the saddle point method was numerically studied by inspecting the Hessian operator during a series of smoothing steps, limited by the requirement that the expectation value of an interesting observable is not biased by smoothing. For the weak coupling case this was successfully verified for the energy gap. In case of strong coupling, where classical solutions can only be washed out by numerous cooling steps, the energy gap was biased.

In the case of $SU(3)$ Yang-Mills theory we focused on classical solutions at finite temperature with non-trivial holonomy. These so-called KvBLL calorons might, incorporated in a semiclassical approximation, provide a microscopic mechanism for the deconfinement-confinement phase transition. It was interesting to perform this numerical study since $SU(3)$ calorons are qualitatively different from calorons with trivial holonomy or from $SU(2)$ embeddings, which appear as certain limiting cases of the KvBLL solution. Previous investigations of the semiclassical structure already dealt with $SU(2)$ [29] but some technical improvements were necessary to proceed to $SU(3)$. For example an improved definition of the field strength, the clover-improved Dirac operator and an over-improved action were used. These improvements were necessary to study higher topological sectors more reliable and to circumvent the instability of classical solutions due to lattice artifacts and topological restrictions. In order to obtain a caloron solution we cooled gauge fields starting from a Monte-Carlo ensemble generated in the confined phase, close to the deconfinement phase transition. Examining these classical configurations we found that non-trivial holonomy is the generic case. All configurations we found resemble the analytical KvBLL caloron, despite the fact that the analytic solution exists in an infinite volume. Typical properties are that (i) a caloron of charge Q consists of $3|Q|$ constituents, (ii) non-dissociated calorons show a substructure in the Polyakov loop profile and are non-static, (iii) dissociated calorons are static and the zero-mode is localised on a monopole constituent, depending on the fermionic boundary condition. The dependence on the boundary condition is determined by the holonomy. These

findings were reproduced consistently by measuring the Polyakov loop, the topological charge density and the spectrum of the Dirac operator for certain values of the boundary condition. Generally the asymptotic holonomy is a well-defined quantity even on a finite lattice. Having found this on selected examples, these features were also reproduced for a large number of cooled fields. Due to lattice artifacts of the gauge action and stability problems on the torus one could miss the KvBLL caloron signature for $|Q| = 1$. We have overcome this by a combined stopping condition, that accepts also static solution even if not perfectly self-dual. Effectively cooling stops earlier. Although the solutions are much more complicated for higher charges [54] we were able to characterise them using the same techniques.

A recombination into non-dissociated calorons takes place if the aspect ratio N_t/N_s is increased towards the symmetric lattice while the KvBLL pattern becomes more pronounced, if the aspect ratio is lowered. Non-trivial holonomy stays important as long as cooling starts from the confined phase.

7.2 Conclusions

We conclude that classical solutions with non-trivial holonomy and the typical behaviour known from KvBLL caloron solutions exist on asymmetric lattices with suitable aspect ratio. In the spirit of these findings, previous numerical and analytical studies which describe the semiclassical structure at finite temperature only in terms of instantons or calorons with trivial holonomy, need a reinterpretation. The temperature range near T_{crit} can be understood only with the 'new' caloron. There, the $SU(3)$ KvBLL calorons should be the building blocks of a semiclassical calculation, where the statistical mechanics of constituents at a given temperature determines the holonomy.

7.3 Outlook

Future work on this subject has two aspects. First one needs to develop further the knowledge of classical solutions, also for higher charges and for the interesting case of $SU(3)$ gauge theory. The present work is only the first step in this direction. Investigations on the lattice have the potential to accompany this development on the analytic side and to give hints for the general composition of the moduli space [77]. The second aspect, which has to be studied numerically, is to search for corresponding signatures in equilibrium Monte-Carlo configurations. Current investigations on APE-smearred configurations already deal with the interpretation of low-lying fermion modes [25, 26]. It remains to be seen whether a model of the QCD vacuum based on calorons with non-trivial holonomy provides a viable microscopic mechanism for confinement, at least at finite temperature.

Appendix A

Projection to $SU(N)$

A.1 General remarks

The essential part of a smearing or cooling procedure is the 'projection' onto the gauge group $SU(N)$. A possible mapping $\mathbf{P}_{SU(N)} : M(n, \mathbb{C}) \mapsto SU(N)$, where generally $SU(N) \subset M(N, \mathbb{C})$ is identical mapped to itself, is defined by the requirement

$$\mathbf{P}_{SU(N)}(M) = \{U \in SU(N) : \text{Re tr}(UM^\dagger) = \text{maximal}\}. \quad (\text{A.1})$$

This procedure is called the *MaxReTr* projection. By replacing a link variable $U_{x,\mu}$ by $\mathbf{P}_{SU(N)}(M)$ the local action $\text{Re tr}(\mathbb{1} - U_{x,\mu}M^\dagger)$ is minimised. The existence of a matrix U in Eq. A.1 is obvious since $SU(N)$ is compact but there are cases where this construction and the requirement are not unique (e.g. $M = \mathbb{0}$). However, such a case was never encountered in the simulation with random matrices. The construction of $\mathbf{P}_{SU(N)}(M)$ is described in Sect. A.3. Another possibility to project to $SU(N)$ is the so called *UnitCircle* formula

$$\mathbf{P}'_{SU(N)}(M) = \frac{M\phi}{\sqrt{M^\dagger M}}, \quad (\text{A.2})$$

where the phase ϕ renders this unitary matrix special unitary. This construction makes only sense if M has non-zero eigenvalues. An important observation is that these methods are not equivalent. Both projections 'respect gauge invariance' which means that for the following diagram commutes.

$$\begin{array}{ccc} M & \xrightarrow{\mathbf{P}_{SU(N)}} & U \\ \Omega \downarrow & & \downarrow \Omega \\ M' & \xrightarrow{\mathbf{P}_{SU(N)}} & U' \end{array}$$

For the ReTrMax projection this only holds numerical if convergence was reached with respect to the numerical precision. The generalised staples M , independent of a specific lattice action, transform as $M \rightarrow M' = \Omega(x)M\Omega(x+\mu)^\dagger$ under gauge transformations $\Omega(x)$. From the the observation that $\text{Re tr}(UM^\dagger) \equiv \text{Re tr}(U'(M')^\dagger)$ and the uniqueness property of \mathbf{P} (which was not proven here) one concludes that

$$\mathbf{P}_{SU(N)}(M') = U' = \Omega(x)\mathbf{P}_{SU(N)}(M)\Omega(x+\mu)^\dagger. \quad (\text{A.3})$$

Two gauge fields remain gauge-equivalent after projection and are in both cases connected by the same gauge transformation. In this sense Eq. A.3 is equivalent to the property that the diagram is commutative. In Tab. A.1 these projection and the naive method, which projects back by orthonormalising the row vectors, are compared for $SU(3)$. As a test of numerical stability one random gauge field on a 4×12^3 lattice is cooled by the APE-smearing method using these three projection methods. For each method the average plaquette after a number of APE blocking steps is shown. As a test, whether projection and gauge transformation are compatible, a parallel history for a random gauge copy is included.

MaxReTr projection		
steps	original gauge field	gauge copy
0	-0.000796934548055	-0.000796934548055
1	0.249483394417475	0.249483394417475
2	0.419962269229319	0.419962269229319
3	0.524804733451640	0.524804733451640
4	0.597637923168918	0.597637923168917
5	0.653131016265543	0.653131016265544
UnitCircle projection		
steps	original gauge field	gauge copy
0	-0.000796934548055	-0.000796934548055
1	0.246866166968911	0.246866166968911
2	0.417470795318875	0.417470795318875
3	0.522740823515202	0.522740823515202
4	0.595853938998313	0.595853938998313
5	0.651568409397263	0.651568409397263
projection by orthonormalisation		
steps	original gauge field	gauge copy
0	-0.000796934548055	-0.000796934548055
1	0.232618217274054	0.233145269931380
2	0.388669863129825	0.389271969451491
3	0.491558739476750	0.492009565989056
4	0.565775939195666	0.566232968210528
5	0.623338491956017	0.623966176858063

Table A.1: Comparison of average plaquette after a number of APE-blocking steps for different projection methods for $SU(3)$

By definition only the *MaxReTr* projection Eq. A.1 gives the maximum of $\text{Re tr}(UM^\dagger)$ but due to the absence of an explicit formula only the *UnitCircle* projection Eq. A.2 is differentiable and can be used e.g. for a HMC algorithm [78]. Both methods evidently respect gauge invariance up to the numerical precision as shown by the highlighted bold letters in Tab. A.1 for the plaquette measurements. The naive projection by orthonormalising should only be used if the matrix M is either 'close' to $SU(N)$ or when the projection does not need to preserve the gauge. In these cases naive orthonormalisation is preferred because its considerably faster than the other methods. If the matrix M is 'close' to $SU(N)$ UnitCircle and naive projection of M

clearly tend to be 'close' to the ReTrMax projection.

A.2 Projection to $SU(2)$

To complete the comments to the projection the ReTrMax projection for $SU(2)$ needs to be specified. This is a mapping

$$\mathbf{P}_{SU(2)} : M = \begin{pmatrix} m_{11} & m_{12} \\ m_{21} & m_{22} \end{pmatrix} \rightarrow U \in SU(2)$$

with $M \in GL(n, \mathbb{C})$. If one uses the parametrisation $U = a_0 \mathbb{1} + i \vec{a} \vec{\sigma}$ the matrix is special unitary if the $a_0 \in \mathbb{R}$, $\vec{a} \in \mathbb{R}^3$ and the condition $a_0^2 + \vec{a}^2 = 1$ is fulfilled. The projection condition $\max \text{Re tr}(UM^\dagger)$ in this parametrisation reads

$$\begin{aligned} & a_0 \text{Re}(m_{11}^* + m_{22}^*) + a_1 \text{Re}(i(m_{12}^* + m_{21}^*)) \\ & + a_2 \text{Re}(m_{12}^* - m_{21}^*) + a_3 \text{Re}(i(m_{11}^* - m_{22}^*)) = \text{maximal}, \end{aligned}$$

which looks like the scalar product of two 4 dimensional vectors. Since a is restricted to lie on a 3 sphere, the product is maximised if a is parallel aligned to the other vector and normalised. Using $a = m_{11} + m_{22}^*$, $b = m_{12} - m_{21}^*$ and $c = 1/\sqrt{|a|^2 + |b|^2}$ this gives the final expression

$$\mathbf{P}_{SU(2)}(M) = c \begin{pmatrix} a & b \\ -b^* & a^* \end{pmatrix} \in SU(2). \quad (\text{A.4})$$

The class of matrixes for which this works is not specified here but during numerical work no problems with singular matrices occurred. If M is a sum of $SU(2)$ matrices, what is clearly not the general case, the projection can simply be accomplished by dividing through the square root of the determinant

$$\mathbf{P}_{SU(2)}(M \propto SU(2)) = \frac{1}{\sqrt{\det M}} M \in SU(2). \quad (\text{A.5})$$

A.3 Iterative projection to $SU(N)$

The iterative procedure of the projection of an complex $N \times N$ matrix M is described in terms of the projection to $SU(2)$ á la Cabbibo-Marinari [67].

1. Choose a (preconditioned) matrix U_0 to start with and set $k = 0$.
2. Select an 2×2 block m of $M \cdot U_k$ and project to $SU(2)$ $w_k = \mathbf{P}_{SU(2)}(m)$
3. Define $U_{k+1} := U_k \cdot w_k$ where W_k only acts on the chosen subgroup.
4. For numerical stability U_{k+1} should be normalised¹ back to $SU(3)$.
5. Set $k \rightarrow k + 1$ and go to 2 until numerical convergence in *all* subgroups.
6. Finally $\mathbf{P}_{SU(N)}(M) := U_{k+1}$.

¹Here it is sufficient to use orthonormalisation of the row vectors.

Appendix B

Testing the Dirac operator

For the $|Q| = 2$ caloron with trivial holonomy, that was shown as an example, the spectrum is shown more explicitly. Since this field was generated in $SU(2)$, one has to distinguish the properties of the $SU(2)$ field and the embedding into $SU(3)$. From this example one can judge to what extent the operator is improved and how the spectrum looks like on a cooled gauge field. On the other hand the index theorem is non-trivially fulfilled for the $SU(3)$ embedding. This might be of general interest. In Fig. B.1 some properties of 80 low lying eigenmodes.

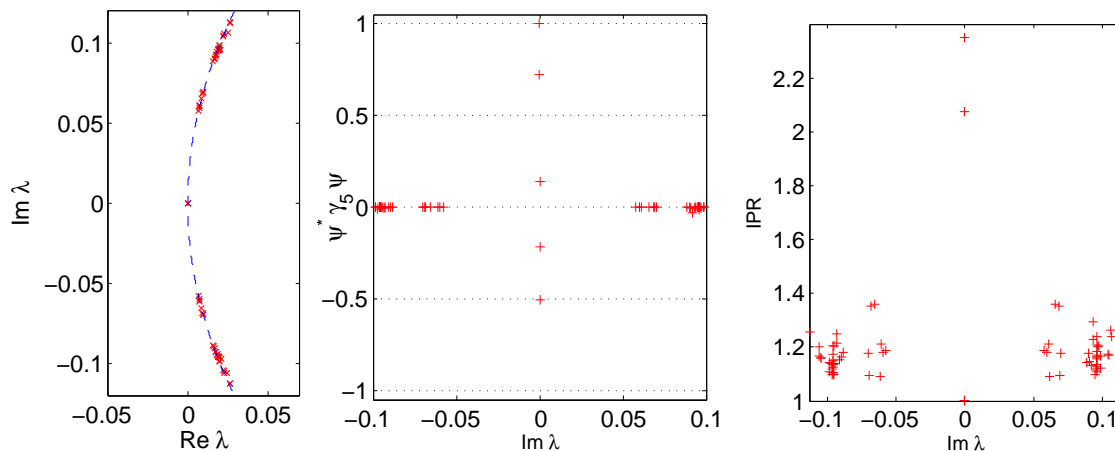


Figure B.1: low lying spectrum of the clover improved Dirac operator with symmetric b.c. for the $Q = 2$ caloron with trivial holonomy (embedded solution); the real and imaginary part of eigenvalues (left); γ_5 matrix element (middle) and inverse participation ratio (right) versus the imaginary part of λ

Two of six zero-modes have definite chirality +1 while the others have not. The trace of γ_5 in the kernel of \mathcal{D} gives $\text{tr}(\gamma_5[U])_{\text{zm}} = 2.03$. Diagonalising the overlap-matrix $M_{ij} = \int d^4x \psi_i \gamma_5 \psi_j$ for $i, j \in \text{kernel } \mathcal{D}$ gives the expected result

$$O^\dagger M O = \text{diag}(-1.02, -0.97, +1.03, +0.99, +1.00, +1.00).$$

Up to numerical errors, which are caused by violation of chiral symmetry of the operator, one has $n_+ = 4$ and $n_- = 2$. The original gauge field in $SU(2)$, however, has only 2 zeromodes with $n_+ = 2$.

Acknowledgements

I want to express my great gratitude to Michael Müller-Preussker for both giving me such an interesting topic for a diploma thesis and for making it possible to experience such a warm atmosphere in his research group. I benefit from his experience, explanations and the many discussions we had.

Special thanks also to Michael Ilgenfritz. I appreciate our good collaboration and the enlightening comments he made.

Many thanks also to André Sternbeck, Stanislav Shcheredin, Jan Volkholz and Peter Schemel. They made very helpful comments to physics, programming, typesetting and so on. Their experience and many discussions helped a lot.

I also like to thank all other people of our group. They all created this kind and nice atmosphere. Working here is a real pleasure!

Furthermore I thank Christof Gattringer (Univ. Regensburg), Falk Bruckmann and Pierre van Baal (Univ. Leiden) for some very useful discussions and correspondence on the topic and for sharing their experience with me.

Finally many thanks to Maria Landgraf. Her support and endless love made this work a walk-over.

Bibliography

- [1] Steven Weinberg. *Nonabelian gauge theories of the strong interactions*. Phys. Rev. Lett. 31, 494–497 (1973).
- [2] D. J. Gross and Frank Wilczek. *Ultraviolet behavior of non-abelian gauge theories*. Phys. Rev. Lett. 30, 1343–1346 (1973).
- [3] H. Fritzsch, Murray Gell-Mann, and H. Leutwyler. *Advantages of the color octet gluon picture*. Phys. Lett. B47, 365–368 (1973).
- [4] Murray Gell-Mann. *A Schematic model of baryons and mesons*. Phys. Lett. 8, 214–215 (1964).
- [5] J. D. Bjorken and Emmanuel A. Paschos. *Inelastic electron proton and gamma proton scattering, and the structure of the nucleon*. Phys. Rev. 185, 1975–1982 (1969).
- [6] Edward V. Shuryak. *The role of instantons in quantum chromodynamics 1. physical vacuum*. Nucl. Phys. B203, 93 (1982).
- [7] Jr. Callan, Curtis G., Roger F. Dashen, and David J. Gross. *Toward a theory of the strong interactions*. Phys. Rev. D17, 2717 (1978).
- [8] Ernst-Michael Ilgenfritz and M. Müller-Preussker. *Statistical mechanics of the interacting Yang-Mills instanton gas*. Nucl. Phys. B184, 443 (1981).
- [9] Gernot Munster. *On the statistical mechanics of dense instanton gases*. Zeit. Phys. C12, 43 (1982).
- [10] Dmitri Diakonov and V. Yu. Petrov. *Instanton bases vacuum from Feynman variational principle*. Nucl. Phys. B245, 259 (1984).
- [11] A. A. Belavin, Alexander M. Polyakov, A. S. Shvarts, and Yu. S. Tyupkin. *Pseudoparticle solutions of the Yang-Mills equations*. Phys. Lett. B59, 85–87 (1975).
- [12] Gerard 't Hooft. *Symmetry breaking through Bell-Jackiw anomalies*. Phys. Rev. Lett. 37, 8–11 (1976).
- [13] Tom Banks and A. Casher. *Chiral symmetry breaking in confining theories*. Nucl. Phys. B169, 103 (1980).
- [14] Yoichiro Nambu. *Strings, monopoles, and gauge fields*. Phys. Rev. D10, 4262 (1974).

- [15] D. Chen, R. C. Brower, J. W. Negele, and Edward V. Shuryak. *Heavy quark potential in the instanton liquid model*. Nucl. Phys. Proc. Suppl. 73, 512–514 (1999), [hep-lat/9809091](#).
- [16] Tamas G. Kovacs. *Instantons and chiral symmetry on the lattice*. Phys. Rev. D62, 034502 (2000), [hep-lat/9912021](#).
- [17] J.W. Negele, F. Lenz, and M. Thies. *Confinement from Instantons or Merons*. (2004). The XXII International Symposium on Lattice Field Theory.
- [18] Barry J. Harrington and Harvey K. Shepard. *Periodic Euclidean solutions and the finite temperature Yang-Mills gas*. Phys. Rev. D17, 2122 (1978).
- [19] David J. Gross, Robert D. Pisarski, and Laurence G. Yaffe. *QCD and instantons at finite temperature*. Rev. Mod. Phys. 53, 43 (1981).
- [20] Thomas C. Kraan and Pierre van Baal. *Periodic instantons with non-trivial holonomy*. Nucl. Phys. B533, 627–659 (1998), [hep-th/9805168](#).
- [21] Ki-Myeong Lee and Chang-hai Lu. *SU(2) calorons and magnetic monopoles*. Phys. Rev. D58, 025011 (1998), [hep-th/9802108](#).
- [22] Dmitri Diakonov, Nikolay Gromov, Victor Petrov, and Sergey Slizovskiy. *Quantum weights of dyons and of instantons with non-trivial holonomy*. (2004), [hep-th/0404042](#).
- [23] Dmitri Diakonov. *Quantum weights of monopoles and calorons with non-trivial holonomy*. (2004), [hep-ph/0407353](#).
- [24] Falk Bruckmann, Daniel Negradi, and Pierre van Baal. *Higher charge calorons with non-trivial holonomy*. (2004), [hep-th/0404210](#).
- [25] Christof Gattringer and Rainer Pullirsch. *Topological lumps and Dirac zero modes in SU(3) lattice gauge theory on the torus*. Phys. Rev. D69, 094510 (2004), [hep-lat/0402008](#).
- [26] Christof Gattringer et al. *Searching for KvBLL calorons in SU(3) lattice gauge field ensembles*. Nucl. Phys. Proc. Suppl. 129, 653–658 (2004), [hep-lat/0309106](#).
- [27] Margarita Garcia Perez, Antonio Gonzalez-Arroyo, Jeroen Snippe, and Pierre van Baal. *Instantons from over - improved cooling*. Nucl. Phys. B413, 535–552 (1994), [hep-lat/9309009](#).
- [28] Ernst-Michael Ilgenfritz, M. L. Laursen, G. Schierholz, M. Müller-Preussker, and H. Schiller. *First evidence for the existence of instantons in the quantized SU(2) lattice vacuum*. Nucl. Phys. B268, 693 (1986).
- [29] E. M. Ilgenfritz, B. V. Martemyanov, M. Müller-Preussker, and A. I. Veselov. *Recombination of dyons into calorons in SU(2) lattice fields at low temperatures*. (2004), [hep-lat/0402010](#).
- [30] Ernst-Michael Ilgenfritz, B. V. Martemyanov, M. Müller-Preussker, S. Shcheredin, and A. I. Veselov. *On the topological content of SU(2) gauge fields below T(c)*. Phys. Rev. D66, 074503 (2002), [hep-lat/0206004](#).

-
- [31] M. Creutz and B. Freedman. *A statistical approach to quantum mechanics*. Ann. Phys. 132, 427.
- [32] Su-zhou Huang. *When is a semiclassical approximation self-consistent?* Phys. Rev. D54, 5280–5289 (1996), [hep-ph/9605461](#).
- [33] R. P. Feynman. *Space-Time Approach to Non-Relativistic Quantum Mechanics*. Rev.Mod.Phys. 20, 367.
- [34] Sidney R. Coleman. *The uses of instantons*. (1977). Lecture delivered at 1977 Int. School of Subnuclear Physics, Erice, Italy, Jul 23-Aug 10, 1977.
- [35] B. Bunk and Ulli Wolff. *Computer simulation of topological effects in lattice theories: A model study*. Nucl. Phys. B215, 495 (1983).
- [36] Ulrich D. Jentschura and Jean Zinn-Justin. *Instantons in quantum mechanics and resurgent expansions*. (2004), [hep-ph/0405279](#).
- [37] Thomas Schafer and Edward V. Shuryak. *Instantons in QCD*. Rev. Mod. Phys. 70, 323–426 (1998), [hep-ph/9610451](#).
- [38] J. Casahooran. Generalized zeta functions and SUSY QM. In *Proceedings of the Wigner Centennial Conference*, 2004. Proceedings of the Wigner Centennial Conference.
- [39] Jean-Loup Gervais and B. Sakita. *Extended particles in quantum field theories*. Phys. Rev. D11, 2943 (1975).
- [40] Hagen Kleinert. *Path integrals in quantum mechanics, statistics and polymer physics*. World Scientific.
- [41] S. Bilson-Thompson, F. D. R. Bonnet, D. B. Leinweber, and Anthony G. Williams. *Cooling for instantons and the wrath of Nahm*. Nucl. Phys. Proc. Suppl. 109A, 116–120 (2002), [hep-lat/0112034](#).
- [42] Frederic D. R. Bonnet, Derek B. Leinweber, Anthony G. Williams, and James M. Zanotti. *Improved smoothing algorithms for lattice gauge theory*. Phys. Rev. D65, 114510 (2002), [hep-lat/0106023](#).
- [43] Colin Morningstar and Mike J. Peardon. *Analytic smearing of SU(3) link variables in lattice QCD*. Phys. Rev. D69, 054501 (2004), [hep-lat/0311018](#).
- [44] R. S. Ward. *Symmetric calorons*. Phys. Lett. B582, 203–210 (2004), [hep-th/0312180](#).
- [45] M. F. Atiyah and I. M. Singer. *The Index of elliptic operators. 1*. Annals Math. 87, 484–530 (1968).
- [46] Gerard 't Hooft. *Computation of the quantum effects due to a four- dimensional pseudoparticle*. Phys. Rev. D14, 3432–3450 (1976).
- [47] M. F. Atiyah, N. J. Hitchin, V. G. Drinfeld, and Yu. I. Manin. *Construction of instantons*. Phys. Lett. A65, 185–187 (1978).
- [48] Falk Bruckmann, Daniel Nogradi, and Pierre van Baal. *Instantons and constituent monopoles*. Acta Phys. Polon. B34, 5717–5750 (2003), [hep-th/0309008](#).

- [49] Claude W. Bernard, Norman H. Christ, Alan H. Guth, and Erick J. Weinberg. *Pseudoparticle parameters for arbitrary gauge groups*. Phys. Rev. D16, 2967 (1977).
- [50] R. Jackiw and C. Rebbi. *Degrees of freedom in pseudoparticle systems*. Phys. Lett. B67, 189 (1977).
- [51] Pierre Van Baal. *Abelian projected monopoles: To be or not to be*. Nucl. Phys. Proc. Suppl. 106, 586–588 (2002), [hep-lat/0108027](#).
- [52] Pierre van Baal. *Instantons versus monopoles*. (1999), [hep-th/9912035](#).
- [53] M. N. Chernodub, Thomas C. Kraan, and Pierre van Baal. *Exact fermion zero-mode for the new calorons*. Nucl. Phys. Proc. Suppl. 83, 556–558 (2000), [hep-lat/9907001](#).
- [54] Falk Bruckmann and Pierre van Baal. *Multi-caloron solutions*. Nucl. Phys. B645, 105–133 (2002), [hep-th/0209010](#).
- [55] Peter J. Braam and Pierre van Baal. *Nahm’s transformation for instantons*. Commun. Math. Phys. 122, 267 (1989).
- [56] Tom M. W. Nye. *The geometry of calorons*. (2001), [hep-th/0311215](#).
- [57] Philippe de Forcrand and Seyong Kim. *Topological susceptibility and Instanton size distribution from over-improved cooling*. Nucl. Phys. Proc. Suppl. 47, 278–281 (1996), [hep-lat/9509081](#).
- [58] Douglas A. Smith and Michael J. Teper. *Topological structure of the $SU(3)$ vacuum*. Phys. Rev. D58, 014505 (1998), [hep-lat/9801008](#).
- [59] Anna Hasenfratz. *Spatial correlation of the topological charge in pure $SU(3)$ gauge theory and in QCD*. Phys. Lett. B476, 188–192 (2000), [hep-lat/9912053](#).
- [60] Nathan Weiss. *The effective potential for the order parameter of gauge theories at finite temperature*. Phys. Rev. D24, 475 (1981).
- [61] Dmitri Diakonov and Michaela Oswald. *Covariant derivative expansion of Yang-Mills effective action at high temperatures*. Phys. Rev. D68, 025012 (2003), [hep-ph/0303129](#).
- [62] B. Alles, M. D’Elia, and A. Di Giacomo. *Topological susceptibility at zero and finite T in $SU(3)$ Yang-Mills theory*. Nucl. Phys. B494, 281–292 (1997), [hep-lat/9605013](#).
- [63] Dmitri Diakonov. *Instantons at work*. Prog. Part. Nucl. Phys. 51, 173–222 (2003), [hep-ph/0212026](#).
- [64] Kenneth G. Wilson. *Confinement of quarks*. Phys. Rev. D10, 2445–2459 (1974).
- [65] K. Fabricius and O. Haan. *Heat bath method for the twisted Eguchi-Kawai model*. Phys. Lett. B143, 459 (1984).
- [66] A. D. Kennedy and B. J. Pendleton. *Improved heat bath method for Monte Carlo calculations in lattice gauge theories*. Phys. Lett. B156, 393–399 (1985).

-
- [67] N. Cabibbo and E. Marinari. *A new method for updating $SU(N)$ matrices in computer simulations of gauge theories*. Phys. Lett. B119, 387–390 (1982).
- [68] G. Boyd et al. *Thermodynamics of $SU(3)$ Lattice Gauge Theory*. Nucl. Phys. B469, 419–444 (1996), [hep-lat/9602007](#).
- [69] G. Peter Lepage. *Redesigning lattice QCD*. (1996), [hep-lat/9607076](#).
- [70] ARPACK code package. see <http://www.caam.rice.edu/software/ARPACK/>.
- [71] E. M. Ilgenfritz, B. V. Martemyanov, M. Müller-Preussker, S. Shcheredin, and A. I. Veselov. *Evidence for dyonic structure of $SU(2)$ lattice gauge fields below $T(c)$* . (2003), [hep-lat/0301008](#).
- [72] B. V. Martemyanov. private communication.
- [73] Pierre van Baal. private communication.
- [74] Falk Bruckmann, E. M. Ilgenfritz, B. V. Martemyanov, and Pierre van Baal. *Probing for instanton quarks with epsilon-cooling*. (2004), [hep-lat/0408004](#).
- [75] Ernst-Michael Ilgenfritz, M. Müller-Preussker, B. V. Martemyanov, and Pierre van Baal. *On the stability of Dirac sheet configurations*. Phys. Rev. D69, 097901 (2004), [hep-lat/0402020](#).
- [76] Pierre van Baal. *$SU(N)$ Yang-Mills solutions with constant field strength on T^4* . Commun. Math. Phys. 94, 397 (1984).
- [77] F. Bruckmann, E. M. Ilgenfritz, B. V. Martemyanov, M. Müller-Preussker, D. Nógrádi, D. Peschka, and P. van Baal. *Calorons with non-trivial holonomy on and off the lattice*. to appear in Nucl. Phys. Proc. Suppl. , [hep-lat/0408036](#).
- [78] W. Kamleh, D. B. Leinweber, and A. G. Williams. *Dynamical FLIC fermions*. Nucl. Phys. Proc. Suppl. 129, 826–828 (2004), [hep-lat/0309154](#).